Sergey Yurevich Luchkin

Local de sondagem de Li $^+$ difusão e concentração em materiais de baterias de ions de litio via Microscopia de Varredura por Sonda

Local probing of Li$^+$ diffusion and concentration in Li-ion battery materials by Scanning Probe Microscopy

Sergey Yurevich Luchkin

Local de sondagem de Li $^+$ difusão e concentração em materiais de baterias de ions de litio via Microscopia de Varredura por Sonda

Local probing of Li$^+$ diffusion and concentration in Li-ion battery materials by Scanning Probe Microscopy

o júri

presidente

Prof. Artur Manuel Soares da Silva
Professor Catedrático do Departamento de Química da Universidade de Aveiro

Prof. Senentxu Lanceros-Mendez
Professor Associado do Departamento de Física da Universidade do Minho

Prof. Verónica Cortes de Zea Bermudez
Professor Catedrático do Departamento de Química da Universidade de Trás-os-Montes e Alto Douro

Prof. José Antonio Paixão
Professor Catedrático do Departamento de Física da Universidade de Coimbra

Prof. Jorge Ribeiro Frade
Professor Catedrático do Departamento de Engenharia de Materiais e Cerâmica da Universidade de Aveiro

Dr. Andrei Leonidovitch Kholkine
Investigador Coordenador do Departamento de Engenharia de Materiais e Cerâmica da Universidade de Aveiro

agradecimentos

palavras-chave

Li-ion baterias, Li difusao, Microscopia de Tensão Eletroquímica, Microscopia de Força de Sonda Kelvin, cátodos de $LiMn_2O_4$, ânodos de grafite.

resumo

Esta tese apresenta os resultados do estudo de Scanning Probe Microscopia (SPM) de materiais de baterias de ions de litio. As medidas foram executadas na cátodos de $LiMn_2O_4$ e ânodos de grafite extraidos de bateriais de litio comerciais em diferentes estados de carga e fadiga. O estudo concentrou-se na medição da distribuição de Li e propriedades de transporte dos materiais de eletrodo ativo. Especial atencao tem sido dada a influencia do ciclo de fadiga da elevada taxa C na distribuicao especial dos ions de Li e coeficiente de difusao. Microscopia de tensão eletroquímica (ESM) tem sido usada para acessar Li transporte propriedades em nanoescala em cátodos de $LiMn_2O_4$. Microscopia de força de sonda Kelvin (KPFM) tem sido usada para acessar a distribuição espacial de Li em anodos de grafite.

ESM foi implementada e usada em um modo de única freqüência de ressonância o contato pela primeira vez. Análise de relação sinal-ruído foi feito para um número de monomodo e multimodo usados no ESM. A análise permite estabelecer critérios para um cantilever e uma instalação experimental para a detecção mais sensível de deslocamentos superficiais.

Propriedades da mobilidade dos ions de lition em catodos de bateria $LiMn_2O_4$ frescos e fatigados foram estudados em nanoescala via ESM, espectroscopia de tempo e espectroscopia de tensão de transporte. Contribuições como sinal Vegard e non-Vegard ESM foram identificadas em ciclos de histerese eletroquímica obtidos em amostras frescas e fatigadas. Em cátodos frescos o sinal Vegard dominante, enquanto em amostras envelhecidas, a diferente ciclo de histerese indica contribuições adicionais. Distribuição espacial não-uniforme do ciclo aberto eletroquímico em partículas de $LiMn_2O_4$ foram estudadas nas amostras fatigadas indicando mais forte variação do coeficiente de difusão de Li das amostras fatigadas em microescala em comparação com a outra amostra. Medições de espectroscopia de tempo revelaram a ausencia de difusidade local em amostras fatigadas por mais de duas ordens de magnitude em comparação com a outra. Atribui-se tal redução do coeficiente de difusão o acúmulo de defeitos de ponto induzida pelo Ciclo de elevada taxa C e acompanhadas de instabilidade estrutural. Este mecanismo pode ser especialmente importante para ciclo de elevada taxa C.

 Distribuição espacial de Li em cátodos amostras fresca e fatigada grafite foi analisaa via KPFM no modo de modulação de amplitude 2-pass. Estruturas de superfícies potenciais core-shell e mosaico têm sido observadas em ânodos fatigados e frescos, respectivamente. As distribuições de superfícies potenciais observadas foram atribuídas para os perfis de concentração Li aparentes em grafite. Distribuição potencial core-shell tem sido atribuída para o ions remanescentes de Li empilhados em partículas de grafite, causando perda irreversível de capacidade. A distribuição de potencial de mosaico tem sido atribuída a Li inativo dentro do grafite na fase inicial do ciclo. Os resultados corroboram o modelo "radial" usado para explicar o mecanismo de desvanecimento de capacidade específica a alta taxa de C em baterias de íon-lítio.

keywords

Li-ion battery, Li diffusion, Electrochemical Strain Microscopy, Kellvin Probe Force Microscopy,$LiMn_2O_4$ cathode, graphitic anode.

abstract

This thesis presents the results of Scanning Probe Microscopy (SPM) study of Li-ion battery active materials. The measurements have been performed on $LiMn_2O_4$ cathodes and graphite anodes extracted from commercial Li batteries at different states of charge and health. The study has been focused on measurements of Li spatial distribution and transport properties in the active electrode materials. Special attention has been paid to influence of fatigue caused by high C rate cycling on Li spatial distribution and local diffusion coefficient. Electrochemical Strain Microscopy (ESM) has been used to access Li transport properties at the nanoscale in $LiMn_2O_4$ cathodes. Kelvin Probe Force Microscopy (KPFM) has been used to examine Li spatial distribution in graphite anodes.

ESM has been implemented and used in a single frequency mode out of the contact resonance for the first time. Signal-to-noise ratio analysis has been performed for a number of single- and multi-frequency modes used in ESM. The analysis allowed to establish criteria for a proper cantilever choice and an experimental setup for the optimized detection of surface displacements via lock-in amplifier.

Transport properties of Li+ mobile ions in fresh and fatigued $LiMn_2O_4$ battery cathodes have been studied at the nanoscale via ESM using time- and voltage spectroscopies. Both Vegard and non-Vegard contributions to ESM signal have been identified in electrochemical hysteresis loops obtained on the fresh and fatigued samples. In fresh cathodes the Vegard contribution dominates the signal, while in fatigued samples different shape of hysteresis loops indicates additional contributions. Non-uniform spatial distribution of the electrochemical loop opening in $LiMn_2O_4$ particles studied in the fatigued samples indicates stronger variation of Li diffusion coefficients in fatigued samples' as compared to the fresh one. Time spectroscopy measurements have revealed suppressed local Li diffusivity in fatigued samples by more than two orders of magnitude as compared to the fresh one. We attributed such reduction of the diffusion coefficient to the accumulation of point defects induced by high C-rate cycling and accompanied structural instability. This mechanism can be specifically important for high C-rate cycling.

Li spatial distribution in fresh and fatigued graphite cathodes has been accessed via KPFM using a 2-pass amplitude modulation mode. Core-shell and mosaic surface potential structures have been observed on the fatigued and fresh anodes, respectively. The observed surface potential distributions have been attributed to the apparent Li concentration profiles in graphite. The core-shell potential distribution has been attributed to the remnant Li ions stacked in graphite particles causing irreversible capacity loss. The mosaic potential distribution has been attributed to inactive Li inside graphite at the starting stage of cycling. The results corroborate the "radial" model used to explain the specific capacity fading mechanism at high C rate cycling in Li-ion batteries.

Contents

List of figures

List of tables

Nomenclature

List of abbreviations

AFM	Atomic Force Microscopy
AM-KPFM	Amplitude Modulated Kelvin Probe Force Microscopy
BE	Band Excitation
C-rate	Cycling rate
CC/CV	Constant Current/Constant Voltage
CPD	Contact Potential Difference
DART	Dual AC Resonance Tracking
EBSD	Electron Backscatter Diffraction
EDS	Energy Dispersive X-ray Spectroscopy
ESM	Electrochemical Strain Microscopy
FM-KPFM	Frequency Modulated Kelvin Probe Force Microscopy
FWHM	Full Width at Half Maximum
HOMO	Highest Occupied Molecular Orbital
HOPG	Highly Oriented Pyrolytic Graphite
HWHM	Half Width at Half Maximum
ICP-OES	Inductively Coupled Plasma Optical Emission Spectrometry
IS	Impedance Spectroscopy
KPFM	Kelvin Prove Force Microscopy
LUMO	Lowest Unoccupied Molecular Orbital
NMR	Nuclear Magnetic Resonance
NPD	Neutron Powder Diffraction
OBD	Optical Beam Detection
OCV	Open-Circuit Voltage
PFM	Piezoresponse Force Microscopy
PVDF	Polyvinylidene Fluoride
PPLN	Periodically Poled Lithium Niobate
RH	Relative Humidity
SEI	Solid Electrolyte Interface
SEM	Scanning Electron Microscopy

SHO	Simple Harmonic Oscillator
SNR	Signal-to-Noise Ratio
SOC	State of Charge
SOH	State of Health
SP	Surface Potential
SPM	Scanning Probe Microscopy
TS	Time Spectroscopy
XRD	X-ray Diffraction
a.u.	arbitrary units

List of physical constants

F	Faraday constant, 9.6487×10^4 C·mol^{-1}
N_A	Avogadro number, 6.022141×10^{23} mol^{-1}
e	elementary charge, 1.602×10^{-19} C
k_B	Boltzmann constant, 1.38065×10^{-23} J·K^{-1}
ε_0	vacuum permittivity, 8.854×10^{-12} F·m^{-1}

List of symbols

$A_{1\omega}$	ESM response at the first harmonic of the driving signal, m
C	capacitance, F
C_i	ionic concentration, m^{-3}
C_i^0	stoichiometric ionic concentration, m^{-3}
C_i^{max}	maximum concentration of a mobile ion in an electrode, m^{-3}
D_i	diffusion coefficient of i-ion, m^2·s^{-1}
D_{ds}^z	power spectral density of the of the microscope detection system noise, m·Hz$^{-1/2}$
D_{th}^z	power spectral density of the thermal noise, m·Hz$^{-1/2}$
D_{tot}^z	power spectral density of the total displacement signal noise, m·Hz$^{-1/2}$
E	electric field, V·m
E_0	standard cell potential, V

E_a	activation energy, J
E_{ac}	ac electric field, V·m
E_{cell}	cell potential, V
E_{dc}	dc electric field, V·m
F	force, N
I	cell operating current, A
N	number of bins in the frequency domain
$\tilde{N}$	number of types of mobile ions
Q	quality factor
$\tilde{Q}_{33}$	electrostriction coefficient
Q_{ijmn}	elements of the electrostriction tensor
P	average power, W
$\mathbf{P}$	polarization vector
P_i	induced polarization
P_{ip}	induced polaron polarization
P_m, P_n	elements of the polarization vector $\mathbf{P}$
P_{noise}	power of noise, W
P_s	power of the measured response, W
P_{signal}	power of signal, W
P_{sp}	spontaneous polarization
P_{ds}^{z}	power of the detection system noise in the system bandwidth, W
R_0	tip-surface contact area, m^2
R_i	internal cell resistance, Ohm
R_S	point contact resistance, Ohm
S	area of the active electrode material, m^2
T	temperature, K
$\tilde{T}$	time period, s
$\tilde{T}_{BE}$	time duration of the BE signal $x(t)$, s

U	capacitor energy, J
V	voltage, V
$\tilde{V}$	particle volume, m^3
V_{CPD}	contact potential difference, V
W	work function, eV
Y	Young modulus, Pa
ΔG	nucleation barrier, eV
δC_i	ionic concentration change, m^{-3}
δU_{elast}	elastic energy density, J·m^{-3}
c_{klij}	elastic modulus tensor
d_{33}^{eff}	piezoelectric tensor component
f	frequency, s^{-1}
f_0	resonance frequency, s^{-1}
f_{33}	flexoelectric strain tensor component
f_{cut}	cutoff frequency, s^{-1}
$g(\omega)$	frequency response function of SHO
h	sample thickness, m
j	current density, A·m^{-2}
k	stiffness (or spring constant), N·m^{-1}
$\tilde{k}$	effective stiffness, N·m^{-1}
l_D	diffusion length, m
m	mass, g
q	ionic charge, C
q_{total}	total charge, C
$\vec{r}$	tip position
r, $\tilde{r}$	ratio of spectral densities of the thermal excitation noise to the detection system white noise
$s(t)$, $s(\omega)$	arbitrary excitation signal
t	time, s

t_D	diffusion time, s
u_{ij}	deformation (strain) response, m
x_i	coordinate
$x(t)$	periodic BE excitation signal, m
z	z-coordinate
z_i	valence of i-ions
$z_{th}^2(\omega)$	cantilever thermal noise, m·Hz$^{-1/2}$
Δf_B	system bandwidth, s^{-1}
Ξ_{33}^C	deformation potential tensor for electron contribution
Ξ_{33}^V	deformation potential tensor for hole contribution
$\Im_{ac}$	concentration dependent force
Ω	volume of an active electrode material, m^3
β	Vegard coefficient
β_{ij}	Vegard tensor
ε	Dielectric permittivity, F·m^{-1}
η_{ct}^a	activation polarizations at the anode, V
η_{ct}^c	activation polarizations at the cathode, V
η_c^a	concentration polarizations at the anode, V
η_c^a	concentration polarizations at the cathode, V
$\tilde{\eta}$	$\Delta\omega_{BE}$ width coefficient
$\theta(x)$	Heaviside step function
λ, η	phenomenological exchange coefficients
μ_{elast}	chemical potential induced by elastic energy, J·mol^{-1}
μ_i	chemical potential of i ion, J·mol^{-1}
ν	Poisson's ratio
ξ_i	coordinate
ρ	resistivity, Ohm·m

ρ_{xy}	coordinate
σ	conductivity, S·m^{-1}
σ_{ij}	mechanical stress tensor
σ_{kl}	stress tensor
τ	characteristic relaxation time, s
τ_{SHO}	time delay at the resonance of SHO, s
$\tau_{low-pass}$	time of signal averaging of the lock-in amplifier, s
υ_i	i-ion drift velocity, m·s^{-1}
φ	electrical potential, V
$\varphi(\omega)$	phase, rad
$\vartheta(\omega)$	phase of $s(\omega)$, rad
ψ	thermal excitation spectral density, m·Hz$^{-1/2}$
ω	angular frequency, rad·s^{-1}
ω_0	angular resonance frequency, rad·s^{-1}
ω_L	angular lower frequency of the frequency range, rad·s^{-1}
ω_U	angular upper frequency of the frequency range, rad·s^{-1}
ω_{cut}	angular cutoff frequency, rad·s^{-1}
ω_s	driving frequency, rad·s^{-1}
$\Delta\omega_B$	bandwidth of the system, rad·s^{-1}
$\Delta\omega_{BE}$	bandwidth of the BE signal, rad·s^{-1}
$\langle \delta n(t) \rangle$	concentration variations of electrons, m^{-3}
$\langle \delta p(t) \rangle$	concentration variations of holes, m^{-3}

Chapter 1

Introduction

Over the last decades Li-ion batteries have become an integral part of portable devices on account of their light weight and compact size. Growth in usability of electric vehicles as well as green and wireless technologies has driven continuous development of Li-ion cells. Conventional Li-ion batteries are only efficient for low-current applications such as mobile devices, but do not satisfy needs of emerging high-power automotive and renewable energy applications. Relatively high cycling rates in these applications cause faster degradation and lower specific capacity after prolonged use as compared with the conventional (low current) applications. [1]

Micromechanical effects associated with cycling significantly contribute to fatigue. Lithium intercalation and de-intercalation results in volume expansion and contraction as well as phase changes in active electrode materials. Resulting mechanical stress can cause microcracks, particle fracture, loss of contact among particles, thus leading to a reduction of the electrochemically active mass and the consequent capacity decrease. Therefore, a thorough understanding of functional properties and degradation mechanisms of electrode materials is essential for further development of energy storage technologies.

Conventional electrochemical methods can hardly be used to study functional properties at the scale less than several μm. Existing and emerging Scanning Probe Microscopy (SPM) based techniques such as Kelvin Probe Force Microscopy (KPFM) [2] and recently implemented Electrochemical Strain Microscopy (ESM) [3] are able to probe electric and transport properties of ionically conducting materials down to the nanoscale. Wider application and development of these techniques are especially important in view of the present trends in reduction of the active particles' size, often to the nm scale.

The main goals of this study are to apply these SPM based methods to commercial Li-ion battery materials in order to deeper understand microscopic origins of degradation, and to further develop the recent ESM method. Electrochemical Strain Microscopy has been used to investigate battery degradation mechanisms by measuring mobility of Li in active particles at different states of charge and health. Mainly $LiMn_2O_4$ cathodes have

been studied due to their stability under ambient conditions. The ESM method has been implemented in the single frequency out-of-resonance mode for the first time. Question about the true origin of the ESM response has been stated. Kelvin Probe Force Microscopy has been used to study degradation mechanisms of electrode materials by measuring spatial surface potential distribution associated with local Li concentration mainly in the graphitic anodes of the same batteries.

This work has been done within the FP7 Marie Curie Initial Training Network "Nanomotion" (grant agreement № 290158, www.nanomotion.eu).

This thesis is organized as follows:

Chapter 2 briefly overviews basics of the Li-ion battery functionality and properties of used active electrode materials. Special attention is paid to physical and chemical properties and problems related to degradation of $LiMn_2O_4$ cathodes and graphitic anodes.

Chapter 3 introduces principles of Kelvin Probe Force Microscopy and Electrochemical Strain Microscopy. Kelvin Probe Force Microscopy is widely used to measure local surface potential of various materials down to the nanoscale. Electrochemical Strain Microscopy is a novel method developed to measure local surface vibrations caused by influence of the external ac electric field to mobile ions below a tip.

Chapter 4 describes the samples preparation. Samples were extracted from commercial Li-ion batteries at different states of charge and health and carefully polished. Sample's phase and lithiation states were identified and presented. Implemented experimental techniques are also listed in this chapter.

Chapter 5 presents a comparative analysis of the signal-to-noise ratio of multi-frequency vs. single-frequency ESM modes. The analysis provided criteria for selection of a working mode based on the cantilever's properties and the microscope detection system sensitivity and noise level. It is shown that for certain parameters the signal-to-noise ratio for the single frequency detection can be higher than that for the multi-frequency resonance detection.

Chapter 6 summarizes ESM results obtained for $LiMn_2O_4$ cathodes of the commercial Li batteries at different stages of charge and health. The results revealed that at high C-rate cycling accumulation of structural defects makes the electrochemical system less structurally stable as compared to the fresh one. Local diffusion coefficients of Li were quantitatively estimated. The strain-diffusion coupling effect was calculated. The results were discussed within the framework of reported degradation mechanisms. Finally, alternative explanation of the ESM response origin was suggested and simulated.

Chapter 7 summarizes KPFM results obtained on graphitic anodes of the commercial Li batteries at different stages of charge and health. The results demonstrated that at high C-rate cycling relatively big structurally integral particles possess a core-shall distribution of the surface potential. By contrast, similar particles without cycling showed a mosaic distribution of the surface potential, which was attributed to inactivated regions of graphite at the early stage of cycling. Additional results obtained on the $LiMn_2O_4$ cathodes

showed that the pitting corrosion of the Al current collector could be another source of the internal resistance increase and associated capacity fading.

Chapter 8 summarizes the presented results and formulates the conclusions.

Chapter 2

Li-ion batteries: overview

The first commercially available rechargeable Li-ion battery was developed by SONY Corporation in 1991. Nowadays, the vast majority of personal mobile devises is powered by Li-ion batteries because of their light weight and compact design. They are sufficient enough to survive the short active lifetime of cellphones, laptops, and other portable electronic devices. However, they are not yet sufficient for emerging and growing automotive and green energy applications, where high power density and long lasting lifetime are urgently required. Conventional Li-ion batteries suffer from fast irreversible capacity loss due to fatigue and ageing[*]. Researchers are intensively developing new battery materials and studying degradation mechanisms in order to overcome the limitations. One of the current trends in the battery research and development is reduction of size of active particles, often to the nm scale. [4] Nanotechnology approach promises the next generation of Li-ion batteries with longer life cycle, higher power and energy density. However, it raises a number of issues such as thermodynamic instability of electrode/electrolyte interfaces or electrical connectivity of nanoparticles. One of the main issues it to understand the origin of degradation and peculiarities of the ionic transport at the nanoscale.

The purpose of this Chapter is to briefly overview the state of the art of Li-ion batteries, principles of the battery functionality, and common problems arising during their use. Special attention will be paid to widely used graphitic anode and $LiMn_2O_4$ spinel cathode materials.

---

[*] There are three terms in literature describing battery degradation: fatigue, ageing, and calendar ageing. Initially, the calendar ageing was used to describe degradation of a battery maintained at specific stable conditions, while the ageing was used to describe degradation due to cycling. Then the fatigue was used to describe degradation caused by cycling as well. Now the term ageing is used to describe both types of degradation depending on the author preferences.

2.1 Principles of Li-ion battery functionality

Li-ion battery is an electrochemical system capable to store and return electrical energy when required. The battery receives electrical energy from an external source, transforms it to chemical energy, and stores it. When required, it releases the stored chemical energy, converts it into the electrical one, and powers an external load. Typical Li-ion battery consists of a negative electrode (anode), a positive electrode (cathode), a separator, an electrolyte, and metallic current collectors (Figure 2.1). During the charging process electric potential is applied between the anode and the cathode, and mobile Li^+ ions de-intercalate from the cathode host lattice and are transferred by the electrolyte molecules through the separator to the anode, where they intercalate into the anode host lattice within a finite concentration range. During this process, the external energy is stored inside the battery. Upon discharging the anode and the cathode are connected through an external electrical circuit and the process proceeds in the opposite direction. In order to maintain the charge neutrality, these reversible electrochemical processes are accompanied by the electron transfer from the cathode to the anode and vice versa through the external circuit, where they produce electric work. The electrolyte and the separator must allow the Li^+ ionic transport but prevent the electronic transport, otherwise the electrons will not go through the external load.

In the charged state Li^+ ions are stored in the negative electrode – the anode. Metallic Li was the obvious initial choice for the anode because it has very high theoretical capacity per unit volume (3860 mAh·g^{-1}). [5] However, the metallic lithium anode suffers from critical safety issues due to formation and uncontrollable growth of Li dendrites [6] and the consequent short circuits, which damage the battery. A number of other high capacity
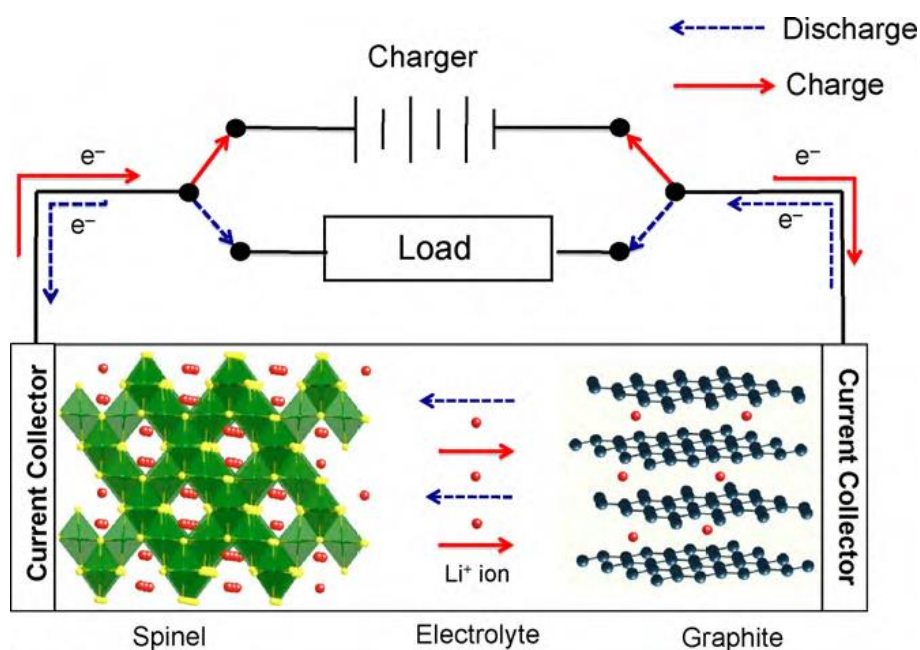
Figure 2.1. Schematic illustration of a Li-ion battery (Reproduced from Ref. [7])

alloy anodes also have critical problems with the major disadvantage coming from the high volume change upon intercalation/de-intercalation and the consequent fast degradation. Silicon [8] and other nanostructured anode materials are promising, but have not been commercialized yet. Nowadays, the most used commercial anode material is graphite because of its low and stable potential vs. Li/Li$^+$, low cost, and long life, even though its theoretical capacity more than 10 times lower than one of the metallic lithium. [9,10]

In the discharged state Li$^+$ ions are stored in the positive electrode – the cathode. The most commercially used cathode materials are layered transition metal oxides such as $LiCoO_2$ and the spinel $LiMn_2O_4$. They possess high operating voltage, but low capacity and short cycling lifetime. Additional drawbacks of $LiCoO_2$ are the high cost of Co and its toxicity. New promising class of cathode materials are polyanionic compounds such as $LiFePO_4$ and $Li_3V_2(PO_4)_3$. [11,12,13] Figure 2.2 illustrates typical electrode compounds, their theoretical capacity and voltage vs. Li/Li$^+$ reference electrode.

The driving force for Li ions to flow from the anode to the cathode and vice versa is the electrochemical potential gradient

$$\nabla \eta_{Li} = \nabla \mu_{Li} + z_{Li} F \nabla \varphi, \qquad (2.1)$$

where μ_{Li} is the chemical potential of Li$^+$ ions, z_{Li} is the Li ionic charge, F is the Faraday constant, and φ is the electric potential. While the electric potential is controlled from outside the battery, the chemical potential is the intrinsic property of the battery. It originates from difference of chemical potentials of Li$^+$ ions inside host lattices of an anode
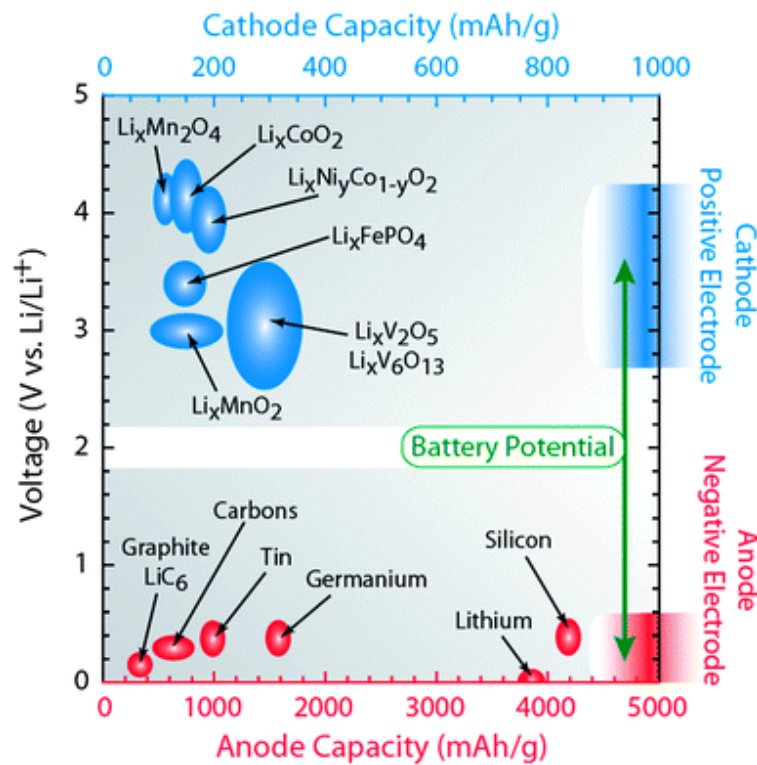
Figure 2.2. Typical anode and cathode materials, their specific capacities, and electrochemical reduction potentials with respect to metallic Li. (Reproduced from Ref. [10])

and a cathode, which is schematically illustrated in Figure 2.3.
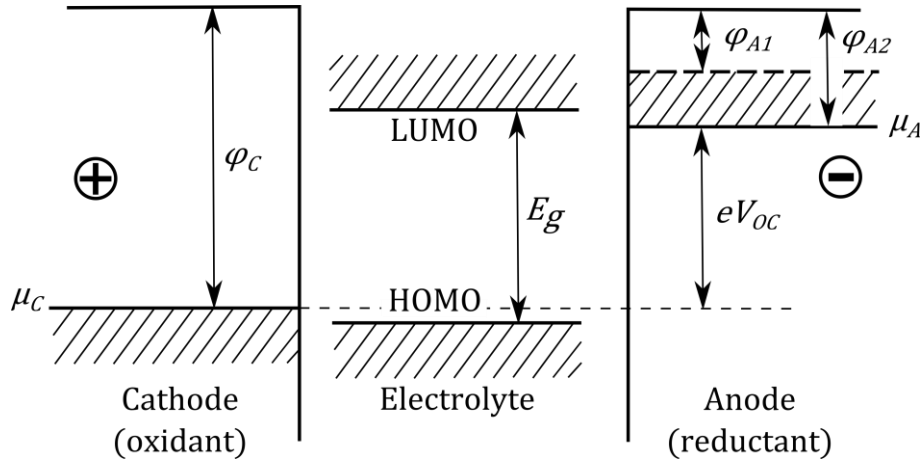
Figure 2.3. Schematic illustration of the Li-ion battery as an open circuit. Relative energies of the electrolyte window Eg and the electrode electrochemical potentials μ_A and μ_C are shown. $\varphi_{A2} - \varphi_{A1}$ is a region of the anode passivation (SEI formation) (Adopted from Ref. [12])

The chemical potential of Li^+ ions inside the anode is higher than one inside the cathode, so that the chemical potential gradient is present, driving Li^+ ions from the anode to the cathode.

The chemical potential difference must be within the electrolyte stability window between its lowest unoccupied molecular orbital (LUMO) and highest occupied molecular orbital (HOMO) energies. If μ_{Li} in the anode or in the cathode is outside the electrolyte LUMO/HOMO window, then a Li permeable passivation layer must be formed on the electrode(s) in order to make the electrochemical system thermodynamically stable. [11]

Typical reversible electrochemical reactions in the graphitic anode/$LiMn_2O_4$ cathode electrochemical system proceed as follows:

$$(-) \quad Li_xC \leftrightarrow C + xLi^+ + xe \qquad \varphi = -2.9V$$

$$(+) \quad Li_{1-x}Mn_2O_4 + xLi^+ + xe \leftrightarrow LiMn_2O_4, \quad 0 < x < 1, \quad \varphi = 0.9V$$

$$(0) \quad Li_xC + Li_{1-x}Mn_2O_4 \leftrightarrow C + LiMn_2O_4 \qquad \Delta\varphi = 3.8V$$
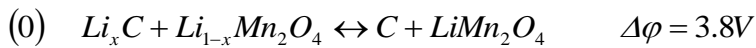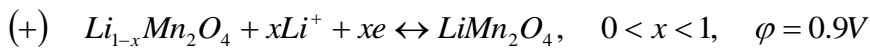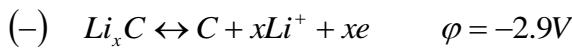
The potential difference determines the battery open-circuit voltage (OCV)

$$\Delta\varphi = \varphi^{Anode} - \varphi^{Cathode} = \frac{\left(\mu_{Li}^{Anode} - \mu_{Li}^{Cathode}\right)}{zF} \tag{2.2}$$

and gives the amount of energy per every mobile charge stored in the battery. Hence, to maximize energy stored in the battery, the amount of energy per a single charge should be maximized, i.e. the OCV should be maximized. Ideally, the operation voltage should be

stable over the whole cell discharge range. The real battery operating voltage is lower than the written above and can be schematically expressed as follows: [7]

$$E_{cell} = E_0 - \left[\eta_{ct}^a + \eta_{ct}^c\right] - \left[\eta_c^a + \eta_c^c\right] - IR_i, \tag{2.3}$$

where E_0 is the standard cell potential, η_{ct}^a and η_{ct}^c are the activation polarizations at the anode and the cathode, η_c^a and η_c^a are the concentration polarizations at the anode and the cathode respectively, I is the cell operating current, and R_i is the internal cell resistance. These parameters depend on both charge and mass transfer kinetics and, hence, the cycling rate (C-rate) and the cell degradation state (or State of Health - SOH).

Figure 2.4 illustrates typical OCV profiles and their dependence on thermodynamic properties of an electrochemical system. Solid solution without phase transitions possesses a gradual OCV slope (Figure 2.4 (a, b)). First order phase transition possesses a stable constant OCV profile (Figure 2.4 (c, d)). First order phase transition with an intermediate metastable phase (e.g. ordering) possesses a step-like OCV profile (Figure 2.4 (e, f)).

By definition, the battery capacity is an amount of charges that can be reversibly transferred between the electrodes. The total battery charge can be expressed as follows:

$$q_{total} = z \times C_i^{max} \times V \times eN_A \equiv z \times C_i^{max} \times \Omega \times F \tag{2.4}$$

where z is the valence of a mobile ion, C_i^{max} is the maximum concentration of mobile ions in an electrode, Ω is the volume of an active electrode material, e is the elementary charge, N_A is the Avogadro number, and F is the Faraday constant. Alternatively, for very small current density the total charge is

$$q_{total} \cong S \int_\tau j dt,$$

where S is the area of an active electrode material, j is the current density, and τ is the discharge time. The stored energy is proportional to the amount of energy per mobile charge ($\Delta\varphi$) multiplied by the total charge (q_{total}).
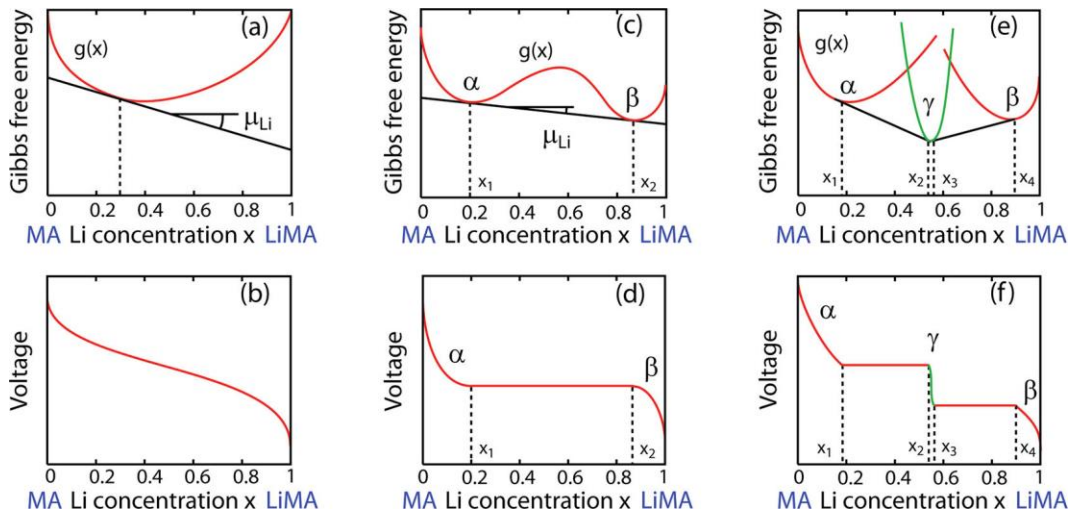
Figure 2.4. OCV profiles (b), (d), (f) are directly related to the slopes of the free energy of the electrode material (a), (c), (e). (Reproduced from Ref. [14])

In this work, commercial batteries with graphitic anodes and $LiMn_2O_4$ cathodes have been investigated. Therefore, we will further focus on properties and common degradation problems of these electrode materials.

2.2 Graphitic anode

Graphite has been widely used in many engineering, technological, and scientific applications for a long time and its properties are widely and thoroughly studied.

Crystal structure

Graphite is a polymorphic structure of carbon with the trigonal sp^2 hybridization of carbon atoms. It possesses a layered hexagonal structure with the $P6_3/mmc$ space group. Carbon atoms are strongly bonded by the covalent σ-bands within layers. The layers are joined together by the weak Van der Walls interaction (delocalized π-bands – electrons with high mobility) and stacked in the A-B consequence. The unit cell parameters are a=2.46 Å and c=6.71 Å. There are 4 atoms per unit cell. Figure 2.5 illustrates the crystal structure of graphite. [15]
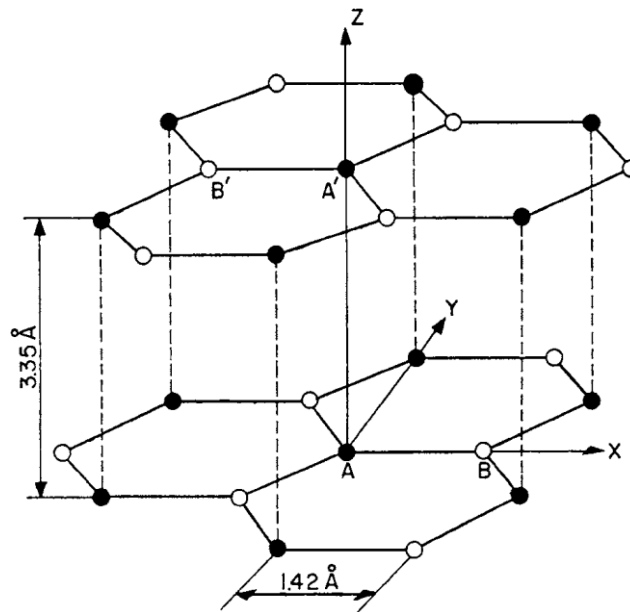
Figure 2.5. Crystal structure of graphite (Reproduced from Ref. [15]).

Electronic structure

There are 4 valent electrons per atom. Among 16 bands 12 are σ-bands (6 bonding and 6 anti-bonding) and 4 are π-bands (2 bonding and 2 anti-bonding). 16 electrons per unit cell fill 8 energy levels, therefore the Fermi level lies in the middle of π-bands. The upper π-bands overlap with the Brillouin zone edges and make graphite semimetal. At

room temperature electrical conductivity along the *a* axis is $\sigma_a = 2.26*10^4$ S·cm^{-1} and along the *c* axis is $\sigma_c = 5.9$ S·cm^{-1}. [15]

Intercalation compounds

The layered anisotropic structure with the weak bounds between the layers results in good intercalation properties – it allows intercalation of reactant between the layers. The intercalation process can be chemical or physical in nature, depending on type of intercalate. If the bonds between carbon and foreign atoms are covalent, then the intercalation is chemical. Such bonds are usually connected with 2 carbon planes, distort them in a wavy form and change the carbon bonding from the trigonal sp^2 to the tetrahedral sp^3, making it nonconductive. An example of such compound is the graphite oxide. Such intercalation materials cannot be used as the anode. [15]

If the bonds are partly ionic, such as in graphite-alkali metal compounds, then the resulting compound is lamellar with intercalates well ordered between the graphite layers. Such compounds tend to de-intercalate the foreign atoms when an external excess of such atoms is removed. Doping or accepting electrons from the foreign atoms change electronic properties of such compounds in a different manner. Li intercalation compounds (as well as other alkali intercalation compounds of graphite) are n-type, i.e. Li$^+$ ion donate electron to graphite, thus increasing its electrical conductivity. [15] The Li positive ionic charge in graphite is ≈0.8 and, in general, depends on Li concentration. [16]

The intercalation compounds pass through a number of stages depending on concentration of foreign atoms. Stage is defined by the number of carbon layers between two intercalated layers (stage 1 is 1 layer, stage 2 is two layers, stage 4 is 4 layers and so on). Hence, the higher stage corresponds to the lower concentration of intercalates.

This thesis deals with the graphitic Li-ion battery anode, therefore we will further consider only Li intercalation compounds.

Figure 2.6 illustrates the graphite-lithium phase diagram and stages.

Within the practical lithiation range the C-Li system passes through a number of stable stages which can coexist within a single grain in a form of domains: [17,18] Li$_{0.05}$C (0.2 V vs. Li/Li$^+$) – dilute stage 4, LiC$_{18}$ – stage 3, LiC$_{12}$ – stage 2, LiC$_6$ (0.05 V vs. Li/Li$^+$) – stage 1. [19–21] The average spacing between graphite layers: 3.359 Å for the pristine graphite, 3.440 Å for the stage 4, 3.513 Å for the stage 2, and 3.712 Å for the stage 1. [15,22,23]

In order to accommodate Li$^+$ ions upon intercalation, single layers of graphite translate with respect to each other into different stacking sequences depending on a stage, finally to the A-A sequence for the stage 1. [16,24,25]

Typical diffusion coefficient of Li in graphite is in the range 10^{-9}-10^{-10} cm^{2}s^{-1} and depends on the lithiation stage. [26] The diffusion coefficient becomes smaller with increasing Li concentration and changes in discontinuous manner. [7,27] The diffusion is highly anisotropic: Li$^+$ ions move along the layers and can hardly jump from one layer to
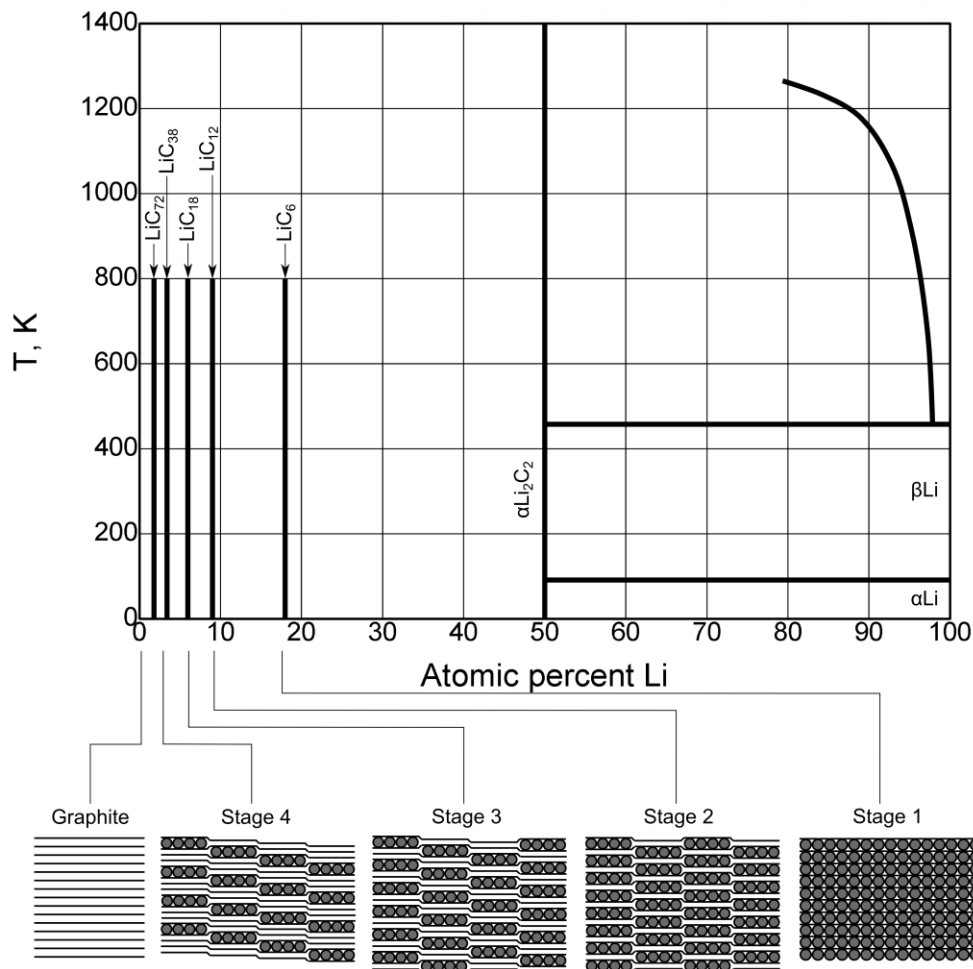
Figure 2.6. C-Li phase diagram and the stages of Li intercalation into graphite (Adopted from Refs. [28],[19])

another.

Fully intercalated graphite with 1 Li per 6 C atoms has theoretical capacity 372 mAh·g^{-1}.

Anode major degradation mechanisms

Practically, Li intercalates into graphite from an organic solvent – electrolyte. When a lithiated graphite is immersed in an electrolyte solution, a Li$^+$ permeable polycrystalline solid-electrolyte interface (SEI) is formed. [29] It happens because the chemical potential of Li in graphite $\mu_{Li}^{Graphite}$ is above the electrolyte lower unoccupied molecular orbitals (LUMO) and the lithiated graphite/electrolyte electrochemical system is thermodynamically unstable (see Figure 2.3). Reduction of the electrolyte progresses until the anode-electrolyte reaction is blocked by the passivating SEI layer, which is usually several tens of nm thick. [11] The SEI layer has sufficient Li conductivity but higher electrical resistance as compared with the pure graphite (literally speaking, it is electrically

insulating), thus increasing the overall battery resistance. Moreover, the growing SEI layer irreversibly consumes Li – the battery's essence. Finally, the SEI layer decreases both the cell OCV (Eq. 2.3) and the specific capacity (Eq. 2.4) resulting in a decrease of stored energy. It usually happens during several initial cycles.

Another degradation mechanism is a structural damage due to the volume expansion/contraction (max about 10%) and consequent stresses, especially at high C-rates and early stages of Li intercalation (x<0.1 in Li_xC_6), where it can result in local C-C bond breaking. [19]

Finally, Li progressively plates the graphite surface at high C-rates when the intercalation rate, limited by the diffusion coefficient of Li, is lower than the rate of Li delivery from the electrolyte solution to the graphite surface. [30] Li plating can lead to growth of Li dendrites, short circuits, and thermal runaway. [31]

A number of methods have been used to improve the cycle life of graphitic anodes. [32–35] These methods are mainly focused on surface modifications in order to stabilize the SEI layer.

Though graphite is one of the most studied anode materials, most of research has been done for small C-rates. Current needs for batteries for automotive applications (working at high C-rate) require studying degradation mechanisms at higher C-rates where not only the previously described degradation mechanisms can contribute to the total degradation, but new degradation mechanisms can emerge as well. In this context, various degradation effects at high C-rates can overwhelm the positive effects of surface modifications. Therefore, thorough investigation of the degradation mechanisms at high C-rate cycling is essential in order to improve the batteries' performance for current and emerging needs.

2.3 $LiMn_2O_4$ cathode

$LiMn_2O_4$ spinel has been intensively investigated over the last decades as one of the cheapest, widely available, and non-toxic material for Li-ion battery cathodes. Its functional properties and degradation mechanisms are generally well known and understood. Nevertheless, the $LiMn_2O_4$ electrical conductivity and Li diffusivity mechanisms are not completely understood.

Crystal structure

At room temperature the stoichiometric $LiMn_2O_4$ possess the cubic centrosymmetric crystal structure with the $Fd\overline{3}m$ space group and the lattice parameter a=8.24 Å. [36] There are 56 atoms per unit cell: 8 Li, 16 Mn, and 32 O. The oxygen atoms form a cubic close packed framework where the Li atoms occupy $1/8^{th}$ of the tetrahedral 8a positions and the Mn atoms occupy half of the octahedral positions designated as 16d (Figure 2.7). [37–39]
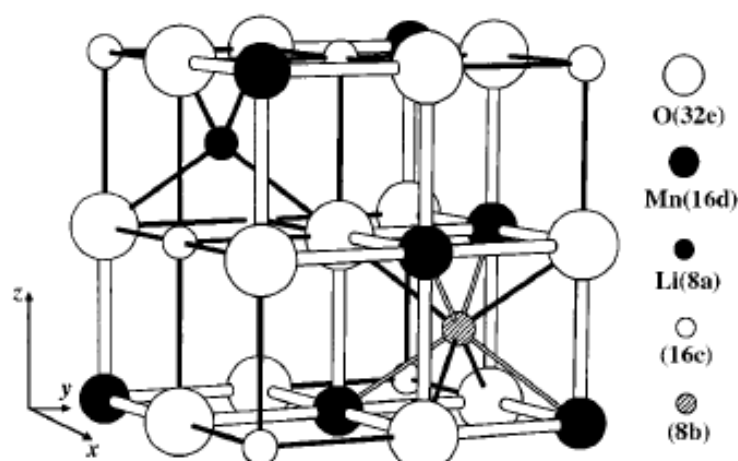
Figure 2.7. Part of the cubic $LiMn_2O_4$ spinel structure (Reproduced from Ref. [37])

Electronic properties

$LiMn_2O_4$ is a small polaron semiconductor. [12,40] Mn^{n+} ions exist in the Mn^{4+}/Mn^{3+} mixed-valence state where the high-spin $Mn^{3+}:t_2^3e^1$ and the low spin $Mn^{4+}:t_2^3e^0$ configurations coexist and the localized e electrons are trapped in local lattice relaxations. [12] The electrical conductivity is controlled by hopping of the trapped electrons between available Mn positions, i.e. it is governed by the electro-diffusion mechanism with the activation energy for the hopping process ≈ 0.16 eV. [41]

In $Li_xMn_2O_4$ ($0 \leq x \leq 1$) the electrical conductivity increases with Li concentration [42] because each Li atom donates electron to Mn^{4+} and turns it into Mn^{3+}. Reported values of the electrical conductivity at room temperature vary between 10^{-4} and 10^{-6} S cm^{-1}. [7,42,43]

$LiMn_2O_4$ as the electrode material

Figure 2.8 illustrates the Li-O-Mn phase diagram representing multiple compounds existing at room temperature around the $LiMn_2O_4$ composition. Lithiation/delithiation occurs along the λ-MnO_2 – $LiMnO_2$ stoichiometric spinel line through the $LiMn_2O_4$ cubic spinel. MnO – Li_2MnO_3 is the stoichiometric rock salt line. Practical lithiation/delithiation range in battery applications is λ-MnO_2 – $LiMn_2O_4$.

Upon lithium deintercalation from $Li_{x=1}Mn_2O_4$ the lattice parameter *a* progressively decreases (Figure 2.9). Within this process three stages can be identified. In the stage *III* where $0.6 < x < 1$ the lattice parameter linearly decreases from 8.247 to 8.194 Å according to the Vegard law; in the stage *II* where $0.4 < x < 0.55$ the lattice parameter linearly decreases from 8.17 to 8.15 Å. There is a discontinuity gap of 0.02 Å between these stages. Upon further delithiation in the stage *I* from *x*=0.4 to 0.1 the lattice structure becomes unstable and can split into two cubic phases: one with the 8.150 Å lattice parameter and another with the 8.072 Å lattice parameter. [36,44] If splitting does not occur, the fully deintercalated spinel has the lattice parameter *a*=8.029 Å and is known as λ-MnO_2. [45,46] Exact lattice
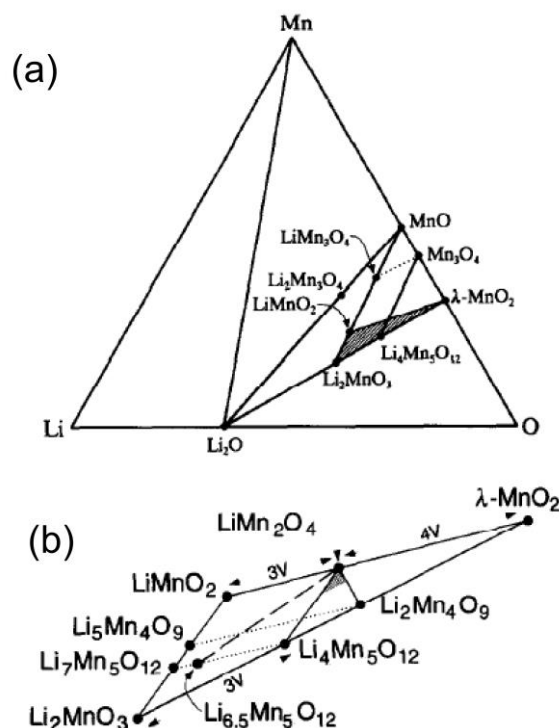
Figure 2.8. (a) An isothermal slice of the ternary Li-Mn-O phase diagram at 25°C; (b) an expanded view of the shaded region of the phase diagram in (a). (Reproduced from Ref. [47])

parameters and Li concentration of the phase transitions strongly depend on sample's defect structure, oxygen and manganese nonstoichiometries, contaminations, average Mn valence state, etc. [36]

Upon Li intercalation when x exceeds 1 in $Li_xMn_2O_4$ (stage *IV*) (average Mn^{n+} oxidation state ≤ 3.5) the phase transformation from the cubic $LiMn_2O_4$ (space group $Fd\bar{3}m$) to the tetragonal $Li_2Mn_2O_4$ (space group I41/amd) takes place. [37] This transformation is accompanied by the first order Jahn-Teller distortion and the severe lattice deformation to $c/a=1.16$ (the tetragonal lattice parameter a is smaller and c is higher than the cubic lattice parameter a). Further Li insertion into $Li_2Mn_2O_4$ results in transformation to the layered $Li_4Mn_2O_4$ structure, which is unstable upon delithiation and converts back into $LiMn_2O_4$. [46]

Figure 2.10 illustrates the electrochemical OCV profile of $Li_xMn_2O_4$ versus Li reference electrode for $0 \leq x \leq 2$. Upon intercalation from $\lambda-MnO_2$ to $LiMn_2O_4$ Li^+ ions fill the tetrahedral 8a positions in the 4V spinel region. This region is separated into two sub-regions by a ≈ 150 mV step around the composition $Li_{0.5}Mn_2O_4$, where the discontinuity gap of 0.02 Å has been detected. [48] The reason for that is believed to be ordering of Li^+ ions at one half of the tetrahedral 8a sites. Li insertion into the octahedral 16c positions of $Li_{x=1}Mn_2O_4$ is accompanied by the Jahn-Teller distortion and the voltage drop to $\approx 3V$ (Figure 2.10). Further Li insertion is followed by the transformation to the layered $Li_4Mn_2O_4$ structure and the voltage drops to ≈ 1.2 V. [46]
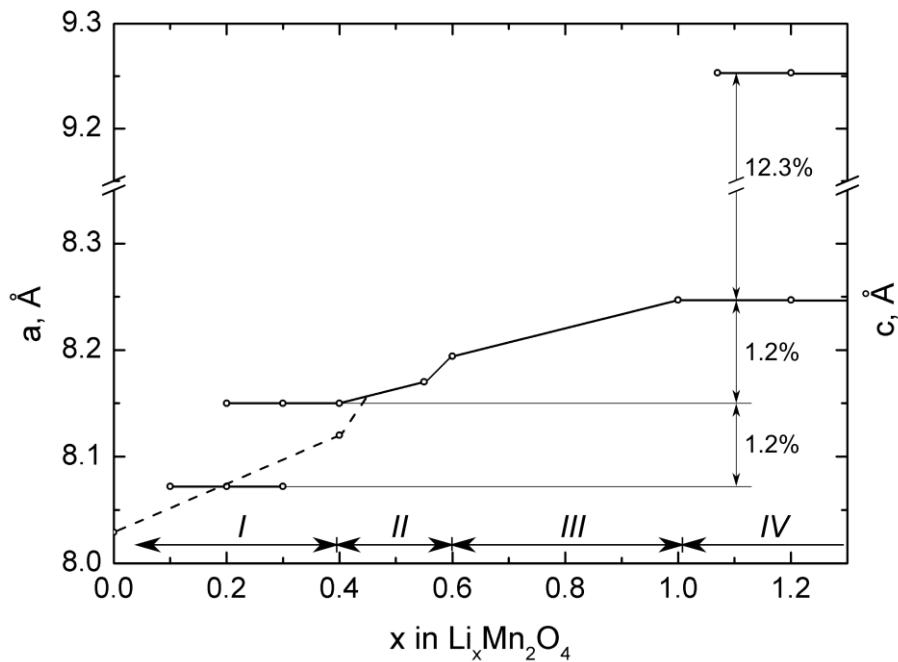
Figure 2.9. Variation of the lattice parameter as a function of Li concentration. *a* is the cubic lattice parameter, *c* is the tetragonal lattice parameter after the cubic to tetragonal phase transformation. Dash line shows variation of the cubic lattice parameter if spliting into two cubic phases does not occur. Percents show the lattice parameter expansion. (Adopted form Refs. [36], [48])
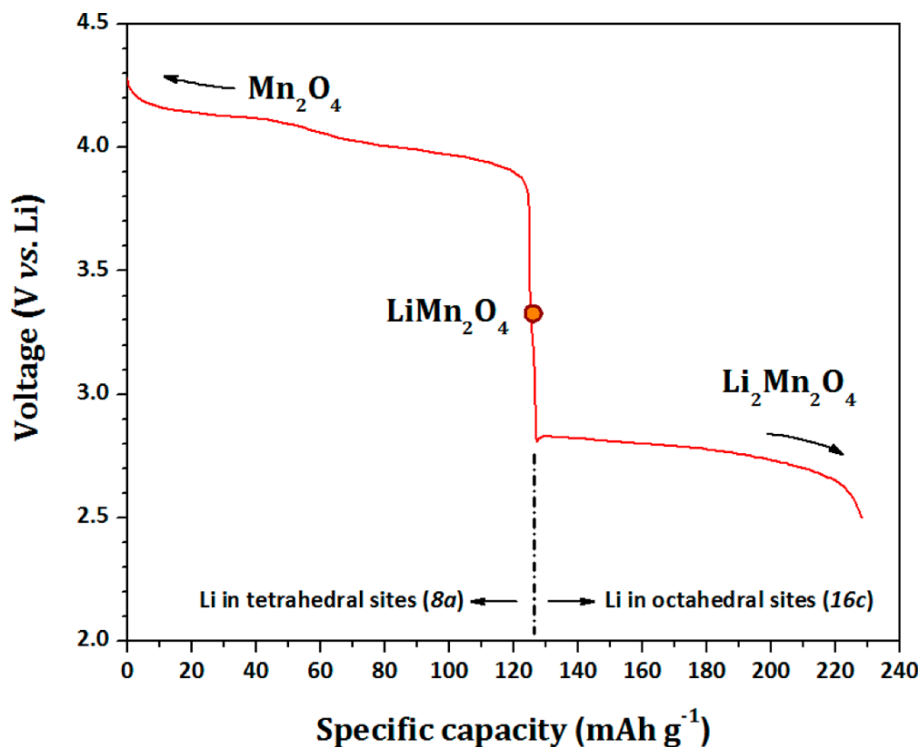
Figure 2.10. Voltage – capacity profile of the $Li_xMn_2O_4$ cathode over the $0<x<2$ lithiation range (Reproduced from Ref. [11])

Only the 4V region is practically interesting for battery applications because otherwise the Jahn-Teller distortion results in fast degradation due to the strong internal mechanical stress and particle fracture.

Resent experimental data shows that the real distribution of Li^+ ions in the lattice is more complex. Synchrotron XRD experiments allowed to determine that part of Li^+ ions is displaced from the ideal 8a positions into the octahedral 16c positions. [38] Nuclear magnetic resonance (NMR) revealed that Li^+ occupies 8a, 16c, and 16d positions. [38,49] *In-situ* neutron powder diffraction (NPD) experiments during charge-discharge cycles showed that Li insertion/extraction in the Li-reach $Li_{1+y}Mn_2O_4$ spinel proceeds in four stages: (1 – discharge) Li occupies the tetragonal 16c sites first; (2 – discharge) Li transfers from the 16c to the tetrahedral 8a sites; (3 – charge) Li removes directly from the 8a sites; (4 – charge) Li transfers to the 16c sites and removes from both 8a and 16c sites. [50] These data can be helpful for further explanation of Li diffusivity and its dependence on Li concentration.

Theoretical capacity of $Li_xMn_2O_4$ ($0 \leq x \leq 1$) is 148 mAh/g. [37] 120 mAh/g practical rechargeable capacity corresponds to insertion/extraction of 0.4 Li per 1 Mn. [46]

Li diffusion

Li diffusion in the $Li_xMn_2O_4$ spinel is not fully understood yet.

Before discussion, we want to emphasize that the concentration gradient is not the diffusion driving force as one can erroneously conclude from Fick's laws. As it was suggested by G. S. Hartley [51] and demonstrated by L. S. Darken, [52] the chemical potential gradient is the main thermodynamic factor controlling the chemical diffusion.

The conventional Li diffusion mechanism suggests that Li^+ ions simply hop over a saddle point from an initially occupied 8a position over a single vacant 16c position into the next vacant 8a position along the [111] direction, which forms the three-dimensional network (Figure 2.11). [38] Within the framework of this approximation, an increase of Li concentration should result in a decrease of available neighboring 8a vacant positions and in an increase of the potential barrier for Li to hop from the 8a to the 16c position and, consequently, should decrease the diffusion coefficient. However, real diffusion mechanisms in transition metal oxides are more complex.

Experimentally determined diffusion coefficients of Li (D_{Li}) in the spinel $Li_xMn_2O_4$ vary in a wide range from $\sim 10^{-9}$ to $\sim 10^{-12}$ cm^2s^{-1} depending on a measurement technique and a sample preparation. [7,53,54] Additionally, the Li diffusion coefficient strongly depends on the Li concentration in a complex and nonlinear manner. Chung et al [53] reported an order of magnitude variation of D_{Li} during charging/discharging with two minima (Figure 2.12). Saidi et al [39] suggested that the minima can be attributed to the Coulomb interaction between the guest-host and the guest-guest ions and Li ordering around the $Li_{0.5}Mn_2O_4$ composition. Additional deviation of the diffusion coefficient from the simplified classical interpretation can come from other sources such as presence of impurities or Mn and O nonstoichiometry (defect structure). [55]
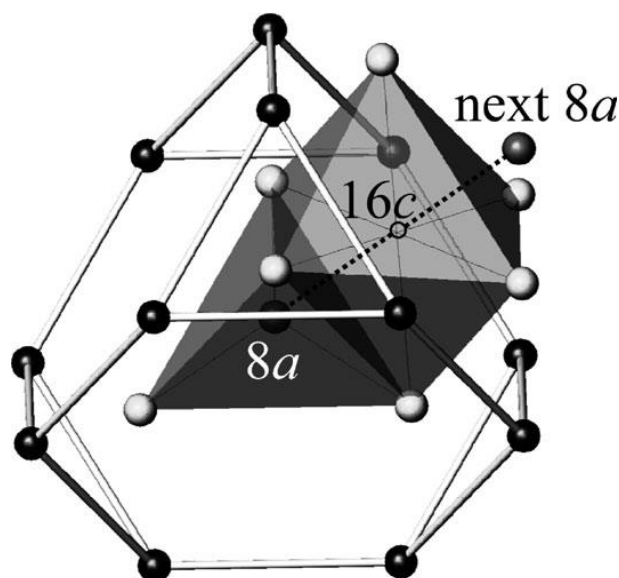
Figure 2.11. First and second nearest coordination shells around 8a and 16c positions in $LiMn_2O_4$ (Reproduced from Ref. [38])

Considering the presented above experimental evidence, the classical diffusion mechanism with the saddle point activation energy seems not to be the case. Moreover, it is not consistent with the small polaron hopping mechanism of the electrical conductivity. [38,56] During Li intercalation/deintercalation the electronic charge transfer occurs at the Fermi level of $Li_xMn_2O_4$ (large intercalation range requires high density of states near the Fermi level). Delocalized electronic states at the Fermi level do favor fast ionic kinetics while the localized electronic states do not. [56] Because the high-spin $Mn^{3+}:t_2^3e^1$ electronic states are localized, the conventional ambipolar diffusion of Li should be suppressed. Nevertheless, $LiMn_2O_4$ shows good intercalation properties that cannot be explained by the conventional diffusion mechanism. [56]

Tateishi et al [57] proposed another mechanism of Li diffusion, where hopping of the Mn^{3+} e_g electron over Mn^{n+} ions mediates displacement of an O^{2-} ion (dynamic deformation of the LiO_4 tetrahedra) and opens the bottleneck of the oxygen tetrahedral cage around the tetragonal 8a position (Figure 2.11). As a result, the potential barrier between the neighbor 8a and 16c positions drops down and allows Li^+ to hop from one position to another. According to the suggested mechanism, Li diffusion is strongly depends on the electron-lattice interaction (Li-polaron coupling), i.e. the activation energy is related to the lattice distortion energy rather than to the potential barrier energy. [58]

This supposition is in agreement with the fact that Li exchange starts when Mn^{3+}/Mn^{4+} charge ordering disappears upon the first order orthorhombic (space group Fddd) to cubic (space group $Fd\bar{3}m$) phase transformation around room temperature ($\sim$280-300 K). [49] This transition is accompanied by the rapid nonlinear change of conductivity from the low to the high temperature activation processes. [41,49,59] When the charge ordering disappears, the electrons start to hop more frequently and conductivity increases, as was experimentally verified. [56]
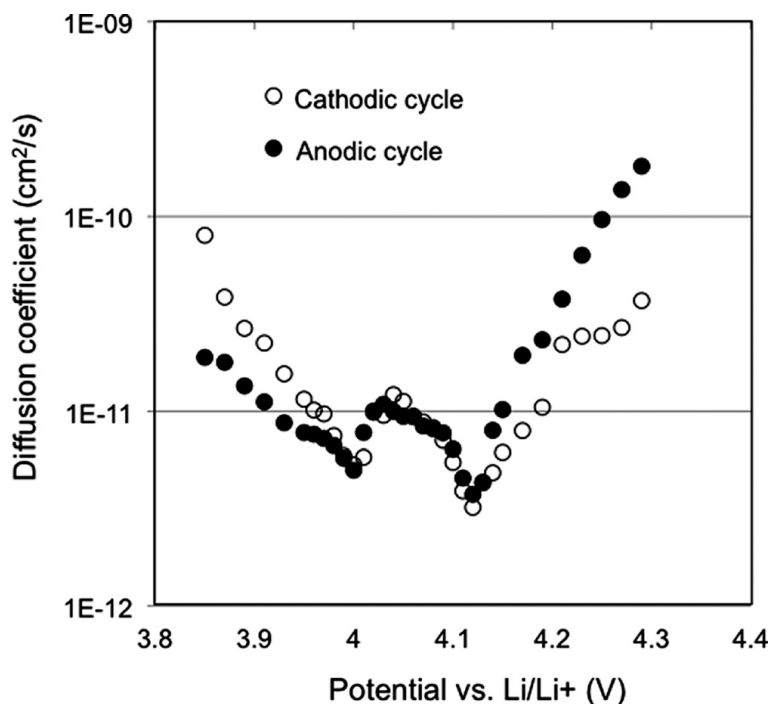
Figure 2.12. Li diffusion coefficient in $Li_xMn_2O_4$ as a function of cell potential vs. Li reference electrode. Both cathodic and anodic cycles are shown. (Reproduced from Ref. [53])

Li diffusion coefficient and electronic conductivity do not follow the same function of Li concentration though. As such, much of the physics underlying Li diffusion in $LiMn_2O_4$ and its interaction with the electronic host structure remains unknown.

It is worth mentioning that the reported Li diffusion coefficient in $Li_2Mn_2O_4$ is an order of magnitude lower than in the cubic phase. [60]

Common problems and related degradation mechanisms

Degradation of $LiMn_2O_4$ active particles occurs via three major mechanisms:

- surface degradation due to Mn dissolution caused by the disproportional reaction $2Mn_{solid}^{3+} \rightarrow Mn_{solid}^{4+} + Mn_{solution}^{2+}$; [36,61,62]

- particle cracking and consequent loss of the electrical contact with the current collector due to internal stress generated upon lithiation/delithiation; [63–65]

- structural instability and loss of crystallinity in the bulk due to Li intercalation/deintercalation and associated structural transformations. [66]

Many researchers consider Mn dissolution as the primary mechanism of capacity fading, though it was shown to be responsible for only 23% of the overall capacity decrease on cycling at room temperature. [67] It happens on the $LiMn_2O_4$/liquid electrolyte interface in the high voltage region [36] and results in a decrease of the spinel phase available for Li intercalation on the surface. Possible redeposition of nonconducting Mn-electrolyte reaction products on the surface of active $LiMn_2O_4$ particles additionally increases the internal resistivity and decreases the specific capacity. [68]

Partial substitution of Mn^{n+} cations by divalent and trivalent cations (such as Ni, Cr, Co) stabilizes the spinel structure and partly suppresses the Mn dissolution [69,70] by decreasing the Mn^{3+}/Mn^{4+} ratio (increasing the average Mn^{n+} valence state). Another method to suppress the Mn dissolution is to isolate $LiMn_2O_4$ from the electrolyte by coating particles with oxide materials such as ZnO or Mn_2O_3. [69]

Cracking of the active particles happens due to severe internal stress created mainly during the first order Jahn-Teller distortion when the average Mn^{n+} valence state falls below 3.5, accompanied by the 6% volume change. [65,71] It is then followed by loss of electrical connectivity of active particles, and parts of the cracked particles become electrochemically inactive, thus decreasing the overall battery capacity. Larger particles are more susceptible to cracking events, especially at high C-rates. [63,64]

This effect can be reduced by suppressing the Jahn-Teller distortion. It can be accomplished by partial substitution of Mn^{n+} cations to Li^+, thus increasing the average Mn^{n+} valence. [46] Mn^{n+} can also be substituted by other cations such as Cr, Ni, Co, etc. [72]

Structural instability and loss of crystallinity in the bulk due to Li intercalation/de-intercalation is also presumably caused by the Jahn-Teller distortion and instability of the cubic phase in the delithiated state. Stabilization of the cubic phase can be achieved by partial substitution of Mn^{n+} cations by other cations as described above.

All these methods could significantly improve the $LiMn_2O_4$ performance. Nevertheless, limited understanding of Li diffusion and degradation mechanisms, especially at high C rates, abridges positive effects of modifications.

Non-toxic and widely available $LiMn_2O_4$ along with its high open-circuit voltage versus Li makes it one of the promising cathode materials for Li-ion batteries. However, the possibility of its application in growing fields such as automotive is limited due to poor cycling performance, especially at high C rates. Therefore, deeper understanding of degradation of relevant functional properties (e.g. Li mobility) at meso- and nano-scales is required.

- 21 -

Chapter 3

Scanning Probe Microscopy methods

Improvement and optimization of Li-ion batteries require complex study of implemented and future electrode materials involved in Li transport. It is prerequisite to study Li transport and diffusion at the highest possible resolution for deeper understanding of degradation processes taking place in battery materials during intensive cycling.

Conventional electrochemical methods such as electrochemical impedance spectroscopy, potentiostatic and galvanostatic intermittent titration techniques [73,74] have long been used to measure kinetic and thermodynamic properties of energy storage materials. However, their lateral resolution, limited to several μm, does not allow to access electrochemical properties at the scale of single grains and grain boundaries. Rapid development of Scanning Probe Microscopy (SPM) based techniques during last decades has allowed to access structural and functional properties of materials at the nanoscale. SPM-based techniques have already been implemented to study photovoltaics and solar cells, fuel cells, and Li ion batteries. [75,76,77]

The purpose of this Chapter is to describe principles of Kelvin Probe Force Microscopy and Electrochemical Strain Microscopy, and to explain how they can be used to study functional properties of Li-ion battery materials at micro- and nanoscale.

3.1 Kelvin Probe Force Microscopy

3.1.1 Principles of KPFM

Kelvin Probe Force Microscopy (KPFM) was first introduced by M. Nonnenmacher in 1991. [2] Since then, it has been widely implemented to study electronic properties of semiconductors. [78,79] Recently, it has been used to study Li-ion battery materials. [77,80]

KPFM is a non-contact SPM method. It is based on detection of a contact potential difference (CPD) between a SPM tip and a sample's surface. Figure 3.1 schematically
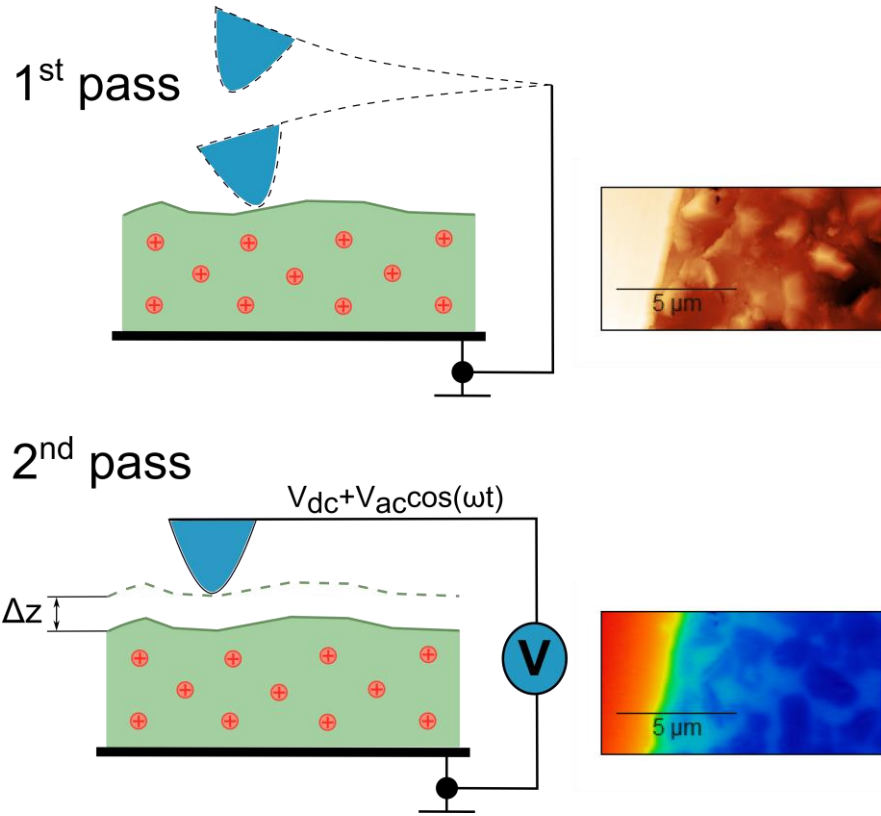
Figure 3.1. Schematic representation of the operation principle of 2-pass KPFM.

illustrates operation of the 2-pass KPFM mode. During the first pass, topography of a sample is recorded in the tapping mode. During the second pass, a tip, lifted at a certain height, passes above the surface following the recorded topography profile. Simultaneous application of ac and dc voltages between the tip and the sample allows measurement of contact potential difference as further described in details.

The tip-surface system can be considered as a capacitor with the energy $U = \dfrac{CV^2}{2}$, where C is capacity and V is voltage. Electrostatic force between the tip and the sample originates from the surface potential difference $V_{CPD} = \dfrac{W_{tip} - W_{sample}}{-e}$, where W_{tip} and W_{sample} are the work functions of the tip and the sample, and e is the electronic charge. [79] By definition, the electrostatic force $F = -\nabla U$ is always attractive. In case of KPFM, the tip displacement is only detected in the vertical z direction, hence we can write

$$F = -\frac{\partial U}{\partial z} = -\frac{\partial}{\partial z}\left(\frac{CV^2}{2}\right) = -\frac{1}{2}V^2\frac{\partial C}{\partial z}.$$

Potential applied to the tip can be written as $V_{tip} = V_{dc} + V_{ac}\sin(\omega t)$, where ω is the tip resonance frequency. $V_{ac}\sin(\omega t)$ generates oscillating electrostatic force that results in cantilever vibrations measured by the microscope detection system. The resulting force is

$$F = -\frac{1}{2}\left[V_{CPD} + V_{dc} + V_{ac}\sin(\omega t)\right]^2 \frac{\partial C}{\partial z} =$$

$$= -\frac{1}{2}\frac{\partial C}{\partial z}\left[\left(V_{CPD} + V_{dc}\right)^2 + \frac{V_{ac}^2}{2} + 2\left(V_{CPD} + V_{dc}\right)V_{ac}\sin(\omega t) - \frac{V_{ac}^2}{2}\cos(2\omega t)\right].$$

Here

$F_0 = -\frac{1}{2}\frac{\partial C}{\partial z}\left[\left(V_{CPD} + V_{dc}\right)^2 + \frac{V_{ac}^2}{2}\right]$ is the static force,

$F_{1\omega} = -\frac{\partial C}{\partial z}\left(V_{CPD} + V_{dc}\right)V_{ac}\sin(\omega t)$ is the oscillating force at a given frequency, and

$F_{2\omega} = \frac{1}{4}\frac{\partial C}{\partial z}V_{ac}^2\cos(2\omega t)$ is the oscillating force at the double frequency.

The system is tuned to nullify the first harmonic of the signal $F_{1\omega}$ by applying $V_{dc} = -V_{CPD}$. The exact sign of the V_{dc} depends on whether it is applied to the tip or to the sample. [79] Thus, the contact potential difference $V_{CPD} = \dfrac{W_{sample} - W_{tip}}{e}$ can be obtained. The tip work function is known (typically, the Pt coated cantilever is used with W_{Pt}=5.27±0.08 eV), [81] so the sample's work function can be easily extracted.

The above analysis is valid for the case of a metallic sample surface and the metal coated cantilever under vacuum conditions. In this case, the contact potential difference reflects the work function that is a difference between the Fermi energy level and the vacuum energy level. In the case of a semiconductor sample, the contact potential difference depends on both the space-charge layer and the trapped surface charge, and is more complicated for quantification. [82] In case of an insulating sample, the contact potential difference depends only on the charge trapped on the sample's surface (Figure 3.2).
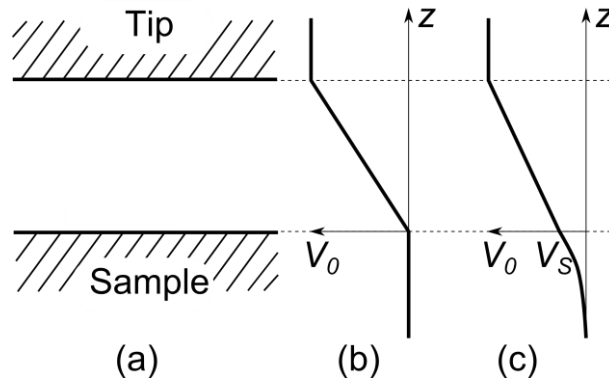
Figure 3.2. Potential distribution in the tip-sample system: (a) tip and sample positions; (b) metallic tip – metallic sample potential distribution; (c) metallic tip – semiconductor sample potential distribution. V_0 is the voltage on the metallic tip, V_S is the semiconductor surface potential. (Adopted from Ref. [82])

3.1.2 Working modes and resolution

The microscope detection system can detect the amplitude of an oscillating cantilever and its phase. It cannot detect the force directly. Depending on the measured parameter, the amplitude modulation (AM-KPFM) and the frequency modulation (FM-KPFM) modes are distinguished. As follows from their names, in the AM-KPFM mode the cantilever oscillation amplitude is tracked and nullified; in the FM-KPFM mode the cantilever oscillation frequency is tracked and nullified.

In the AM-KPFM mode topography is measured in the conventional tapping mode at the first (or fundamental) cantilever resonance frequency ω_0. During the second pass, the ac potential $V_{ac}\sin(\omega t)$ is applied at the second cantilever resonance frequency $\omega = 6.25\omega_0$ to avoid possible crosstalk with the topography and to increase the oscillation amplitude by the quality factor Q. Electrostatic interaction between the tip and the sample with the force $F_{1\omega} = -\dfrac{\partial C}{\partial z}(V_{CPD} + V_{dc})V_{ac}\sin(\omega t)$ results in cantilever oscillations, nullified by applying $V_{dc} = -V_{CPD}$. The ac modulation amplitude should be high enough to excite detectable oscillations. The resonance-enhanced detection allows using low V_{ac} and minimizing possible band bending in semiconductors with the minimum impact from topography. [75] The measured amplitude correlates with the force. [83]

In the FM-KPFM mode topography is measured in the conventional tapping mode at the first cantilever resonance frequency ω_0 exactly as in the AM-KPFM mode. During the second pass, the cantilever is mechanically excited at the first resonance ω_0 and additional ac potential $V_{ac}\sin(\omega t)$ is applied and modulates the oscillation of the electrostatic force $F_{1\omega} = -\dfrac{\partial C}{\partial z}(V_{CPD} + V_{dc})V_{ac}\sin(\omega t)$. The resulting shift of the first resonance frequency correlates with the force gradient. [83] Indeed, the resonance frequency [84] is defined as $\omega_0 = \sqrt{\dfrac{k}{m^*}}$, where k is the cantilever stiffness and m^* is the cantilever effective mass. If the external force F with the gradient $\dfrac{\partial F}{\partial z}$ is applied, the effective stiffness is changing, thus changing the resonance frequency $\omega_0' = \sqrt{\dfrac{k - \dfrac{\partial F}{\partial z}}{m^*}} \approx \omega_0\left(1 - \dfrac{1}{2k}\dfrac{\partial F}{\partial z}\right)$. It leads to appearance of additional signals shifted by $\Delta\omega = \omega_0 - \omega_0' = \dfrac{1}{2k}\dfrac{\partial F_{1\omega}}{\partial z} = -\dfrac{1}{2k}\dfrac{\partial^2 C}{\partial z^2}(V_{CPD} + V_{dc})V_{ac}\sin(\omega t)$ from the first resonance at ω_0. This signal is nullified by applying $V_{dc} = -V_{CPD}$. The modulation frequency ω should be high enough to avoid the apparent crosstalk with the topography, but to stay within bandwidth of the frequency demodulator. [83]
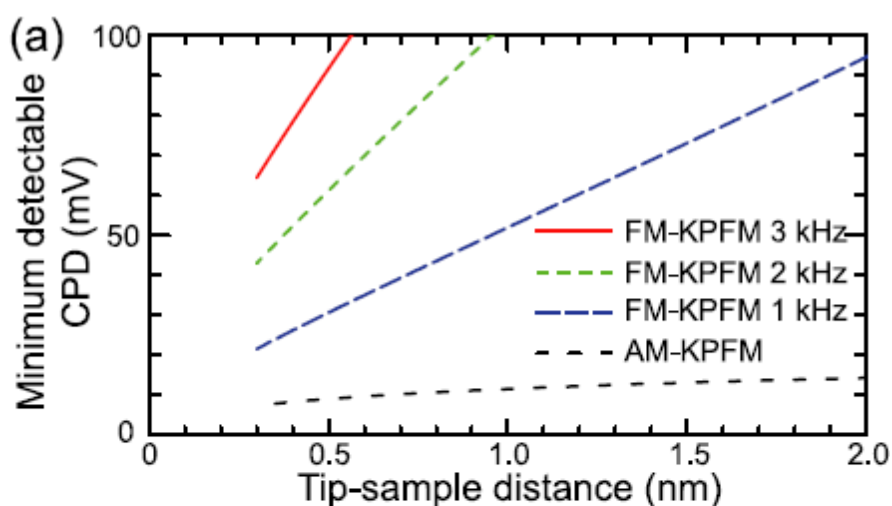
Figure 3.3. Theoretical calculation of the minimum detectable CPD for AM- and FM-KPFM as a function of the tip–sample distance (Reproduced from Ref. [85])

It was shown that FM-KPFM has higher lateral sensitivity than the AM-KPFM because it probes the force gradient (shorter range than the force) and, thus, has stronger distance dependence as compared with the AM-KPFM. [85,86] In the FM-KPFM mode mainly the tip apex contributes to the detection, while in the AM-KPFM mode the apex contribution is smaller and the lever contribution is stronger. [87] At the same time, AM-KPFM has higher energy resolution (Figure 3.3). [85]

Recently, Nagpure et al [77] implemented KPFM to measure surface potential of aged and fresh $LiFePO_4$ cathodes. They found that the surface potential of the aged samples is lower than that of the fresh ones. In another work, Jing Zhu et al [80] used KPFM to study changes of the surface potential of TiO_2 anode in an all-solid-state Li-ion battery during Li insertion and extraction. These results clearly demonstrated a great promise of KPFM for characterization of battery materials at the mesoscale.

3.2 Electrochemical Strain Microscopy

3.2.1 Principles of ESM

Electrochemical Strain Microscopy (ESM) has emerged after application of Piezoresponse Force Microscopy (PFM) to non-ferroelectric ionic conductors. The observed response was attributed to reversible modulation of the local molar volume below the tip due to intercalation and deintercalation of mobile ions under applied electric field. Similar to PFM, its lateral resolution is limited by the tip diameter and typically varies between 5 and 50 nm, and vertical resolution is of the order of several pm (because of the lock-in amplification). Thus, a tiny electrochemical response can be detected inside single grains and even at grain boundaries of polycrystalline ionic conductors. [88] ESM method

with time and voltage spectroscopies in general combines microscopy itself, spectroscopy, and electrochemical probing at the nanoscale.

Before further description, it is important to mention and keep in mind that the high-frequency ESM response mechanism is not fully understood and the theory is not complete by now. The first – diffusion-based – model was suggested in 2010. [3] Since then, a number of works on computer modeling of ESM showed that at high frequencies the diffusion-based response must be well below the microscope detection limit. [89,90] Still, the response is experimentally detectable at 200-400 kHz frequencies. Another mechanism of the high-frequency response has been recently suggested. [91] We will postpone its discussion to Chapter 6 (§ 6.5). In this Chapter we will focus on the diffusion-based description. Despite of the mentioned limitations in the high-frequency regime, it accurately describes static (0 kHz) and low-frequency (<<100 kHz) processes.

Electrochemical Strain Microscopy is based on detection of oscillating surface displacements presumably caused by ionic motion and the consequent local volume change under applied electric field. In ESM, an external ac voltage is applied between a conducting SPM tip operating in the contact mode and a sample's counter electrode. Resulting electric field alters local electrochemical potential of lithium (or other mobile ions) in a host lattice, causing them to locally intercalate or deintercalate. Consequent changes of their local concentration mediate expansion or contraction of the lattice under the tip (Figure 3.4). Corresponding oscillating surface displacements are detected by the SPM detection system via a lock-in amplifier.

The diffusion-based description of the ESM response was given by Morozovska et al. [3] It requires solution of conjoint elastic and diffusion problems. Fick's laws were used assuming absence of strain-diffusion coupling and negligible thermal expansion effect. Note, that Fick's laws are true only for small concentrations and concentration gradients in binary or pseudo binary systems. Nevertheless, they are often (but not always) applicable to describe real systems with appropriate accuracy. [92]

Equation of state for anisotropic elastic media with elastic compliance tensor s_{ijkl}, Vegard's tensor β_{ij}, concentration excess δC_i, mechanical stress tensor σ_{ij}, and elastic strain u_{ij} is following: [3,93,94]

$$u_{ij} = \beta_{ij}\delta C_i + s_{ijkl}\sigma_{kl}\,. \tag{3.1}$$

For the isotropic Vegard tensor $\beta_{11} = \beta_{22} = \beta_{33} = \beta$ and concentration excess $\delta C_i(x_1, x_2, x_3, t)$, using equilibrium $\sigma_{ij,j} = 0$ and boundary conditions on the surface $\sigma_{ij}n_j\,|_S = 0$, the solution for the displacement field is: [3,89,95]

$$u_3\left(x_1, x_2, 0, t\right) = -\frac{(1+\nu)}{\pi}\beta\iiint\limits_{\xi_3>0}\frac{\xi_3\delta C_i(\xi_1, \xi_2, \xi_3, t)d\xi_1 d\xi_2 d\xi_3}{\left((x_1-\xi_1)^2 + (x_2-\xi_2)^2 + \xi_3^2\right)^{3/2}} \tag{3.2}$$

This Equation can be simplified in case of an axially symmetric electric field $\varphi(\rho_{xy}, z, \omega)$ with axially symmetric redistribution of the ionic concentration $\delta C_i(\rho_{xy}, z, \omega)$, were
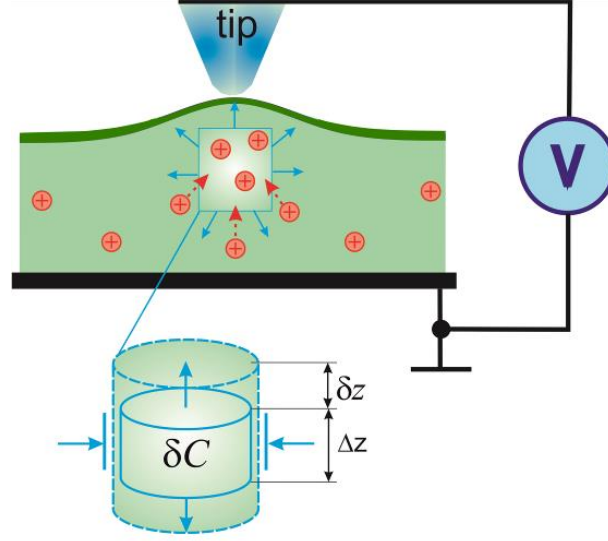
Figure 3.4. Upper image – the surface deformation δz as a result of local change of a lattice parameter due to change of ionic concentration under the tip. Lower image – deformation δz of a small cylinder with the Δz height clamped laterally.

$\delta C(\rho_{xy}, z, \omega)$ is the frequency spectrum of $\delta C_i(x_1, x_2, x_3, t)$ and $\rho_{xy} = \sqrt{x^2 + y^2}$. Then the linear surface displacement at the tip-surface junction $z = 0$ is [95]

$$u_3(0, \rho = 0, \omega) = -\frac{(1+\nu)}{\pi}\beta\int\limits_0^h dz\int\limits_0^\infty d\tilde{\rho}\tilde{\rho} \cdot \frac{z \cdot \delta C_i(\tilde{\rho}_{xy}, z, \omega)}{\left(\tilde{\rho}_{xy}^{\ 2} + z^2\right)^{3/2}} \tag{3.3}$$

$$\delta C(\rho_{xy}, z, t) \approx \delta C(z, t)\theta(R_0 - \rho_{xy}) , \tag{3.4}$$

where $\theta(x > 0) = 1$ and $\theta(x < 0) = 0$ is the Heaviside step function. Equation (3.4) is valid when the Li-diffusion length is less than the tip-surface contact area R_0, i.e. $\omega\tau >> 1$ (ω is the driving frequency, τ is the characteristic diffusion time). The concentration field (3.3) is a function of z at $\rho_{xy} \leq R_0$ and is zero outside the tip-surface contact. It vanishes when $z >> R_0$. Then

$$u_3(z = 0, \rho_{xy}, \omega) \approx -\frac{(1+\nu)}{\pi}\beta\theta(R_0 - \rho_{xy})\int\limits_0^h \delta C_i(z, \omega)dz . \tag{3.5}$$

It can be expressed via the average concentration variation $\langle\delta C_i\rangle = \frac{1}{h}\int\limits_0^h \delta C_i(\rho_{xy}, z, \omega)dz$

and the total charge $Q = q\int\limits_0^h \delta C_i(\rho_{xy}, z, \omega)dz$ ($q = Ze$ is the ionic charge) as

$$u_3(0, \omega) \propto -\frac{(1+\nu)}{\pi}\beta h\langle\delta C_i\rangle \equiv -\frac{(1+\nu)}{\pi}\frac{\beta}{q}Q(\omega) . \tag{3.6}$$

Thus, the solution of the problem is reduced to finding the concentration change $\delta C_i(\rho_{xy}, z, t)$ ($\delta C_i(\rho_{xy}, z, \omega)$).

In case of a non-uniform electric field at the tip-surface junction, absence of the strain-diffusion coupling, and when ionic transport is controlled by ambipolar diffusion the Fick second law is used to describe the Li concentration change [3]

$$\frac{\partial}{\partial t}\delta C_i(x,t) = D\left(\frac{\partial^2}{\partial x_1^2} + \frac{\partial^2}{\partial x_2^2} + \frac{\partial^2}{\partial x_3^2}\right)\delta C_i(x,t) \tag{3.7}$$

with the following boundary conditions

$$\lambda\frac{\partial}{\partial x_3}\delta C_i(x_1,x_2,0,t) - \eta\delta C_i(x_1,x_2,0,t) = -V_0(x_1,x_2,t)$$
$$\delta C_i(x_1,x_2,x_3\to\infty,t)\to 0 \qquad , \tag{3.8}$$
$$\delta C_i(x,0) = 0$$

where D is the constant diffusion coefficient, and $V_0(x_1,x_2,t)$ is the electrostatic potential distribution at the tip-surface junction ($x_3 = 0$). [96] Phenomenological exchange coefficients λ and η correspond to the case of either fixed concentration ($\lambda = 0$) or fixed ionic flux ($\eta = 0$). The solution is

$$\delta C(k_1,k_2,x_3,t) = \frac{1}{2i\pi}\int_{A-i\infty}^{A+i\infty}ds\exp\left(-x_3\sqrt{k^2+s/D}+st\right)\frac{\overline{V}_0(k_1,k_2,s)}{\lambda\sqrt{k^2+s/D}+\eta}, \tag{3.9}$$

where k_i are coordinates of the Fourier transformation.

As one can see, the concentration change $\delta C_i(\rho_{xy},z,t)$ (and the final equations for the strain u_3 consequently) depends on the diffusion coefficient, which is essential for studying ionic dynamics by means of ESM in time and frequency domains and can be used to obtain the diffusion coefficient from the measured strain response.

Specific attention has to be paid to the boundary conditions, since in real experiments the tip-surface interfacial state, use of different cantilevers, and atmosphere conditions (e.g. vacuum, liquid environment, dry or humid atmosphere) affects the measured response.

In ESM, a SPM cantilever is a movable top electrode. Depending on the cantilever type and details of an experimental setup it can be either ion blocking (with a metallic coating in dry atmosphere) or partially reversible non blocking.

Ion blocking electrodes (cantilevers with Pt/It, Au, TiN, etc. coatings) are able to conduct electrons but not mobile ions. These cantilevers are preferable for ESM on Li-ion battery materials because they do not interact with Li ions. The blocking electrode employs the fixed concentration ($\lambda = 0$) boundary conditions.

Electrodes can be reversible if they transfer electrons and ions with low impedance. [97] In case when ESM measurements are performed by bare Si probes, or under ambient conditions with humidity > 30% when liquid wetting layer forms on the tip-surface junction, [3,98,99] or in Li-containing electrolyte the tip-electrode system may be considered as partially reversible. Interaction of the bare Si cantilever with Li ions should be partially reversible and results in rapid degradation of the cantilever due to formation of unstable chemical compounds (e.g. Si-Li) and their interaction with atmosphere gases and water. In

the idealized fully reversible case the non blocking electrode employs the fixed ionic flux ($\eta = 0$) boundary conditions. Blocking electrodes can be also rendered to reversible ones at high biases when Li extraction and tip plating inevitably occurs.

Note, that the simplification used in Eq. (3.4) stands for thin film samples when the field distribution is indeed axial (Figure 3.5). In case of thick samples the radially symmetric field distribution must be considered instead (Figure 3.5 (a)). In both cases the dependence of the displacement u_3 on the tip-surface contact area will be different.
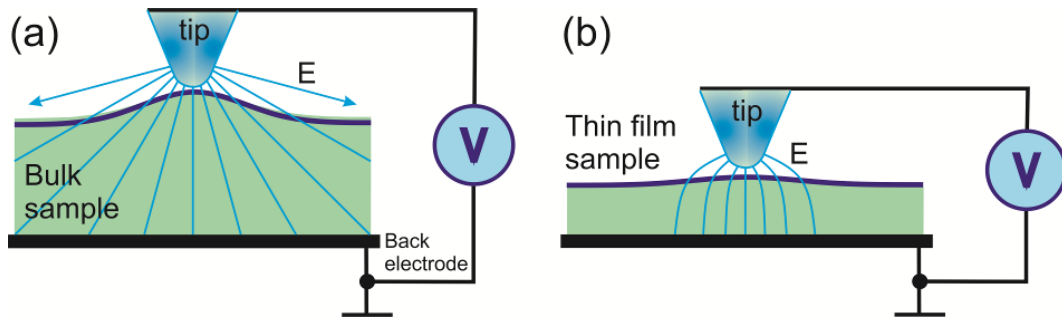
Figure 3.5. Electric field distribution in (a) a bulk sample where the sample thickness is much higher than the tip radius, and in (b) a thin film sample where the electric field is more confined between the tip and the counter electrode.

In all mentioned cases the electric field created by the probe is highly localized and the tip detects local deformations.

3.2.2 Spatial resolution

The spatial resolution of ESM can be estimated from the characteristic size of the area affected by the concentration change. Lateral resolution is defined as half width of the excited spatial region at half maximum (HWHM) (normalized to the tip size R_0) and is shown in Figure 3.6 as a function of frequency for the limiting cases of boundary conditions. Vertical resolution is defined as the maximum ESM response and is shown in Figure 3.7. Limiting cases for low and high frequency regimes can be classified depending on the value of $\omega\tau$ in relation to unity: [3]

1. Static or quasi-static regime, where the Li-diffusion length significantly exceeds the signal detection volume (tip radius), $\omega\tau \ll 1$.
2. Low frequency regime, when the Li-diffusion length is comparable to the tip radius, $\omega\tau \leq 1$.
3. High-frequency regime, when the Li-diffusion length is less than the tip radius, $\omega\tau \gg 1$.

The highest lateral resolution can be achieved in the high-frequency regime ($\omega\tau \gg 1$) when the diffusion length is less or about the tip radius, while the highest vertical resolution can be achieved in the quasi-static regime ($\omega\tau \ll 1$) when the volume affected by the concentration change is maximum. Attention should be paid to the signal-to-noise
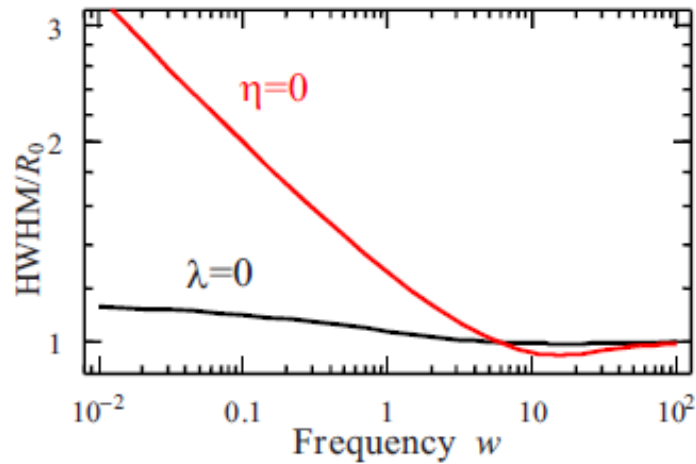
Figure 3.6. Frequency dependence of the excited spatial HWHM normalized by the tip size R_0 for boundary conditions with $\lambda=0$ and $\eta=0$. (Reproduced from Ref. 3)
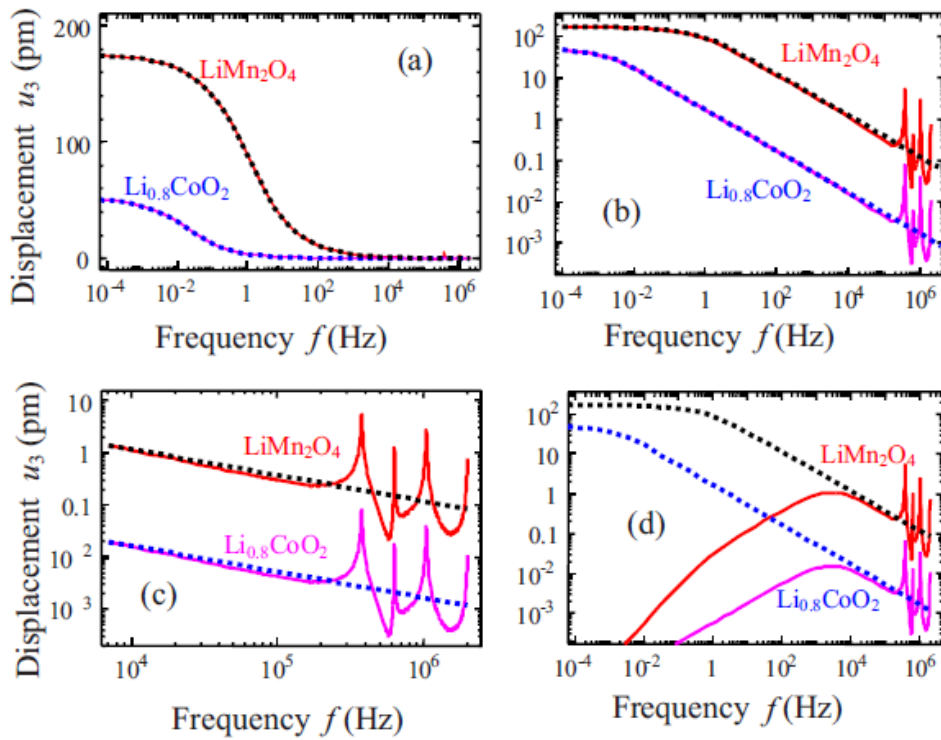
Figure 3.7. (a) and (b) Absolute values of the materials displacement (dotted curves) and the ESM response multiplied by the experimental transfer function (solid curves) vs driving frequency f for the determined concentration $\delta C_i / C_i^{max} = 0.05$ (i.e., $\lambda = 0$) for LiMn$_2$O$_4$ and Li$_{0.8}$CoO$_2$. (c) Zoom in the high-frequency regime. (d) Materials response (dotted curves) and signal to noise ratio for ESM response divided by noise function $\sim (f_0 / f + 1)$ with $f_0 = 3\,\text{kHz}$ (solid curves). (Reproduced from Ref. 3)

ratio (SNR) with the noise function $\sim (f_0/f + 1)$ for the ESM response multiplied by the experimental transfer function in Figure 3.7 (d): in order to avoid the flicker noise $\dfrac{1}{f}$, measurements should be performed at sufficiently high frequency.

3.2.3 ESM spectroscopies

ESM response represents the combined contribution of several factors and cannot be directly used to distinguish among different mechanisms involved in signal formation. It only illustrates how different elements of topography respond to the ac excitation, while understanding and interpretation of results require knowledge of actual mechanisms of the response.

Time spectroscopy

Studying of Li diffusion at the nanoscale is possible by measurement of a local ESM response as a function of time. Dynamics of the response reflect the instant changes of Li^+ concentration and, therefore, serves as a signature of the ionic mobility. It requires formation of the Li concentration gradient that can be easily created by an external electric field bias. These principles are used in ESM Time Spectroscopy (TS). [100] Figure 3.8 (a) illustrates the pulse application schematic of TS.

In this technique, a sequence of dc pulses is applied between a tip and a counter electrode, and the surface vibrations (ESM response) are typically measured after the dc pulses. Li drift velocity consists of field dependent and field independent components according to Equation [7]

$$\vec{\upsilon}_i = \frac{D_i}{k_B T}\left(\nabla \mu_i + z_i F \nabla \varphi\right), \tag{3.10}$$

where D_i is the ionic diffusion coefficient, k_B is the Boltzmann constant, T is the temperature, μ_i is the chemical potential, z_i is the ionic charge, F is the Faraday constant, and φ is the electric potential. When the dc voltage is on, Li^+ ions migrate under the electric potential gradient $\nabla \varphi$ towards or outwards the tip in order to compensate the external electric field, thus shifting the sample from the initial thermodynamically stable state to a new state with inhomogeneous Li concentration distribution. This redistribution is controlled by both migration and diffusion mechanisms. [74] As a result, the Li concentration gradient defined by the amplitude and the time of the applied dc pulse is created below the tip. After the dc bias is off, the Li^+ ions diffuse back (relaxation) bringing the sample from the inhomogeneous concentration state into the initial equilibrium state under the resulting chemical potential gradient $\nabla \mu_i$. Simultaneous ac probing of the ESM response after the dc pulse (dc off state) represents dynamics of the local deformation and presumably Li^+ concentration (this assumption is correct if only C_i changes, while temperature, contact area, diffusion coefficient and voltage remain
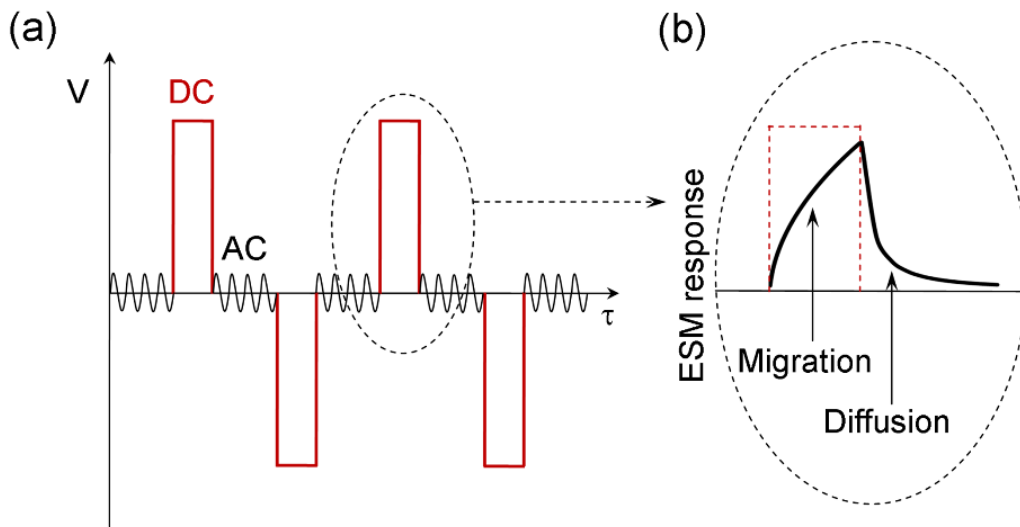
Figure 3.8. Schematic representation of time spectroscopy. (a) Sequence of dc pulses and ac probe between the dc; (b) schematic illustration of the measured ESM response.

constant, and non-Vegard's contributions can be neglected). Shape of the ESM relaxation response is schematically represented in Figure 3.8 (b). Fitting the experimental curves with an appropriate physical model allows estimating local Li diffusion coefficient in a studied material.

To minimize irreversible changes of concentration and injected charges, a sequence of positive and negative dc pulses of the same magnitude is commonly applied. Initial ESM response should be measured before the first dc pulse to record the reference response (initial state). Dc pulse magnitude and time should be small enough to activate only reversible processes.

Before further description, one must clearly distinguish difference between the *dc mediated ionic migration and diffusion* and the *ac mediated oscillating surface displacements probed by SPM (ESM response)*. In TS increasing/decreasing ESM response represents the dc mediated migration and diffusion processes of mobile ions through the oscillating strain. Remember that the true mechanism of the ESM response that links the detected ac mediated strain to the ionic mobility/concentration below the tip is not fully understood. We will discuss this issue later in Chapter 6.

Solutions for the dc mediated strain and its relaxation in time domain were obtained by using Fick's second law (see Eq. 3.7 and 3.8), assuming absence of strain-diffusion coupling, the constant diffusion coefficient, and the negligible thermal expansion effect. [3] For the rectangle dc pulse with t_0 pulse time and in the case of fixed concentration boundary condition ($\lambda = 0$) the solution for the static case ($\omega=0$) is following: [3, 93]

$$u_3\left(0, t < t_0\right) \approx -\left(1 + \nu\right) \frac{4\beta V_a}{\eta\sqrt{\pi}} \sqrt{Dt} \propto t^{1/2}$$

$$u_3\left(0, t >> t_0\right) \approx -\left(1 + \nu\right) \frac{\beta V_a R_0^2 t_0}{6\eta t^{3/2}\sqrt{\pi D}} \propto t^{-3/2} \qquad (3.11)$$

where u_3 is the elastic strain, β is the Vegard coefficient, ν is the Poisson ratio, and R_0 is the tip-surface contact area.

In the classic diffusion theory the exponent i in the power law $t^{-i/2}$ at $t>>t_0$ determines the dimension of diffusion: $i=1$ for 1D, 2 for 2D, and 3 for 3D and experimentally can indicate reduction/increase of the diffusion dimension, i.e. local diffusion anisotropy.

For the same dc pulse in the case of fixed flux boundary condition ($\eta = 0$) the solution for the static case ($\omega=0$) is following: [3,96]

$$u_3\left(0, t < t_0\right) \approx -\left(1 + \nu\right)\beta V_a \frac{R_0^2}{4\lambda} \ln\left(1 + \frac{8Dt}{R_0^2}\right)$$

$$u_3\left(0, t > t_0\right) \approx -\left(1 + \nu\right)\beta V_a \frac{R_0^2}{4\lambda} \ln\left(\frac{R_0^2 + 8Dt}{R_0^2 + 8D(t - t_0)}\right) \qquad (3.12)$$

Time dependent solutions for the dynamic strain (ESM, $\omega \neq 0$) have not been derived yet.

Voltage spectroscopy

Further insight into Li dynamics can be done by means of the voltage spectroscopy. [101,102] In this method, a series of dc pulses (sketched in Figure 3.9) is applied between a tip and a counter electrode, and the resulting ESM response is probed after each dc pulse by applying a periodic ac voltage. Measured ESM amplitudes are plotted versus corresponding dc voltages. As the field induced Li^+ concentration increases/decreases below the tip, the induced displacement increases/decreases correspondingly. Short time between pulses prevents full displacement relaxation after each pulse (diffusion relaxation time is in the 0.1–1 s range for the probed volume and for typical diffusion coefficients 10^{-14}–10^{-12} m^2s^{-1}), thus electrochemical hysteresis loops can be observed, resembling the piezoresponse hysteresis loops in ferroelectric materials. [103] In contrast to ferroelectrics where hysteresis is a signature of polarization switching, ESM loops represent a variation of Li^+ concentration/mobility following the dc cycling.

The loop is open only when significant Li redistribution occurs during dc pulses. It is possible if there are mobile Li ions in the probed volume. [104] Loop opening strongly depends on the dc sweep frequency and can be understood from a simple mechanism. If the frequency is much higher than the Li inverse diffusion frequency in the probed volume $\frac{1}{\tau} = \frac{D}{l^2}$ than the Li redistribution during the dc sweep is small, measured ESM response is almost constant and the loop is closed. When the frequency decreases and becomes
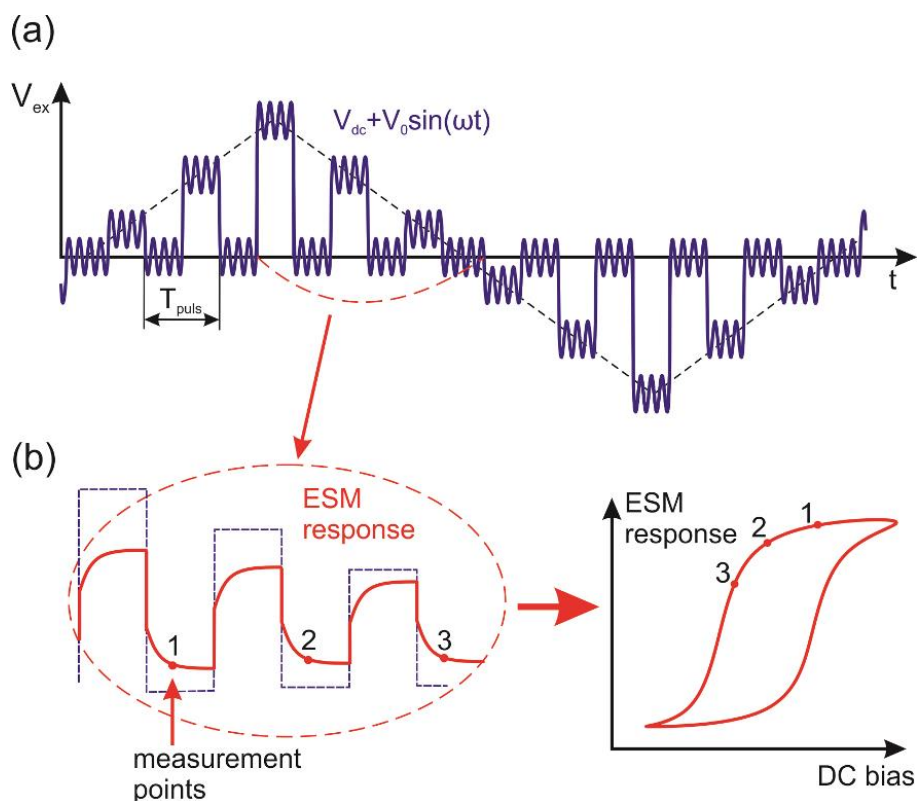
Figure 3.9. Voltage spectroscopy: (a) schematic of dc and ac pulses, (b) schematic of response and loop formation.

comparable with the Li diffusion frequency $\frac{1}{\tau} = 1\text{–}10$ Hz in the probed volume, Li redistribution in the probed volume is significant, but there is a lag between the Li concentration change and the electric field, and the loop opens. If the sweep frequency is much lower than the Li diffusion time, then Li redistribution occurs in a volume that significantly bigger than the probed one, and the loop saturates, closes and becomes S-shaped. [104]

The applied dc pulses should be limited in time and amplitude in order to prevent possible irreversible changes that might arise for sufficiently high and long voltage pulses. These values depend on many parameters such as tip material, humidity, sample's surface state and should be determined empirically before measurements.

A certain threshold dc voltage is needed in order to initiate Li redistribution. Apart of that, in electrochemically active systems there is a concentration limit for mobile ions, i.e. ESM response reaches saturation after a certain dc pulse amplitude. Figure 3.10 schematically illustrates effect of the threshold voltage and the concentration saturation on the loop shape.

Figure 3.11 is a striking illustration of the dependence of loop opening on mobile Li concentration below the tip. The measurements were done over the test solid-state battery structure consisting of partially overlapped layers of the $LiCoO_2$ cathode, the LiPON electrolyte, and the Si anode. [104] Loops from the anode deposited directly on the Al current
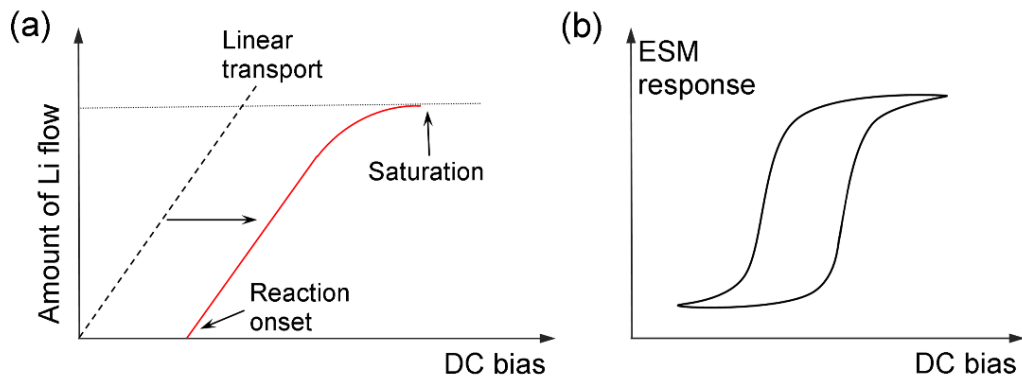
Figure 3.10. Schematic illustration of the Li-redistribution as a function of the maximum bias pulse. In presence of the reaction limitation, the process is linear above a certain threshold bias and saturates at the intercalation limit. (b) The expected hysteretic response. (Adopted from Ref. [104])

collector are completely closed, while loops from the full battery structure are open. These results clearly demonstrate that the ESM response and the voltage spectroscopy hysteresis loops are representative for the electrochemical processes below the tip.
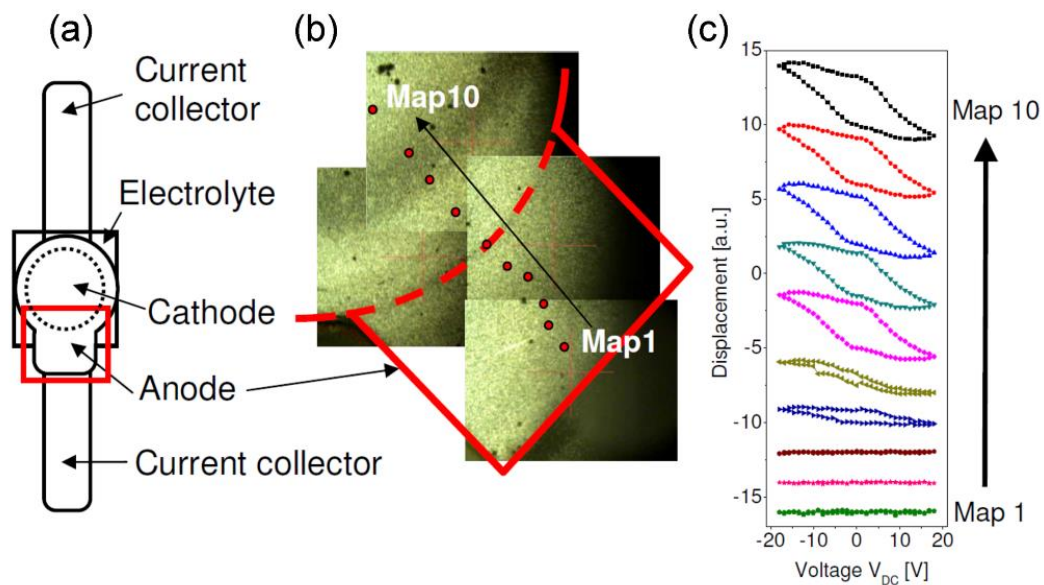
Figure 3.11. (a) Layout of the battery device, illustrating the relative position of LiCoO$_2$ cathode, LiPON electrolyte, and Si anode layers. (b) Combination of the optical micrographs of the battery surface acquired through an AFM digital camera system, illustrating the location of measurement. (c) Measured responses (shifted along the y-axis for better visibility) illustrating the lack of electromechanical activity on a bare anode surface and strong hysteretic responses in the regions where underlying LiPON and cathode materials are present. (Reproduced from Ref. [104])

3.2.4 Non-Vegard contributions

Besides the Vegard ESM response u, a number of other – non-Vegard – contributions to the measured signal $A_{1\omega}$ is possible: [95]

$$A_{1\omega} \propto -\frac{(1+\nu)}{\pi}h\left(\left(\beta - \frac{2q}{\varepsilon_0}f_{33}\right)\langle\delta C_i(t)\rangle + \Xi_{33}^C\langle\delta n(t)\rangle + \Xi_{33}^V\langle\delta p(t)\rangle + \frac{\tilde{Q}_{33}k_B T}{2\varepsilon_0}\langle E_3^2\rangle\right) +$$

$$\frac{1}{\tilde{k}}\frac{\partial C}{\partial z}(V_{dc} + V_{CPD})V_{ac} + d_{33}V_{ac} \qquad ,(3.13)$$

where ν is the Poisson coefficient, h is the film thickness (in case of a thin film sample), $\left(\beta - \dfrac{2q}{\varepsilon_0}f_{33}\right)$ is the renormalized Vegard coefficient including the flexoelectric strain tensor component f_{33}, Ξ_{33}^C and Ξ_{33}^V are deformation potential tensors for electron and hole's contributions correspondingly, $\tilde{Q}_{33}$ is the electrostriction coefficient, $E_3 = -\dfrac{\partial\varphi(z)}{\partial z}$ is the electric field distribution, $\dfrac{1}{\tilde{k}}\dfrac{\partial C}{\partial z}(V_{DC} - V_{CPD})V_{AC}$ is the electrostatic contribution, [103] V_{CPD} is the contact potential difference between the tip and the sample, and $d_{33}^{eff}V_{AC}$ is the piezoresponse. [103] $\langle\delta C_i(t)\rangle$, $\langle\delta n(t)\rangle$, and $\langle\delta p(t)\rangle$ are concentration variations of ions, electrons, and holes as a function of the applied voltage V_{ac} (for example, $\langle\delta C_i(t)\rangle \propto \dfrac{eC_i D_i V_{ac}}{fk_B T R_0}$). In case of multiple types of mobile ions the Vegard contribution is $\sum_{i=1}^{\tilde{N}}\beta_i\langle\delta C_i(t)\rangle$, where $\tilde{N}$ is a number of types of mobile ions.

Ferroelectric (and piezoelectric) contribution is common in noncentrosymmetric materials and is typically higher than the ESM response controlled by the Vegard deformation. The electrochemically active cathode and anode materials used in Li-ion cells are usually not piezoactive. Commercial battery anodes and cathodes are typically composites containing active particles within the PVDF binder enriched with conductive nanoparticles. The PVDF binder could show stronger piezoresponse then the ESM response from active particles containing mobile Li ions ($LiMn_2O_4$, $LiCoO_2$, etc.). [105]

Ferroelectric response is polar in nature. Polarization switching during voltage spectroscopy results in the characteristic butterfly-like shape of the amplitude hysteresis loop and 180° phase switching. Conversely, the ESM amplitude loop has different shape and its phase does not switch to 180° due to non-polar nature of the Vegard strain response, which depends only on Li concentration [106] (Figure 3.12).

Flexoelectricity is a spontaneous electrical polarization induced by the strain gradient. The flexoelectric contribution is common for both centrosymmetric and non-centrosymmetric materials and typically an order of magnitude smaller than the Vegard
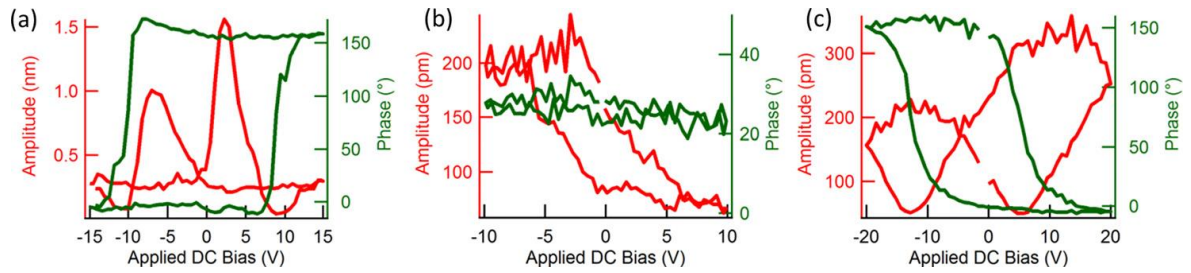
Figure 3.12. Phase-voltage and amplitude-voltage loops from (a) piezoactive PZT, (b) non-piezoactive Li conductive LFP and (c) soda-lime glass. (Reproduced from Ref. [106])

contribution. [95]

The electrostatic signal contributes to the measured response in the dc on state, but can be easily identified as a linear function of bias and subtracted. [103,107] Moreover, the electrostatic contribution is inversely proportional to the cantilever spring constant and can be suppressed by using sufficiently stiff cantilevers. In the dc off state it should be zero unless the contact potential difference V_{CPD} between the tip and the sample is present. Electrostatic contribution due to the contact potential difference does not change the hysteresis loop shape measured in the off-field state. [103] It just shifts the whole loop along the ESM response axis causing an offset which depends on the tip electrode material. However, this is not always true and will be discussed in details in Chapter 6.

The electrostriction contribution can significantly affect the ESM response, but only in the dc on mode. In the dc off mode it exists at the double modulation frequency and does not contribute to the ESM response unless a background dc of any nature is present. [95]

Numerical calculations performed for $LiCoO_2$ and $LiMn_2O_4$ systems with ion-blocking boundary conditions show displacements much below 1 pm for frequencies above 10^4 Hz even though a relatively high Li diffusion coefficient of 10^{-13}-10^{-14} m^2s^{-1} was used. [108,90] A mean oscillation path for the ions smaller than the distance between two interstitials was calculated, meaning that the diffusion-based model cannot be applied in this case. However, the ESM signal induced by lithium ions is experimentally detected at frequencies 200-400 kHz as was described above in this Chapter. This fact arises a question about the true nature of the ESM response.

Chapter 4

Experimental

4.1   Sample preparation

All samples studied in this work were prepared and characterized by XRD, ICP-OES, SEM, and EBSD by Mr. Hugues-Yanis Amanieu and colleagues at the Corporate Research business unit of Robert Bosch GmbH in Gerlingen-Schillerhoehe, Germany within the FP7 Marie Curie Initial Training Network "Nanomotion" project collaboration.

In order to investigate degradation mechanisms of $LiMn_2O_4$ cathodes and graphite anodes caused by intensive cycling at high C rates, we compared samples from non-cycled and cycled down to 80% state of health (SOH) batteries. The batteries are commercial 18650 Li-ion cells with $LiMn_2O_4$ cathodes and graphitic anodes and a typical capacity of 1200 mAh. Three cells (termed "fresh" further in the text) were completely discharged at 1C-rate in the CC/CV mode down to 2.3 V with a stop current of 0.2C-rate. The first of these cells was maintained at 0% state of charge (SOC), the second cell was charged at 1C-rate up to 50% SOC, the third one was charged at 1C-rate up to 100% SOC. Another three cells (termed "fatigued" further in the text) were cycled being charged at 2 A (slightly more than 1C-rate) and discharged at 16C-rate (Figure 4.1). After fatigue down to 80% SOH (Figure 4.2) they were cycled 3 times at 1C-rate and finally completely discharged at 1C-rate. After that, one cell was maintained at 0% SOC and the other two were charged at 1C-rate up to 50% SOC and 100% SOC similar to the fresh ones. The $LiMn_2O_4$ cathodes with the Al current collector and the graphitic anodes with the Cu current collector were extracted in a glove box in Ar atmosphere and washed in dimethyl carbonate in order to remove the electrolyte. [109]

The extracted samples are complex composites consisting of the Al/Cu current collector, $LiMn_2O_4$/graphite active particles, and the soft polymer PVDF binder enriched with carbon black nanoparticles. Figure 4.3 illustrates element mapping obtained on $LiMn_2O_4$ cathodes using Scanning Electron Microscopy (SEM) with Energy Dispersive X-ray Spectroscopy (EDS). Preliminary X-Ray diffraction (XRD) measurements showed that
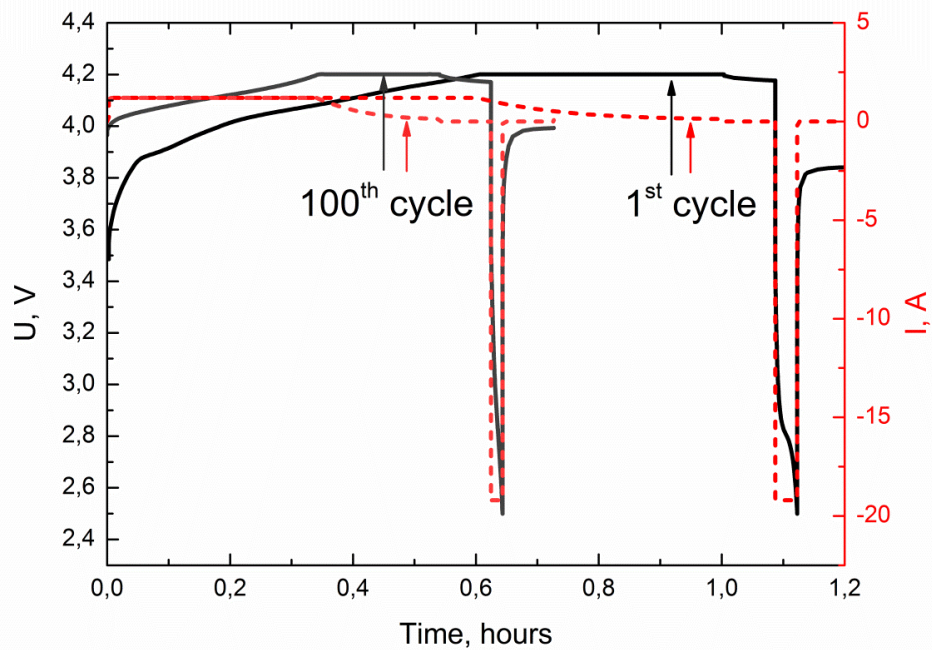
Figure 4.1. Charge-discharge curves of the fatigued to 80% SOH sample for the 1st and the 100th cycles. Battery was charged in the CC/CV mode at 2 A current until voltage reached 4.2 V and then discharged at 16C-rate. (Reproduced from Ref. [109])
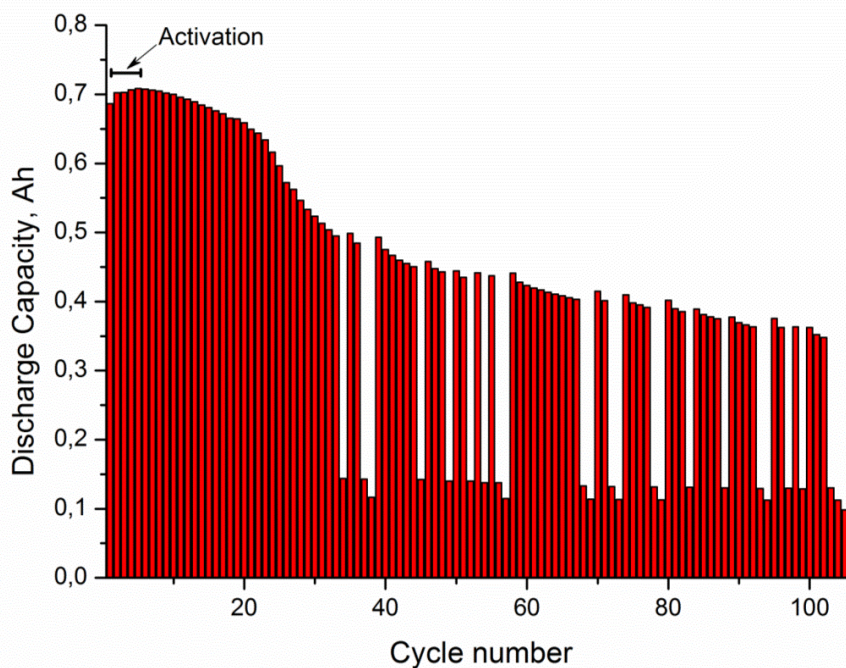
Figure 4.2. Discharge capacity versus cycle number of the fatigued cell at 16C discharge rate. The 5 first cycles present a capacity increase due to activation of the cell. The very low capacities at some points are due to the failure with the cycling instrument. SOH was determined as a capacity loss at 1C-rate – not shown. (courtesy of ZSW) (Reproduced from Ref. [109])
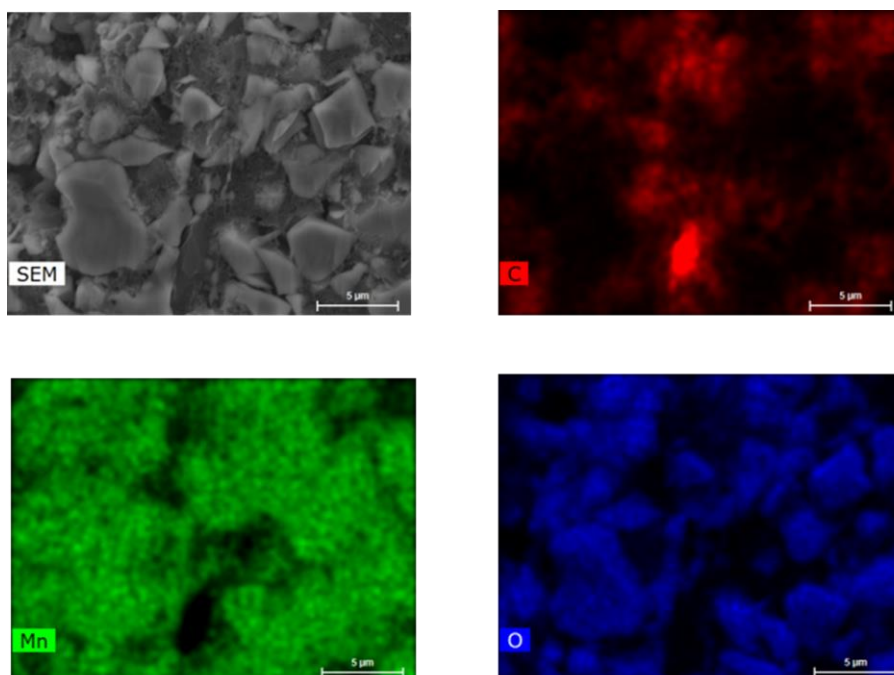
Figure 4.3. SEM image and EDS spectra of the washed LiMn$_2$O$_4$ cathode. C, Mn, and O letters on images correspond to distribution of carbon, manganese, and oxygen.

all Li$_x$Mn$_2$O$_4$ samples possess the spinel cubic structure (Fd$\overline{3}$m space group). Inductively coupled plasma optical emission spectrometry (ICP-OES) showed the Li/Mn ratio within the cubic spinel phase range. Results are summarized in Table 4.1. It should be noted that ICP-OES cannot distinguish the origin of different elements. It is hence possible that lithium were present as impurities (secondary electrolyte interface, rest of electrolyte salts, etc.), increasing the overall ratio.

After preliminary characterization the samples were embedded in a soft and compliant epoxy resin, sequentially polished with 1200–4000 silicon carbide sand paper, 3 μm and 1 μm diamond paste, and Struers OP-S suspension. Resulting surface is shown in Figure 4.4. The mechanically polished samples were finally polished by an Ar ion beam: 15 min cleaning at a 10° angle and 30 min polishing at a 4° angle. PVDF was completely sputtered off the surface.

4.2   Experimental setup

ESM measurements were performed using a commercial AFM (Solver Next, NT-MDT – Figure 4.5) working under ambient conditions (RH≈40%) in the ESM mode. Pt/Ir coated cantilevers of the same type with ≈5 N/m stiffness and ≈130 kHz fundamental resonance frequency were used as external movable electrodes. Before measurements they were tested using a periodically poled lithium niobate (PPLN) test sample. The samples were grounded through the metallic current collectors serving as counter electrodes. Each

active particle ($Li_xMn_2O_4$ or graphite) was electrically connected to the metallic current collector (Al for the cathode and Cu for the anode) through the conductive carbon black

Table 4.1. Samples

№ of sample	Composition	SOH, %	SOC, %	Lattice parameter, Å	Li/Mn ratio
1	$Li_xMn_2O_4$	100	0	8.1779	0.94/2
2	Graphite	100	0	-	-
3	$Li_xMn_2O_4$	100	50	8.1406	0.75/2[*]
4	$Li_xMn_2O_4$	100	100	8.092	0.61/2
5	$Li_xMn_2O_4$	80	0	8.1791	0.89/2
6	Graphite	80	0	-	-
7	$Li_xMn_2O_4$	78	50	8.1352	0.756/2
8	Graphite	78	50	-	-
9	$Li_xMn_2O_4$[**]	78	100	8.1104	0.65/2
10	$LiMn_2O_4$ thin film	n/a	n/a	8.1866	-

[*] the Li/Mn ratio is estimated from the lattice parameter

[**] the cell is unchargable, stopped at 4.08 V

within the PVDF. Driving ac voltage with 3 V amplitude was applied between the cantilever and the counter electrode using the internal source of the microscope ($\leq$10 V). Parameters of dc pulses for ESM spectroscopies are presented in Chapter 6. Measurements were conducted below the first cantilever-surface contact resonance in the frequency range where no spurious peaks were observed, until different is specifically stated. ESM response was measured by means of the internal lock-in amplifier of the microscope as the first harmonic of the laser beam deflection.

KPFM measurements were performed in the 2-pass AM-KPFM mode using the same microscope under ambient conditions. The samples were grounded through the metallic current collector serving as a counter electrode. Ac voltage of the second pass was 0.5 V in amplitude, the 2nd pass lifting height was always 15 nm; scan resolution was 256×256 points. Pt/Ir coated cantilevers (NTMDT NSG10, resonance frequency = 249.4 kHz, force constant = 11.8 N·m^{-1}) were used. Before measurements the cantilevers were

calibrated using a highly oriented pyrolytic graphite (HOPG) test sample and a thin Ag film sputtered on a Si substrate.
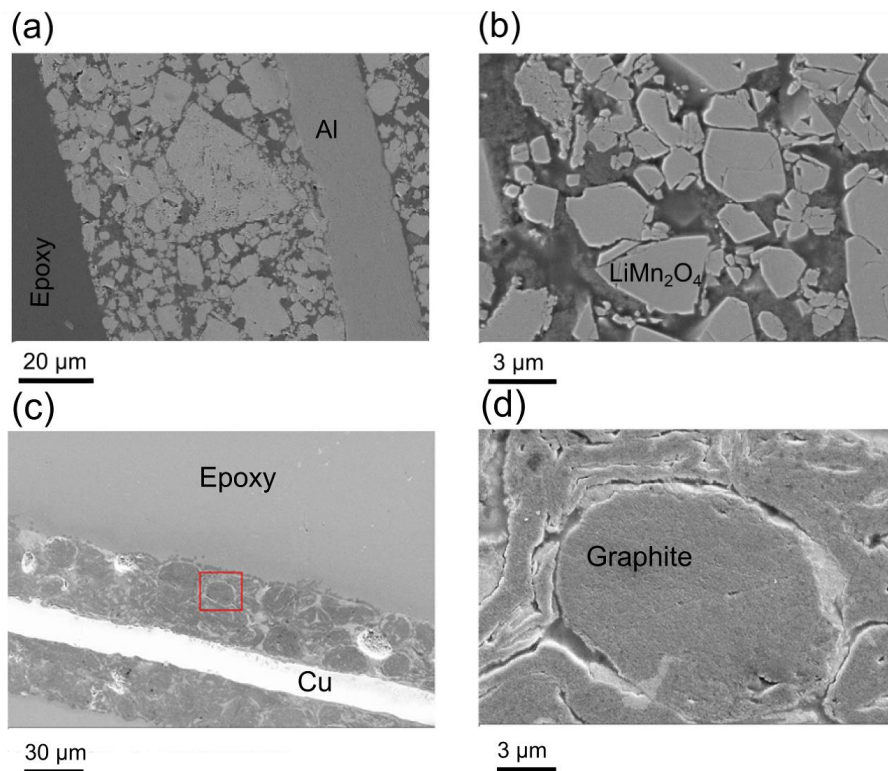
Figure 4.4. SEM images of cross-sections of the $LiMn_2O_4$ cathode (a, b) and graphite anodes (c, d). Courtesy of Robert Bosch GmbH, Corporate Research.
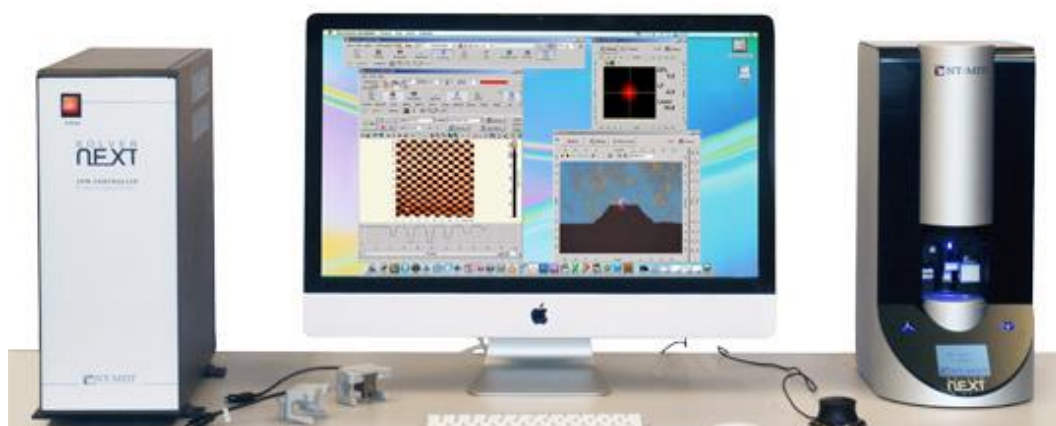
Figure 4.5. Solver Next scanning probe microscope. (Reproduced from Ref. [110])

- 45 -

Chapter 5

Single- and multi-frequency detection of surface displacements via ESM

Estimated vertical surface deformations measured in ESM are ranging from 10^{-2} pm to tens picometers. [3] Implemented in ESM lock-in amplification allows detecting surface displacements with the vertical resolution down to several pm. However, this is at the limit of the AFM's resolution. Up to now the ESM method has been implemented in multi-frequency modes [111] such as Band Excitation (BE) [112] and Dual AC Resonance Tracking (DART) [113] in order to amplify sufficiently low ionic mediated displacements at the cantilever resonance. Despite the fact that the BE and DART techniques were introduced more than 7 years ago, their noise performance has not been carefully analyzed yet.

In this work we implemented ESM in the single frequency detection mode without the resonance amplification for the first time, so it is prerequisite to compare its noise performance with the earlier used multi-frequency methods.

In order to prove efficiency of the single frequency approach for ESM measurements, in this Chapter we first analyzed noise performance of the multi-frequency detection modes and compared it with the conventional single-frequency detection mode. We established the dependence of the signal-to-noise ratio on cantilever parameters and noise in the AFM system. Finally, we demonstrated that the ESM response can be measured off the resonance using a commercial AFM system.

5.1 Band Excitation mode

Band Excitation was recently introduced as an universal alternative to the traditional single-frequency detection that allows quantitative studies of dissipative and conservative phenomena of a tip in contact with surface, and thus can be applied virtually to all SPM methods. In this method, both excitation and detection are performed using a driving signal having defined amplitude and phase content in a given frequency interval

across the contact resonance. This allows efficient use of the resonance amplification, avoiding artifacts due to changes in the resonance frequency and the quality factor Q as a function of a probe position, bias, or surface properties. [112] Figure 5.1 illustrates the first contact resonance shift over a composite sample surface recorded in the BE mode.
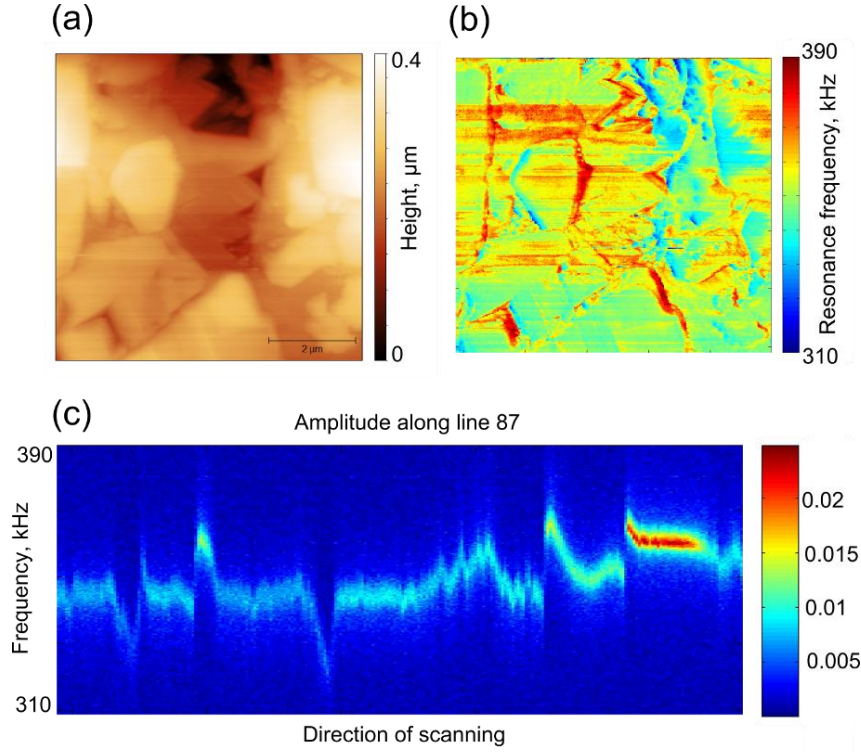
Figure 5.1. Shift of the contact resonance frequency during scanning of a LiMn$_2$O$_4$ cathode: (a) surface topography, (b) the resonance frequency map, (c) shift of the resonance frequency along the single line. (This image was obtained at the CNMS ORNL (project CNMS2013-130))

Analytical expression $x(t)$ for the BE excitation signal in time domain can be found by Fourier transformation of the Heaviside step function $\left(\theta(\omega-\omega_L)-\theta(\omega-\omega_U)\right)$ (Figure 5.2 (b)):

$$x(t) = \frac{1}{2\pi}\int_{-\infty}^{+\infty}\left(\theta(\tilde{\omega}-\omega_L)-\theta(\tilde{\omega}-\omega_U)\right)\exp(i\tilde{\omega}t)d\tilde{\omega} =$$
$$= \frac{\Delta\omega_{BE}}{2\pi}\mathrm{sinc}(\frac{\Delta\omega_{BE}}{2}\cdot t)\cdot\exp\left(i\frac{(\omega_U+\omega_L)}{2}t\right) \qquad (5.1)$$

where $\Delta\omega_{BE} = \omega_U - \omega_L$ is the bandwidth of the BE signal, $\theta(x)$ is the Heaviside step function, $\exp\left(i\frac{(\omega_U+\omega_L)}{2}t\right)$ is the carrier signal with the frequency $\frac{\omega_U+\omega_L}{2}$ and $\frac{\Delta\omega_{BE}}{2\pi}\mathrm{sinc}(\frac{\Delta\omega_{BE}}{2}\cdot t)$ is the modulation signal with the modulation frequency $\frac{\Delta\omega_{BE}}{2}$.
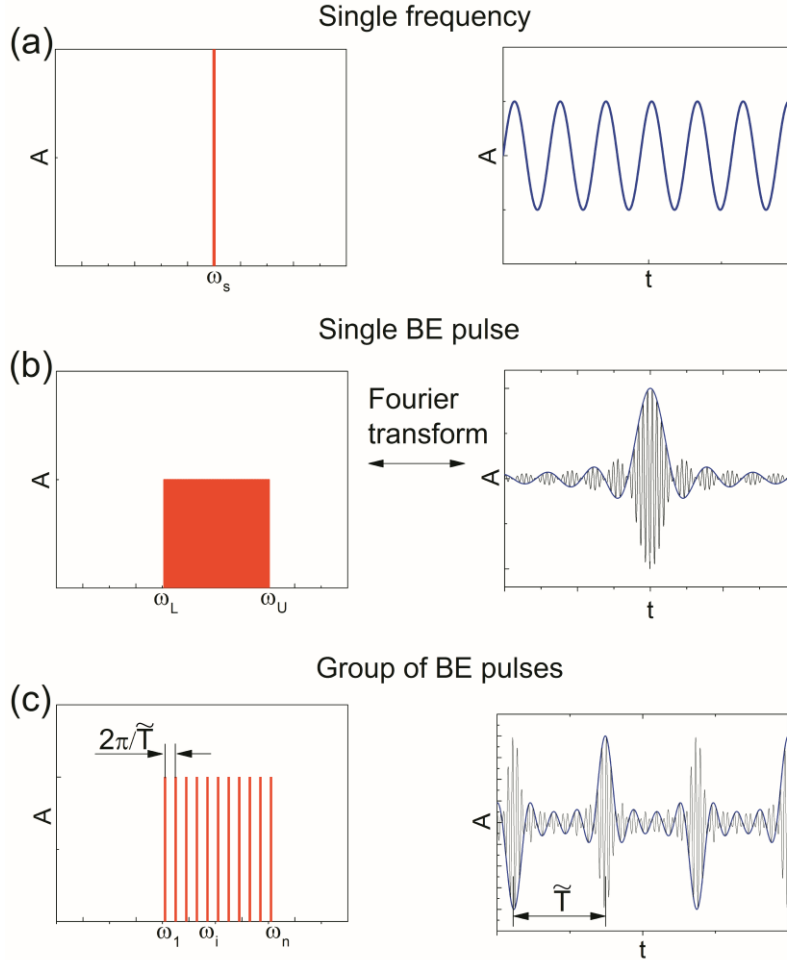
Figure 5.2. Excitation signals of BE mode in comparison with the single frequency detection method in time (right figures) and frequency domains (left figures). (a) Single harmonic signal for the single frequency mode. (b) BE pulse has spectral density uniformly distributed within BE band. (c) Group of the BE pulses has discrete spectrum with spectral density at each spectral point higher than spectral density of a single BE pulse but lower than a single harmonic signal (a). (Reproduced from Ref. [114])

Infinite in time domain Sinc excitation signal (Eq. 5.1) has a rectangular continuous spectral density and zero shift phase content. Energy of the Sinc excitation is concentrated in one pulse for a short period of time $\sim \dfrac{2\pi}{\Delta\omega_{BE}}$ during which all excitation energy can be transferred to the sample.

Another type of BE excitation signal is the Chirp excitation $V_0 \sin(\varphi \cdot t^2)$ – which is the phase modulated signal with the fixed amplitude V_0 with a rectangular type of spectral density and a quadratic phase content. Energy of the Chirp excitation signal is distributed more continuously within the pulse duration and, consequently, for the same injected energy has much lower electric field at the maximum. Preferable type of excitation can be selected for a specific task. The desired energy distribution in the time domain can

be obtained by tuning the phase content of the signal from the Sinc to the Chirp type of excitation.

5.2 Signal-to-noise ratio and vertical resolution

Noise in the Atomic Force Microscopy consists of the cantilever thermal noise, the tip-surface interaction noise, and the instrumental noise of detection and signal processing systems (Figure 5.3). [115] Therefore, the power spectral density of the total displacement signal noise can be expressed as $D_{tot}^z = D_{th}^z + D_{ds}^z$, where D_{th}^z and D_{ds}^z are the thermal and the detection-system contributions, respectively.
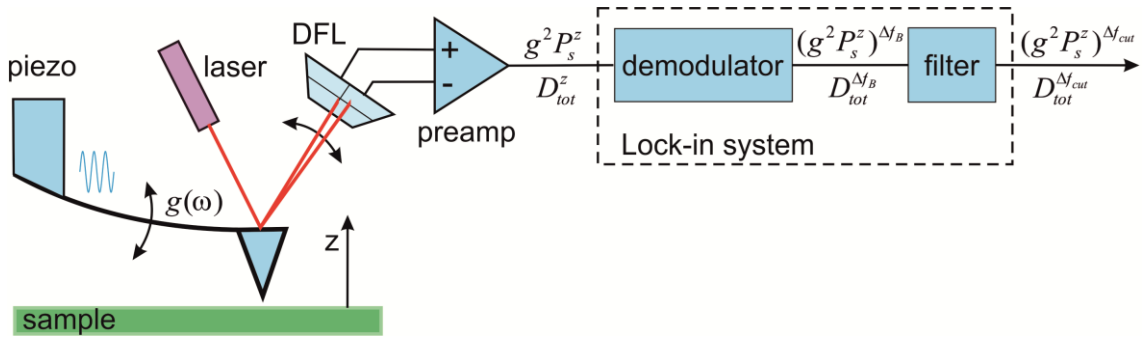
Figure 5.3. Schematic presentation of the signal path in AFM detection and lock-in system. The quantities P_s^z and $(g^2 P_s^z)^{\Delta f}$ describe the input and output signals of the lock-in and AFM system. $D_{tot}^z = D_{th}^z + D_{ds}^z$ and $D_{tot}^{\Delta f}$ are the corresponding noise power spectral densities superimposed on the ESM/PFM signal and $g(\omega)$ is the frequency response function of the cantilever. (Reproduced from Ref. [114])

Electrical and optical components of the detection system produce noise that typically overlays the ionic displacement (ESM) signal.

Single frequency

Effect of the cantilever resonance amplification can be considered using a simple harmonic oscillator (SHO) model. Around the first contact resonance the frequency response function of a cantilever can be approximated by the frequency response function of SHO. Solution of the SHO equations for a single sinusoidal excitation $\ddot{z} + 2\delta\dot{z} + \omega_0^2 z = \omega_0^2 A^{max} \sin(\omega t)$ with the amplitude A^{max} and the frequency ω is:

$$z(t) = A(\omega)\sin(\omega t + \varphi), \tag{5.2}$$

where the response amplitude A and the phase φ are defined by equations:

$$A(\omega) = A^{\max} \cdot g(\omega) = \frac{A^{\max}\,\omega_0^2}{\sqrt{(\omega^2 - \omega_0^2)^2 + (\omega\omega_0/Q)^2}} \; .$$

$$\tan(\varphi(\omega)) = \frac{\omega\omega_0/Q}{\omega^2 - \omega_0^2}$$

(5.3)

Here $\omega_0 = 2\pi f_0$ is the resonance frequency, $Q = \dfrac{\omega_0}{2\delta}$ is the quality factor, and $g(\omega)$ is the frequency response function of SHO. For an arbitrary excitation signal $s(t)$ the expression for $z(t)$ is the integral of the frequency response function with the amplitude spectral density of the excitation signal $s(\omega)$:

$$z(t) = \frac{1}{2\pi}\int s(\omega)g(\omega)\sin(\omega t + \vartheta(\omega) + \varphi(\omega))d\omega = \frac{1}{2\pi}\int z(\omega)\sin(\omega t + \phi(\omega))d\omega \, , \quad (5.4)$$

where $\vartheta(\omega)$ is the phase of $s(\omega)$. Spectrum of the cantilever vibrations $z(t)$ is

$$z(\omega) = g(\omega) \cdot s(\omega) \tag{5.5}$$

According to the equipartition theorem [116]

$$\frac{1}{2}k\left\langle z^2(t)\right\rangle = \frac{1}{2}k_B T \, , \tag{5.6}$$

where $\left\langle z^2(t)\right\rangle$ is the cantilever mean-square displacement, k is the static stiffness of the cantilever, k_B is the Boltzmann constant, and T is temperature. The total mean square cantilever displacement and the power spectral density of the cantilever thermal noise $D_{th}^z(\omega) = z_{th}^2(\omega)$ are related to each other as

$$\left\langle z^2(t)\right\rangle = \frac{1}{2\pi}\int\limits_0^\infty D_{th}^z(\omega)d\omega \, . \tag{5.7}$$

The power spectral density of the cantilever thermal noise $D_{th}^z(\omega)$ with the constant thermal excitation spectral density ψ (white noise) can be written as $D_{th}^z(\omega) = \dfrac{2}{k}g^2(\omega)\cdot\psi$, where $\psi = \dfrac{2k_B T}{\omega_0 Q}$. [115]

Using Equations (5.4) – (5.7), the $SNR = \dfrac{P_{signal}}{P_{noise}}$ in the frequency range from ω_L to ω_U before processing is:

$$SNR = \frac{\dfrac{1}{2\pi}\int\limits_{\omega_L}^{\omega_U} g^2(\omega)s^2(\omega)d\omega}{\dfrac{1}{2\pi}\int\limits_{\omega_L}^{\omega_U}\left(g^2(\omega)\dfrac{4k_B T}{\omega_0 Qk} + D_{ds}^z\right)d\omega} = \frac{\dfrac{1}{2\pi}\int\limits_{\omega_L}^{\omega_U} g^2(\omega)s^2(\omega)d\omega}{\left(\dfrac{k_B T/k}{\Delta f D_{ds}^z} + 1\right)\Delta f_B D_{ds}^z} \, , \tag{5.8}$$

where $\Delta\omega_B = \omega_U - \omega_L = 2\pi\Delta f_B$ is the bandwidth of the system, integral $\int_{\omega_L}^{\omega_U} g^2(\omega)d\omega$ at

$\omega_U \gg \omega_0$ and $\omega_L = 0$ is equal to $\approx \int_0^\infty g^2(\omega)d\omega = \frac{\pi}{2}Q\omega_0$. For the sinusoidal (one

harmonic) response signal $s^2(\omega) = 2\pi P_s \cdot \delta(\omega - \omega_s)$ the SNR at the driving frequency

$\omega_s < \omega_U$ before processing can be written as:

$$SNR(\omega) = \frac{P_s}{P_{ds}^z}\frac{g^2(\omega_s)}{\left(\dfrac{k_BT/k}{\Delta f_B D_{ds}^z}+1\right)},\tag{5.9}$$

where P_s is the power of the measured response, and $P_{ds}^z = D_{ds}^z \Delta f_B$ is the power of the detection system noise in the system bandwidth.

After using a low-pass filter in a lock-in amplifier with the cutoff frequency

$\omega_{cut} = 2\pi f_{cut} \ll \dfrac{\omega_0}{Q}$, the integral $\int_{\omega_L}^{\omega_U} g^2(\tilde{\omega})d\tilde{\omega}$ converts to

$$\frac{1}{2\pi}\int_{\omega-\frac{\omega_{cut}}{2}}^{\omega+\frac{\omega_{cut}}{2}} g^2(\tilde{\omega})d\tilde{\omega} \approx g^2(\omega)f_{cut}.\tag{5.10}$$

Subsequently, after changing the integration limits in Eq. (5.8)

$$SNR = \frac{\dfrac{1}{2\pi}\displaystyle\int_{\omega-\frac{\omega_{cut}}{2}}^{\omega+\frac{\omega_{cut}}{2}} g^2(\omega)s^2(\omega)d\omega}{\dfrac{1}{2\pi}\displaystyle\int_{\omega-\frac{\omega_{cut}}{2}}^{\omega+\frac{\omega_{cut}}{2}}\left(g^2(\omega)\dfrac{4k_BT}{\omega_0Qk}+D_{ds}^z\right)d\omega}$$

converts to

$$SNR(\omega) \approx \frac{P_s}{P_{ds}^z}\frac{g^2(\omega)}{\left(1+rg^2(\omega)\right)}\cdot\left(\frac{\Delta f_B}{f_{cut}}\right),\tag{5.11}$$

where

$$r = 4\frac{k_BT/k}{Q\omega_0 D_{ds}^z}\tag{5.12}$$

is the ratio of spectral densities of the thermal excitation noise $\dfrac{2}{k}\psi$ to the detection system

white noise D_{ds}^z. The term $\dfrac{g^2(\omega)}{\left(1+rg^2(\omega)\right)}$ is responsible for the SHO amplification and the

term $\left(\dfrac{\Delta f_B}{f_{cut}}\right)$ is responsible for the lock-in amplification. At the resonance

$$SNR(g(\omega_0) = Q) = \frac{P_s}{P_{ds}^z} \frac{Q^2}{\left(1 + rQ^2\right)} \cdot \left(\frac{\Delta f_B}{f_{cut}}\right) \tag{5.13}$$

and off the resonance at $g(\omega) = 1$

$$SNR(g(\omega) = 1) = \frac{P_s}{P_{ds}^z} \frac{1}{\left(1 + r\right)} \cdot \left(\frac{\Delta f_B}{f_{cut}}\right). \tag{5.14}$$

Now, consider the ratio of SNRs at the resonance $(g(\omega_0) = Q)$ and off the resonance $(g(\omega) = 1)$:

$$\frac{SNR(g(\omega_0) = Q)}{SNR(g(\omega) = 1)} = \frac{\left(1 + r\right)}{\left(\dfrac{1}{Q^2} + r\right)}. \tag{5.15}$$

If $Q^2 >> \dfrac{1}{r}$, then $\dfrac{SNR(Q)}{SNR(1)} \approx \dfrac{1}{r} + 1$, i.e. at high Q, the effect of the resonance amplification is defined by r.

If $Q^2 << \dfrac{1}{r}$ then $\dfrac{SNR(Q)}{SNR(1)} \approx Q^2$, i.e. at low $r << 1$, the effect of the resonance amplification is defined by Q^2.

Figure 5.4 (a, c) illustrates $\dfrac{SNR(Q)}{SNR(1)}$ at a single frequency as a function of Q and r.

If sensitivity of the SPM detection system (laser and photodetector) is higher or about the thermal excitation spectral density ($r \geq 1$), then the resonance amplification does not significantly improve the signal-to-noise ratio, because the cantilever thermal vibration spectra corresponds to its frequency vibration spectra. [115,117–119] For more effective resonance amplification r should be significantly less than 1 and Eq. 5.12 can be used to select optimal parameters of the cantilever for the resonance measurements.

A typical cantilever for contact measurements has 10-100 kHz resonance frequency and 0.01-1 N/m stiffness. For numerical estimations the commercial Solver Next AFM microscope (NT-MDT) and a Pt/Ir coated cantilever with 0.3 N/m spring constant and 14.5 kHz resonance frequency were used under ambient conditions on a cross-section of LiMn$_2$O$_4$ lithium-ion battery cathode embedded in epoxy resin and rigorously polished. In contact with the sample the cantilever's quality factor $Q = 30$ and the contact resonance frequency $f_0 = 75.4\,\text{kHz}$ (Figure 5.5). The contact spring constant $k^* \cong 8\,\text{N/m}$ was estimated as a ratio of the contact and the non-contact resonance frequencies and is 27 times higher than the non-contact spring constant. This is in agreement with typical ratios of contact and non-contact cantilever spring constants. [120] However, the thermal noise level (mean square cantilever displacement) in contact remains almost the same, while a decrease by the k^*/k factor was expected. It is due to additional noise originated from the
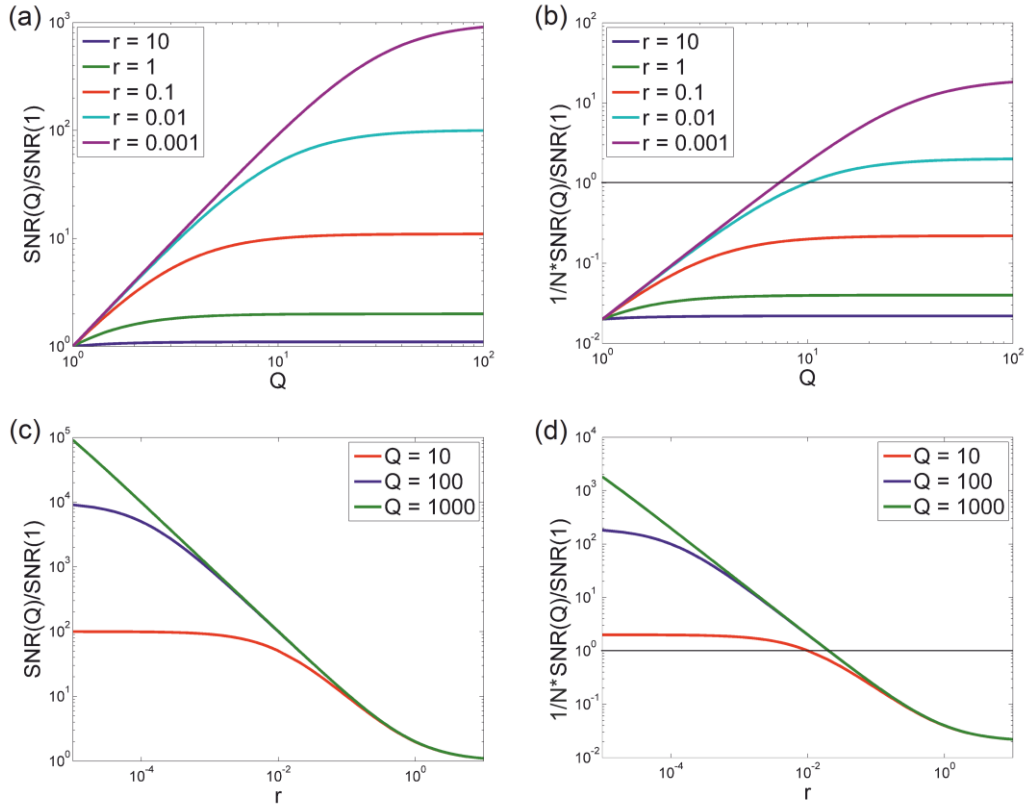
Figure 5.4. Ratio of SNR with resonance amplification (SNR(Q)) to SNR without resonance amplification (SNR(1)) as functions of quality factor Q and r. Figures (a) and (c) illustrates the single frequency case while figures (b) and (d) illustrates the BE case for 50 points in frequency domain. In the BE case (SNR(Q)/SNR(1))/N at one frequency point (bin) can be less than 1 a certain values of *Q* and *r*. (Reproduced from Ref. [114])

change of the cantilever boundary conditions in contact, which are not equal to the ideally fixed beam cantilever. [121]

For these parameters and for $D_{ds}^z = 0.1 \cdot pm^2/Hz$ (taken from the microscope specification) we calculate r=0.014 and $\dfrac{SNR(Q)}{SNR(1)} = 56$ (corresponding ratio of amplitudes is

$\sqrt{\dfrac{SNR(Q)}{SNR(1)}} = 7.5$). In this case, the resonance amplification is 56 instead of maximum

possible $Q^2 = 900$ for the high level of the detection system noise.

Time delay at the resonance $\tau_{SHO} = \dfrac{Q}{2\pi f_0} = 63\mu s$ is still lower than the time of the

signal averaging of the lock-in amplifier $\tau_{low-pass} = \dfrac{1}{2\pi f_{cut}} = 300 \div 3000\,\mu s$ (condition

$\omega_{cut} = 2\pi f_{cut} << \dfrac{\omega_0}{Q}$ for Eq. 5.10), therefore the resonance amplification can improve the
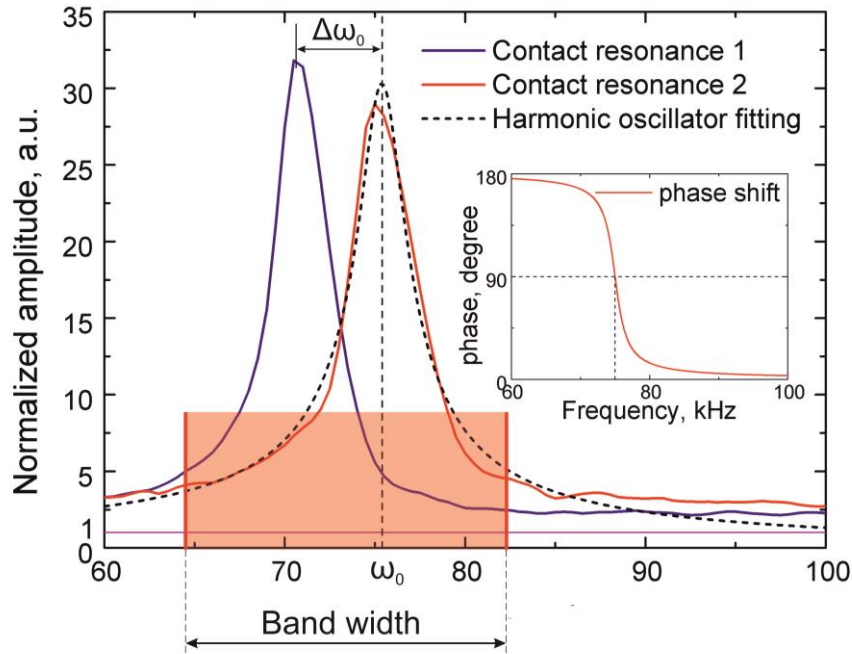
Figure 5.5. Observed resonance frequency shift $\Delta\omega_0$ during scanning. Band width is the schematic frequency range of the BE band needed to track the resonance shift. (Reproduced from Ref. [114])

SNR without the significant additional time delay. However, a shift of the resonance frequency due to the topography crosstalk results in a significant error in the amplitude response in case of the single frequency measurements (Figures 5.1 and 5.5). [112,122] For this reason, the BE or DART techniques are used to avoid the resonance frequency shift error.

Multi-frequency

To analyze SNR for the BE method we should consider a more complex excitation signal. Analytical expressions $x(t)$ of the BE excitation signal in the time domain for continuous spectrum are SINC $\dfrac{\Delta\omega_{BE}}{2\pi}\mathrm{sinc}(\dfrac{\Delta\omega_{BE}}{2}\cdot t)\cdot\exp\left(i\dfrac{(\omega_U+\omega_L)}{2}t\right)$ or CHIRP $V_0\sin(\varphi\cdot t^2)$ single pulses. Since the lock-in processing method operates with a discrete type of a signal spectrum, in practical applications a periodic excitation signal (group of Sinc or Chirp pulses) with the time period $\tilde{T}=\dfrac{N}{\Delta\omega_{BE}}$ (Figure 5.2 (c)) can be used. According to the convolution theorem, such sequence gives a discrete spectrum consisting of $N\div N+1$ bins in the bandwidth $\Delta\omega_{BE}=\omega_U-\omega_L$. The analytical expression of the periodic BE excitation signal can be found as a sum of $N+1$ harmonics $\exp(i\omega_j t)$ with

$$\omega_j = \omega_L + \frac{\Delta\omega_{BE}}{N} \cdot j \text{ and } j = 1, 2, .., N:$$

$$x(t) = \sum_{k=0}^{N} \exp(i(\omega_L + \frac{\Delta\omega_{BE}}{N} \cdot j)t) = \frac{\sin(\frac{N+1}{2N}\Delta\omega_{BE}t)}{\sin(\frac{\Delta\omega_{BE}}{2N}t)} \cdot \exp(i\frac{(\omega_U + \omega_L)}{2}t) , \qquad (5.16)$$

where $\exp\left(i\frac{(\omega_U + \omega_L)}{2}t\right)$ is the carrier signal with the frequency $\frac{\omega_U + \omega_L}{2}$, and

$\dfrac{\sin(\frac{N+1}{2N}\Delta\omega_{BE} \cdot t)}{\sin(\frac{\Delta\omega_{BE}}{2N}t)}$ is the modulation signal with the modulation frequency

$\frac{1}{2}(1 + \frac{1}{N})\Delta\omega_{BE}$ and pulse frequency $\frac{\Delta\omega_{BE}}{N} = \frac{2\pi}{\tilde{T}}$. Here $\tilde{T}$ is the pulse period with 0 and

π alternating phase content following the period $2\tilde{T}$.

Such sequences of the pulses can be characterized by an average power P over the time period $\tilde{T}$

$$P = \frac{1}{\tilde{T}} \int_{-\frac{\tilde{T}}{2}}^{+\frac{\tilde{T}}{2}} |x(t)|^2 dt . \qquad (5.17)$$

According to Parseval's theorem, the average power can be expressed as:

$$P = \frac{1}{\tilde{T}_{BE}} \int_{-\infty}^{+\infty} |x(t)|^2 dt = \frac{1}{\tilde{T}_{BE}} \int_{-\infty}^{+\infty} |X(f)|^2 df , \qquad (5.18)$$

where $\tilde{T}_{BE}$ is the time period of the signal $x(t)$. The average power of the signal can be written as an integral (sum) of the power spectral densities $P(f) = \dfrac{|X(f)|^2}{\tilde{T}_{BE}}$:

$$P = \frac{1}{\tilde{T}_{BE}} \int_{-\infty}^{+\infty} |X(f)|^2 df = \int_{-\infty}^{+\infty} P(f)df . \qquad (5.19)$$

For the spectral density $P(f)$ of the exciting signal with the discrete spectrum including N equal bins, the average power P is equally distributed between each P_i components of the spectrum:

$$P_i = \frac{P}{N} . \qquad (5.20)$$

According to Eq. (5.11), the lock-in amplification is expressed by the relation $\left(\dfrac{\Delta f_B}{f_{cut}}\right)$, where $f_{cut} = \dfrac{1}{2\pi\tau}$ is the cutoff frequency and τ is the time constant limiting the minimum time of measurement. Then SNR improvement after the lock-in amplification is

$$SNR \sim \Delta f_B \cdot \tau, \tag{5.21}$$

i.e. it is proportional to the time of measurement of the system τ. Based on Eq. (5.11), (5.20) and (5.21), the *SNR* at a single frequency point (bin) after the lock-in amplification for different methods such as lock-in sweep/fast tune, band excitation, and single frequency signal processing can be expressed as a ratio of the measurement time (τ) for a number of points in the frequency domain to the number of these bins (*N*) in the frequency domain at the same power P of the driving signal:

$$SNR \sim \frac{time\ of\ measurement}{number\ of\ points\ in\ frequency\ domain} = \frac{\tau}{N}. \tag{5.22}$$

Because of simultaneous measurement of a number of bins in the frequency domain, the signal energy (and the average signal power P) is redistributed between the bins in the frequency band range, and, therefore, the signal-to-noise ratio for a single bin in BE is apparently lower than in the case of the single frequency resonance amplification. In this regard, the DART technique which can operate at the resonance and use only two frequencies should be more effective. [113] However, the method is sensitive to the shape symmetry of the resonance curve and phase stability during quality factor measurements. From the point of view of the average power distribution between frequency points, the fast tuning technique [123] is similar to the described BE method.

Additional resonance amplification results in *SNR* improved by a factor $\dfrac{Q^2}{\left(1 + rQ^2\right)}$ (see Eq. 5.13).

FWHM of the resonance peak of the example cantilever is $\dfrac{f_0}{Q} = 2$–2.5 kHz. To trace the 5 kHz resonance shift (observed on the $LiMn_2O_4$ for the given cantilever – Figure 5.5) in the case of BE the frequency range must be extended at least up to 10 kHz. This needs minimum 10–20 points in the frequency domain (2 points per FWHM). When the tip-surface interactions are non-linear and cannot be described by the SHO model, typical number can be 50–100 points. According to Eq. (5.22), the SNR decrease for a single frequency point is proportional to a number of points in the frequency domain, i.e. 50–100 times that eliminates amplification at the resonance, i.e. 1.1–0.6 instead of 56 for the same measurement time and driving voltage at a single frequency.

Figures 5.4 (b) and (d) illustrate $\dfrac{1}{N}\dfrac{SNR(Q)}{SNR(1)}$ for BE as a function of *Q* and *r* for 50 points in the frequency domain. Under ambient conditions on stiff surface (for example, quartz), typical $Q\sim10^2$ and $r\leq10^{-4}$ that allow efficient resonance amplification using BE. However, in case of soft samples, soft cantilevers, or liquid environment [124] *r* could exceed 0.1 and $\dfrac{1}{N}\dfrac{SNR(Q)}{SNR(1)}$ will be less than 1, i.e. operating at resonance can attenuate the measured response for the multi-frequency detection. Therefore, it is particularly important that the cantilever is chosen according to sample's properties and experimental setup in the

case of multi-frequency detection. Equations (5.12), (5.15) and (5.22) can be used as a guide for choosing correct parameters of the cantilever for the ESM measurements if the noise in the system is known.

If the lock-in detection using the same reference signal with the same phase content for N spectral components of the expected response signal, the spectral amplitudes after the demodulator will be shifted to zero frequency and after summing up can be filtered by a low-pass filter. In this case, we have a coherent sum (in one phase) of N signal amplitudes and a sum of N incoherent (random phase) amplitudes of the noise signal. Incoherent sum of noise amplitudes can be expressed as a sum of noise powers. Such synchronous detection in the BE mode can improve SNR of the response signal.

Indeed, the power presentation of the response signal with N spectral components is $s^2(\omega) = 2\pi \dfrac{P_s}{N} \cdot \sum_{i=1}^{N} \delta(\omega - \omega_i)$, and the amplitude presentation is

$$s(\omega) = 2\pi \sqrt{\frac{P_s}{N}} \cdot \sum_{i=1}^{N} \delta(\omega - \omega_i) , \qquad (5.23)$$

Phase sensitive lock-in detection results in summing up of signal amplitudes:

$$\frac{1}{2\pi} \int_{\omega - \frac{\omega_{cut}}{2}}^{\omega + \frac{\omega_{cut}}{2}} g(\omega) s(\omega) d\omega = \int_{\omega - \frac{\omega_{cut}}{2}}^{\omega + \frac{\omega_{cut}}{2}} g(\omega) \sqrt{\frac{P_s}{N}} \cdot \sum_{i=1}^{N} \delta(\omega - \omega_i) d\omega = \sqrt{\frac{P_s}{N}} \cdot \sum_{i=1}^{N} g(\omega_i) ,$$

and sum of noise powers

$$\frac{1}{2\pi} \sum_{i=1}^{N} \int_{\omega_i - \frac{\omega_{cut}}{2}}^{\omega_i + \frac{\omega_{cut}}{2}} \left(g^2(\omega) D_{th}^z + D_{ds}^z \right) d\omega = \left(D_{th}^z \sum_{i=1}^{n} g^2(\omega_i) + N D_{ds}^z \right) f_{cut} .$$

Then $SNR = \dfrac{P_{signal}}{P_{noise}}$ can be estimated in a similar manner as it was made in Eq. (5.8):

$$SNR = \frac{\left(\dfrac{1}{2\pi} \displaystyle\int_{\omega - \frac{\omega_{cut}}{2}}^{\omega + \frac{\omega_{cut}}{2}} g(\omega) s(\omega) d\omega \right)^2}{\dfrac{1}{2\pi} \displaystyle\sum_{i=1}^{N} \int_{\omega_i - \frac{\omega_{cut}}{2}}^{\omega_i + \frac{\omega_{cut}}{2}} g^2(\omega) D_{tot}^z d\omega} = \frac{P_s}{P_{ds}} \frac{\left(\displaystyle\sum_{i=1}^{N} g(\omega_i) \right)^2}{N \left(r \displaystyle\sum_{i=1}^{N} g^2(\omega_i) + N \right)} \left(\frac{\Delta f_B}{f_{cut}} \right) , \qquad (5.24)$$

where $r = 4 \dfrac{k_B T / k}{Q \omega_0 D_{ds}^z}$ is the ratio of the spectral densities of the thermal excitation noise $\dfrac{2}{k} \psi$ to the detection system white noise D_{ds}^z. The sums $\displaystyle\sum_{i=1}^{N} g(\omega_i)$ and $\displaystyle\sum_{i=1}^{N} g^2(\omega_i)$ for

$N \gg 1$ can be estimated as integrals $\dfrac{N}{\Delta\omega_{BE}} \displaystyle\int_{\omega_0-\frac{\Delta\omega_{BE}}{2}}^{\omega_0+\frac{\Delta\omega_{BE}}{2}} g(\omega)d\omega$ and $\dfrac{N}{\Delta\omega_{BE}} \displaystyle\int_{\omega_0-\frac{\Delta\omega_{BE}}{2}}^{\omega_0+\frac{\Delta\omega_{BE}}{2}} g^2(\omega)d\omega$ with the

bandwidth $\Delta\omega_{BE} = \omega_U - \omega_L$. To estimate these integrals near the resonance we approximated the frequency response function $g^2(\omega)$ by an exponential distribution (Figure 5.6):

$$g^2(\omega) \approx Q^2 \exp\left(\frac{-|\omega-\omega_0|}{\omega_0} \frac{4Q}{\pi} \right), \tag{5.25}$$

Then

$$\sum_{i=1}^{N} g(\omega_i) \approx \frac{N}{\Delta\omega_{BE}} \int_{\omega_0-\frac{\Delta\omega_{BE}}{2}}^{\omega_0+\frac{\Delta\omega_{BE}}{2}} g(\omega)d\omega \approx \frac{N}{\Delta\omega_{BE}} \pi\omega_0 \left(1 - \exp\left(-\frac{\Delta\omega_{BE}}{\omega_0} \frac{Q}{\pi} \right) \right)$$

and

$$\sum_{i=1}^{N} g^2(\omega_i) \approx \frac{N}{\Delta\omega_{BE}} \int_{\omega_0-\frac{\Delta\omega_{BE}}{2}}^{\omega_0+\frac{\Delta\omega_{BE}}{2}} g^2(\omega)d\omega \approx \frac{N}{\Delta\omega_{BE}} \frac{\pi}{2} Q\omega_0 \left(1 - \exp\left(-\frac{\Delta\omega_{BE}}{\omega_0} \frac{2Q}{\pi} \right) \right).$$

Thus, for the bandwidth $\Delta\omega_{BE} = \tilde{\eta}\dfrac{\omega_0}{Q}$ of the excitation signal symmetrically extended to both sides from the resonance, where $\tilde{\eta} \geq 0$, Eq. (5.24) takes the form:
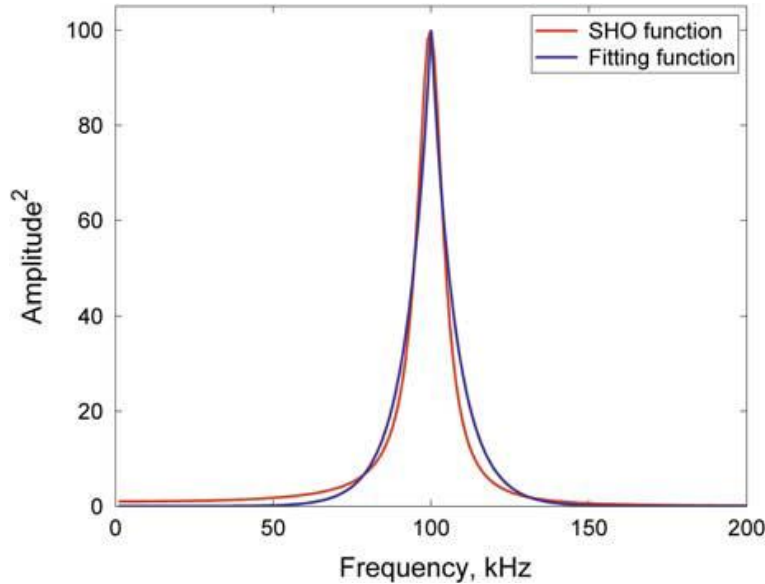
Figure 5.6. Fitting of the frequency response function of SHO by exponential distribution. (Reproduced from Ref. [114])

$$SNR_{\Delta\omega_{BE}} = \frac{P_s}{P_{ds}} \frac{\left(\dfrac{N}{\Delta\omega_{BE}}\pi\omega_0\left(1-\exp\left(-\dfrac{\Delta\omega_{BE}}{\omega_0}\dfrac{Q}{\pi}\right)\right)\right)^2}{N\left(r\dfrac{N}{\Delta\omega_{BE}}\dfrac{\pi}{2}Q\omega_0\left(1-\exp\left(-\dfrac{\Delta\omega_{BE}}{\omega_0}\dfrac{2Q}{\pi}\right)\right)+N\right)}\left(\frac{\Delta f_B}{f_{cut}}\right) =$$

$$= \frac{P_s}{P_{ds}} \frac{\left(Q\dfrac{\pi}{\tilde{\eta}}\left(1-\exp\left(-\dfrac{\tilde{\eta}}{\pi}\right)\right)\right)^2}{rQ^2\dfrac{\pi}{2\tilde{\eta}}\left(1-\exp\left(-\dfrac{2\tilde{\eta}}{\pi}\right)\right)+1}\left(\frac{\Delta f_B}{f_{cut}}\right) =$$

$$= \frac{P_s}{P_{ds}} \frac{\left(Q\dfrac{\pi}{\tilde{\eta}}\left(1-\exp\left(-\dfrac{\tilde{\eta}}{\pi}\right)\right)\right)^2}{\left(r\dfrac{\tilde{\eta}}{2\pi}\coth(\dfrac{\tilde{\eta}}{2\pi})\right)\left(Q\dfrac{\pi}{\tilde{\eta}}\left(1-\exp\left(-\dfrac{\tilde{\eta}}{\pi}\right)\right)\right)^2+1}\left(\frac{\Delta f_B}{f_{cut}}\right)$$

Denote $\tilde{Q} = Q\dfrac{\pi}{\tilde{\eta}}\left(1-\exp\left(-\dfrac{\tilde{\eta}}{\pi}\right)\right)$ and $\tilde{r} = r\dfrac{\tilde{\eta}}{2\pi}\coth(\dfrac{\tilde{\eta}}{2\pi})$, $\tilde{Q} \leq Q$ and $\tilde{r} \geq r$. Then

$$SNR_{\Delta\omega_{BE}} = \frac{P_s}{P_{ds}} \frac{\tilde{Q}^2}{\tilde{r}\tilde{Q}^2+1}\left(\frac{\Delta f_B}{f_{cut}}\right), \tag{5.26}$$

The relation for $\dfrac{SNR_{\Delta\omega_{BE}}}{SNR(1)}$ at different $\tilde{\eta}$ is shown in Figure 5.7 (b). Increase of the bandwidth $\Delta\omega_{BE}$ with respect to the FWHM of the resonance peak $\dfrac{\omega_0}{Q}$ reduces $\tilde{Q}$ and increases $\tilde{r}$ resulting in SNR reduction.

In the limiting case when $\tilde{\eta} \to 0$ we have $\tilde{Q} \to Q$, $\tilde{r} \to r$ and

$SNR_{\eta\to0} = \dfrac{P_s}{P_{ds}} \dfrac{Q^2}{rQ^2+1}\left(\dfrac{\Delta f_B}{f_{cut}}\right)$ is equal to the *SNR* for the single frequency resonance amplification (Eq. 5.13).

In the case when $2\pi < \tilde{\eta} < 2Q$ ($\dfrac{2\pi\omega_0}{Q} < \Delta\omega_{BE} < 2\omega_0$) SNR can be approached as

$$SNR_{2\omega_0>\Delta\omega_{BE}>\frac{2\pi\omega_0}{Q}}(\Delta\omega_{BE}) = \frac{P_s}{P_{ds}} \frac{\left(\dfrac{\pi\omega_0}{\Delta\omega_{BE}}\right)^2}{\left(r\dfrac{Q\Delta\omega_{BE}}{2\pi\omega_0}\right)\left(\dfrac{\pi\omega_0}{\Delta\omega_{BE}}\right)^2+1}\left(\frac{\Delta f_B}{f_{cut}}\right). \tag{5.27}$$
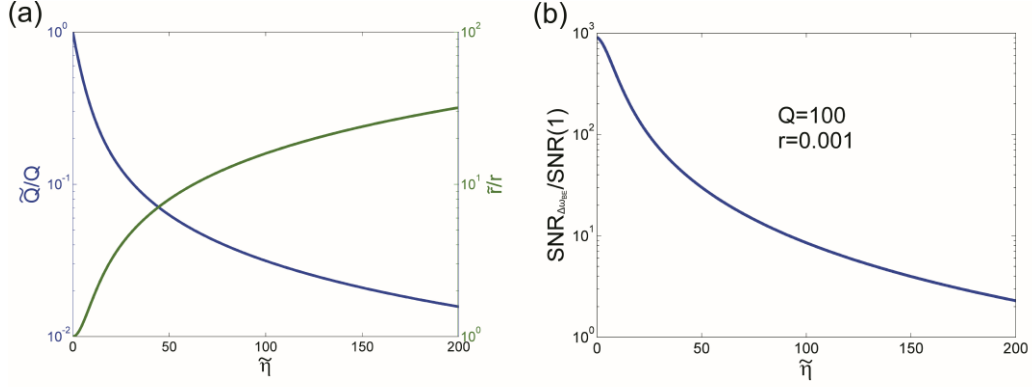
Figure 5.7. $\tilde{Q}$, $\dfrac{SNR_{\Delta\omega_{BE}}}{SNR(1)}$ reduction and $\tilde{r}$ increase as a result of $\Delta\omega_{BE}$ bandwidth increase. (a) represents $\tilde{Q}$, $\tilde{r}$ dependences , and (b) $\dfrac{SNR_{\Delta\omega_{BE}}}{SNR(1)}$ as a function of $\tilde{\eta} = Q\dfrac{\Delta\omega_{BE}}{\omega_0}$. (Reproduced from Ref. [114])

Dependences of $\dfrac{\tilde{Q}}{Q}$ and $\dfrac{\tilde{r}}{r}$ on $\tilde{\eta}$ are shown in Figure 5.7 (a). Reduction of $\tilde{Q}$ and increase of $\tilde{r}$ results in the SNR decrease as can be seen from Fig. 5 (b).

The considered synchronous detection can be used if phase of ESM response is frequency independent within the BE frequency range. To make the lock-in detection synchronous (in one phase) for all spectral components we have to know phase characteristics of the resonance in advance, i.e. first we have to make the fitting procedure on the spectral points when SNR is reduced by a number of bins *N* (Eq. 5.22). Fitting (weighted fitting) of the resonance curve is used to extract the resonance parameters *Q* and f_0, and normalized amplitude $\dfrac{A}{Q}$ of the signal (here we consider amplitude *A* as a fitting parameter). Two fitting parameters *Q* and f_0 are enough to calculate the phase of the response signal at the resonance (Eq. 5.3). The described method is more complicated in realization, but provides the best SNR in the BE mode for a measured ESM/PFM amplitude. In this case, the response amplitude will be characterized by better SNR than the amplitude as the fitting parameter *A*, since in the fitting procedure the basic SNR at each frequency point (bin) is reduced by the number of bins (Eq. 5.22).

Optimal number of bins in the BE mode should be minimal to be enough to make correct fitting and extract basic parameters *Q*, and f_0 of the resonance. This requires minimum two bins per $2 \cdot FWHM = 2 \cdot \dfrac{\omega_0}{Q}$ frequency region (as realized in DART technique) and three bins within resonance – minimal number of bins to make unambiguous fitting of the resonance. Depending on the character of a tip-surface interaction, a resonance frequency shift, and a change of a quality factor, the total number

of bins can be increased to tens and hundreds. In the BE mode the fitting is a key procedure which operates with spectral signal components with reduced by *N* SNR.

One of the alternative ways by which ESM/PFM instrument development can be focused is an improvement in the sensitivity of the detection system of AFMs. The optical beam detection (OBD) noise (D_{ds}^{z}) can be significantly reduced. Fukuma et al [125] developed an OBD sensor with a deflection noise density of 17 $\mathrm{fm}/\sqrt{\mathrm{Hz}}$ instead of conventional 100–1000 $\mathrm{fm}/\sqrt{\mathrm{Hz}}$. Up-to-date AFM systems with the improved sensitivity of the detection system have already achieved 25 $\mathrm{fm}/\sqrt{\mathrm{Hz}}$ level of the detection system noise (according to NT-MDT Titanium AFM specification). According to Eq. (5.12), such reduction of D_{ds}^{z} results in ~5-50 times higher r, thus weakening the effect of the resonance amplification on SNR. In case of the mentioned above low noise optical beam detection system [125] and the given cantilever, *r* could be ~0.1 –1. According to the SNR analysis, in the case when the OBD noise is lower or about the thermal cantilever noise the single frequency regime (conventional mode) becomes optimal with the best SNR of a measured signal as compared with the multi-frequency methods.

An example of the ESM imaging using the single-frequency detection is shown in Figure 5.8 for the cross-section of the commercial battery cell with the LiMn$_2$O$_4$ cathode.

The ESM contrast is overlaid on the topography, which shows LiMn$_2$O$_4$ cathode particles embedded in epoxy resin next to the Al current collector. Decreased vertical sensitivity due to the off-resonance detection is compensated by the elevated ac-excitation
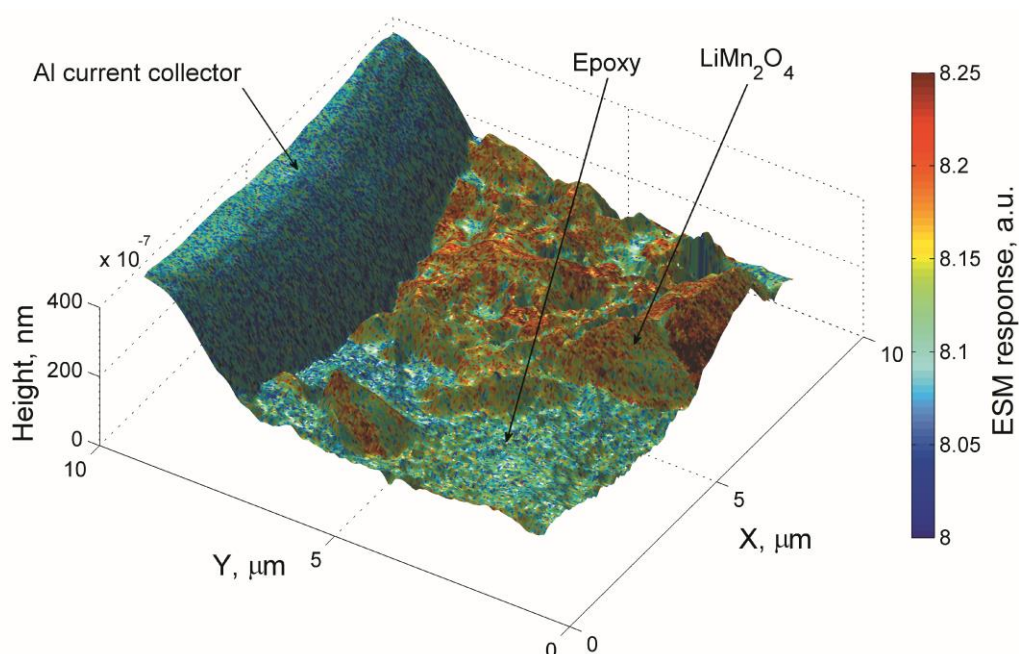
Figure 5.8. ESM image overlaid on the topography of the LiMn$_2$O$_4$ cathode. ESM response is on the LiMn$_2$O$_4$ active particles. Noise signal is on the epoxy and the Al current collector. (Reproduced from Ref. [114])

voltage – 5 V – which did not cause any surface damage. The signal-to-noise ratio in this case was 2 to 4 times lower than that foreseen for the resonance bin in the BE method. Nevertheless, the robust ESM contrast is observed thus allowing nanoscale measurements of Li^+ mobility in lithium-battery electrode materials.

Conclusions

The conventional single-frequency method and the multi-frequency methods for measuring surface displacements were analyzed and compared. Signal-to-noise ratio was calculated taking into account different sources of noise in modern AFM systems. It was shown that the resonance amplification at a single frequency depends on the ratio of the detection system noise to the thermal excitation white noise and can be lower than that predicted by the SHO theory. In case of the multi-frequency detection (BE) the resonance amplification can be additionally attenuated due to distribution of the driving power over a number of points in the frequency domain. The analysis allowed establishing criteria for a cantilever and an experimental setup for the most sensitive detection of surface displacements via a lock-in amplifier. Example of the single-frequency detection ESM imaging was given for the cross-section of the commercial Li-battery According to the presented SNR analysis, the improvement of the sensitivity of the AFM optical detection system is crucial for the performance of ESM (PFM) methods which can be significantly improved in different (multi-frequency and single frequency) regimes.

Chapter 6

Li transport properties in LiMn$_2$O$_4$

A novel method called Electrochemical Strain Microscopy is able to probe transport properties of ion conducting materials at the scale down to a few nm, allowing better understanding of their functionality and degradation mechanisms. Up to now it has been implemented only in the multi-frequency Band Excitation [112] and DART [113] modes on a number of lithium and oxygen conducting materials, [101,126–128] but never on commercial samples and after prolonged cycling at high C-rate.

In the previous Chapter we showed that the single frequency detection possess sufficient sensitivity to detect the ESM response. This Chapter summarizes ESM results obtained on LiMn$_2$O$_4$ cathodes at different SOH and SOC in the single frequency out of resonance mode. The results revealed a difference in voltage spectroscopy electrochemical loops between the fresh and the fatigued samples. Time spectroscopy data were used to quantitatively estimate diffusion coefficients of Li in the samples. These data were analyzed in the framework of existing degradation mechanisms. Finally, an alternative mechanism of the ESM response origin from ionic polarization rather than from Vegard's expansion was proposed and used in a finite element model.

6.1 Defining the measurement limits

In Chapter 3 we stated that the ESM response represents the combined contribution of several factors and cannot be directly used to distinguish among different mechanisms involved in signal formation. For this reason, voltage and time spectroscopies are used to isolate specific contributions to the signal. The aim of the ESM spectroscopies is to study electrochemical system dynamics, i.e. bringing it from the initial stable state into an unstable one and observing its relaxation to the initial state. Electric potential applied between a tip and a sample changes local Li concentration below the tip. Exact concentration change depends on the duration and amplitude of the applied dc pulse. As it was noted in Chapter 2, Li$_x$Mn$_2$O$_4$ experiences several phase transitions upon lithiation/delithiation. Phase transition can temporarily stabilize the system, preserving its

relaxation as well as changing local properties (diffusion coefficient, conductivity, etc.) Additional perturbation can emerge from induced electrochemical reactions at the tip-sample interphase with formation of stable or metastable products of the reactions. These effects should be avoided. Therefore, before performing actual measurements we will determine a maximum dc voltage that can be applied without phase transitions and irreversible electrochemical reactions. In order to determine these limits, we applied dc pulses and determined where the expected transitions start. Appearance of measurable currents correlated with change of topography was attributed to onset of an electrochemical reaction.

Note that the samples are composites and after cycling different particles could have different Li concentration as was reported by Amanieu et al. [129] Nevertheless, all particles where measurements were done showed similar voltage-current dependences.

Figure 6.1 summarizes the measurement results. Negative voltage applied to the tip produced small but detectable stable current below -5 V presented in Figure 6.1 (a). Positive voltage applied to the tip produced unstable current above +6 V, which was 1-2 orders of magnitude higher than that produced by the negative pulses (Figure 6.1 (b)). These will derive the limits for applied dc voltage in further measurements.
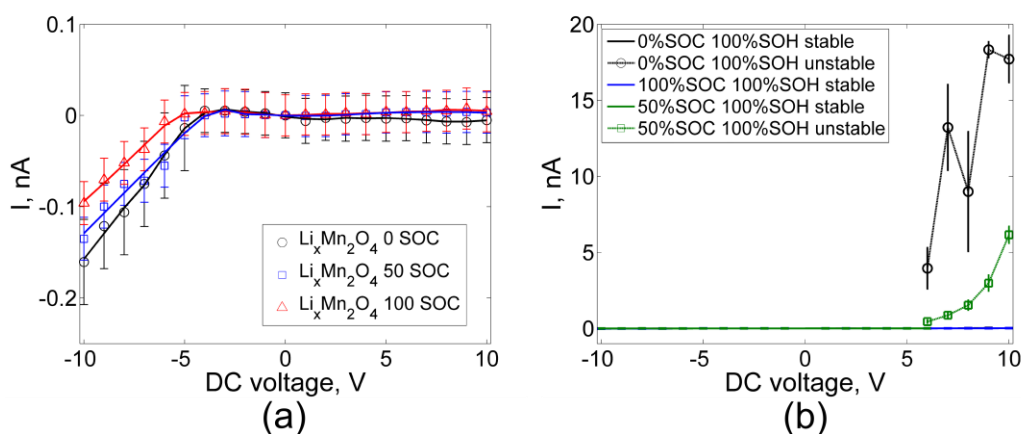
Figure 6.1. Current dependences. Two regimes of current were determined: stable after negative pulses (a) and unstable after positive ones (b).

Note that the small stable current slightly decreased with the increasing state of charge. It corresponds to decrease of Li concentration and amount of electronic current carriers (presumably small polarons). [12]

Figures 6.2 and 6.3 illustrate reversible and irreversible types of surface changes. The reversible change of topography was attributed to the formation of small (200-300 nm in diameter) protrusions on the surface, which relaxed after 15 minutes (Figure 6.2). ESM response after the relaxation returned back to the initial value. Such behavior might be due to a field-induced phase transition. The field induced cubic to tetragonal phase transition during scanning of a $LiMn_2O_4$ sample by a SPM tip under bias was observed by Kuriyama et al. [130] This new phase, being metastable, relaxed back into the spinel.
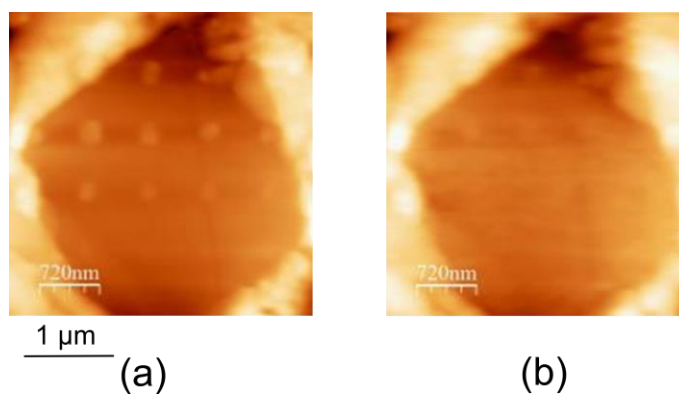
Figure 6.2. Reversible change of topography upon application of dc voltage pulses: (a) protrusions in topography formed by the pulses; (b) topography after 15 minutes, protrusions relaxed.
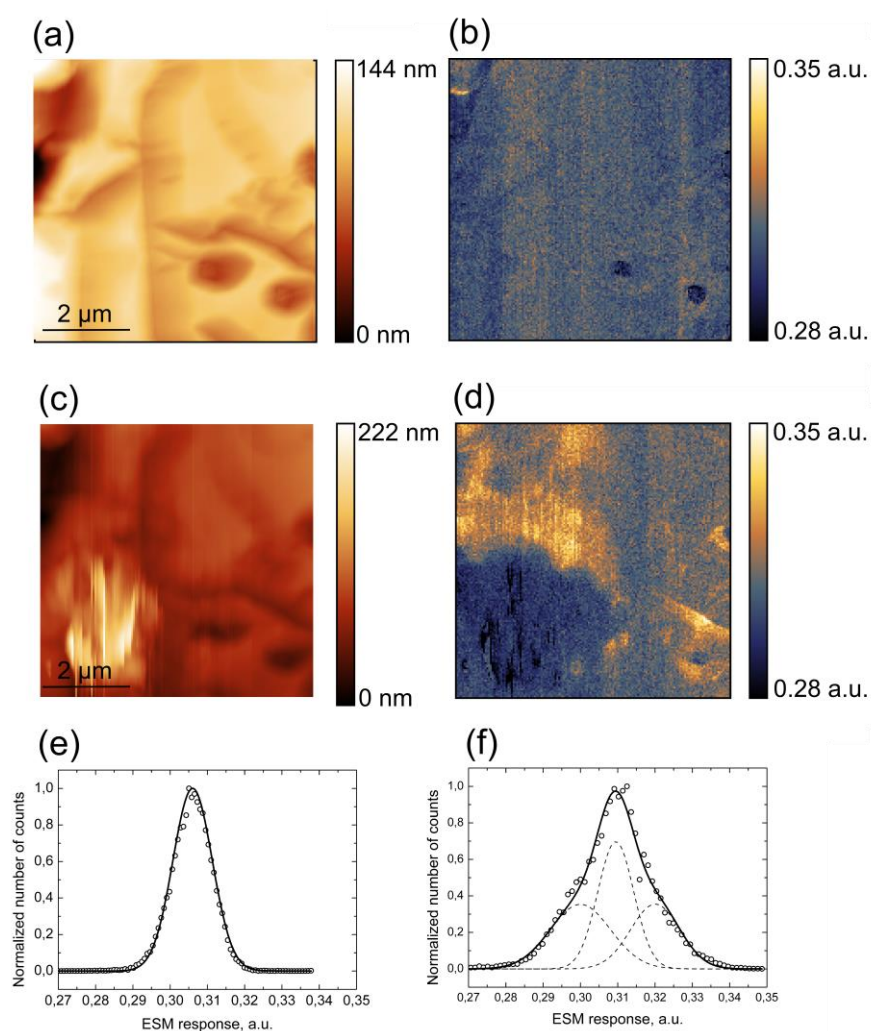
Figure 6.3. Irreversible change of topography and ESM response upon application of dc voltage pulses: (a) and (b) topography and ESM response before the dc pulse; (c) and (d) topography and ESM response after the dc pulse; (e) and (f) ESM histograms before and after the pulse.

The irreversible surface change was attributed to appearance of a ~100 nm high stable particle on the surface (Figure 6.3). The ESM response was suppressed on the particle and increased around it. The increased one was noticeably stronger than the initial response before the damage. It illustrates that the irreversible damage, being created by applying voltage between the tip and the sample on the area of ~30 nm radius, modifies much larger area (up to several μm).

Note, that the actual potential in the material is smaller than the applied one because of the interfacial potential drop. [101]

6.2 Possible non-Vegard contributions

Figure 6.4 shows amplitude hysteresis loops taken on the same 0% SOC 100% SOH LiMn$_2$O$_4$ sample from different places. On the one hand, Figure 6.4 (a) shows the concentration dependent loop. Negative dc voltages applied to the tip attract mobile Li ions to the tip-sample contact and increase the local Li concentration below the tip, thus increasing the ESM response. Positive dc voltages repulse Li ions and reduce the local Li concentration, thus decreasing the ESM response. On the other hand, Figure 6.4 (b) exhibits the butterfly-like shaped asymmetric loop with the higher signal. This kind of loop does not seem to be Li concentration dependent and is not expected in LiMn$_2$O$_4$.

Ideal ESM response is attributed to oscillatory surface displacements caused by the Vegard strain due to local concentration change of lithium ions under the applied ac electric field. However, the lock-in detection system of the microscope can measure another ac-mediated responses contributing to the first harmonic signal $A_{1\omega}$, which were briefly described in Chapter 3 as follows (see Eq. 3.13):
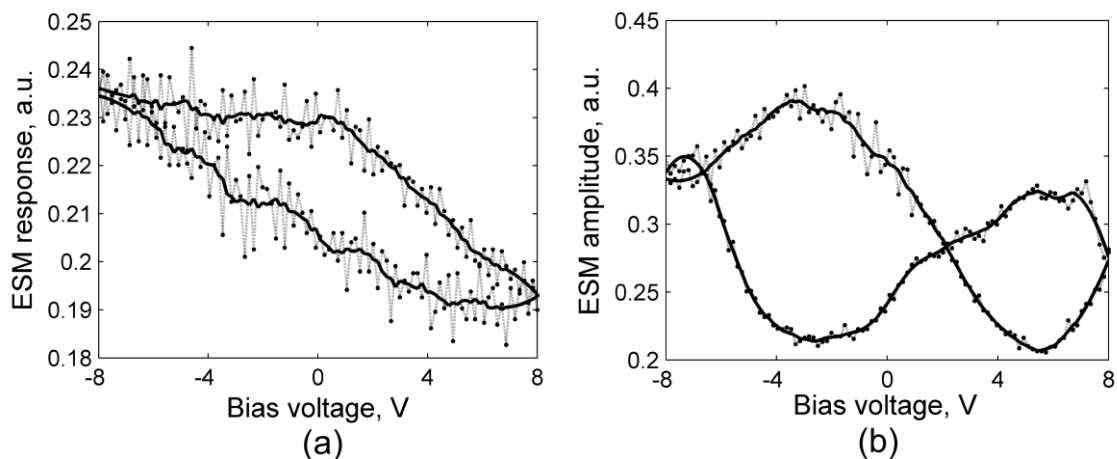
Figure 6.4. Experimental amplitude hysteresis loops measured on LiMn$_2$O$_4$ particles: (a) non-polar loop caused by presumably Vegard's response; (b) complex loop with the additional polar contribution.

$$A_{1\omega} \propto -\frac{(1+\nu)}{\pi} h \left(\left(\beta - \frac{2q}{\varepsilon_0} f_{33} \right) \langle \delta C_i(t) \rangle + \Xi_{33}^C \langle \delta n(t) \rangle + \Xi_{33}^V \langle \delta p(t) \rangle + \frac{\tilde{Q}_{33} k_B T}{2\varepsilon_0} \langle E_3^2 \rangle \right) +$$
$$\frac{1}{\tilde{k}} \frac{\partial C}{\partial z} (V_{dc} + V_C) V_{ac} + d_{33} V_{ac}$$
.

Multiple non-Vegard contributions have to be distinguished in the measured response in order to prevent misinterpretation of results. The best way to do this is to know qualitative and quantitative properties of each contribution.

For $Li_x Mn_2 O_4$ the lattice parameter changes almost linearly from 8.03 Å for λ-MnO_2 to 8.24 Å for $LiMn_2O_4$. Taking into account that the dynamic resolution of ESM is about 10 pm (using a lock-in amplifier), one can detect about 5% of the Li concentration variation in the unit cell (on average).

Flexoelectric and deformation potential contributions for $LiMn_2O_4$ are not known, but typically an order of magnitude smaller than the Vegard contribution. [95]

Electrostatic and electrostriction contributions normally appear as the second harmonic of the driving signal. They can, however, appear as the first harmonic, but only if the dc component of the electric field is present. In the dc off state the dc electric field can be caused by the contact potential difference between the tip and the sample which is normally constant. In this case, the electrostatic and electrostriction contributions do not change the hysteresis loop shape measured in the off-field state. [103] They just shift the whole loop along the ESM response axis causing the offset. However, this is not always true. Sufficiently high voltage applied to the tip in contact with the sample can cause a charge injection. Typical space charge relaxation time (also known as Maxwell-Wagner relaxation) for $LiMn_2O_4$ with the static dielectric permittivity ≈ 10 [131] and electrical conductivity $\sim 10^{-6}$ S/cm [7] does not exceed $\sim 10^{-6}$ sec ($\tau = \frac{\varepsilon_0}{\sigma}$). Nevertheless, if charge traps are present, the injected charge can be stabilized and its relaxation time can significantly exceed 10^{-6} sec. If it is longer than the probing time after the dc voltage pulse, it can contribute to the dc off signal. This phenomenon was demonstrated in perovskite manganite $La_{0.89}Sr_{0.11}MnO_3$. [132]

The response is not limited by the mentioned above general contributions. $LiMn_2O_4$ is a small polaron semiconductor [40] with centrosymmetric cubic crystal structure (centrosymmetric structure rules out the piezoelectric effect). The external electric field applied in ESM experiments between a tip and a counter electrode should induce a dipole moment of the small polarons (as schematically shown in Figure 6.5) and their ordering. [133] Corresponding signal will be detected along with the true ionic ESM response. The dipole moment is proportional to a number of polarons, i.e. it is higher for the higher local Li concentration.

Note, that if the driving frequency ω is below the dipole polarization change frequency, then the response must be detected as the second harmonic of the driving frequency, because the induced dipole reorient (if it can) in the ac field each half period in order to compensate an external electric field. In this case, it will just increase the effective

(a)

(b) $+$ $\leftarrow \text{---} \mathbf{E}_{int}$

$\rightarrow \mathbf{E}_{ext}$

$-$
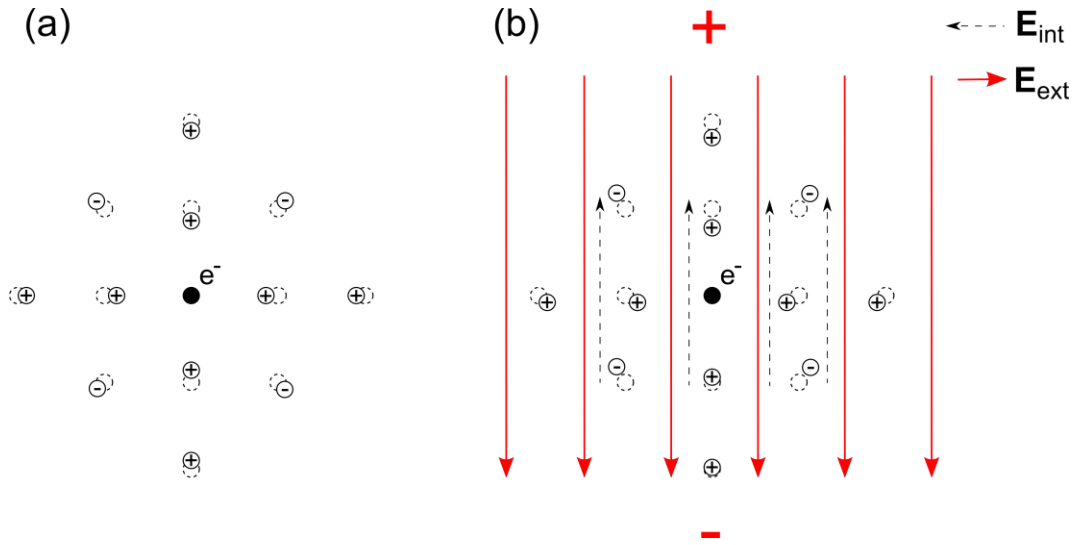
Figure 6.5. (a) Schematic representation of the polaron; (b) dipole moment induced in the polaron by the external electric field.

dielectric permittivity in the second harmonic electrostriction contribution. It can, however, response at the first harmonic if there is a dc component, which is always present due to contact potential difference and charge injection. Physically it means that at a certain dc electric field part of the polaron dipoles are induced and oriented (induced polaron polarization P_{ip}), thus giving a total dipolar moment that respond to the ac at the first harmonic as $2Q_{33}\chi\varepsilon_0 P_{ip}E_{ac}\cos(\omega t + \varphi_0)$. Because the induced polarization P_{ip} is determined by the dc electric field, the final response depends on the dc/ac ratio.

Additionally, static long-range ordering of Jahn-Teller polarons and local charge ordering under the external electric field in manganites can induce lattice distortion that can break the structural inversion symmetry and provoke local ferroelectric-like response. [132, 134, 135, 136] Though it has not been reported in $LiMn_2O_4$ so far, we cannot exclude a possibility of emergence of the ferroelectric-like state (localized in time and space), which is difficult to assess numerically.

This contribution can be more complex when the local Li/Mn ratio below the tip exceeds the first order Jahn-Teller distortion threshold (average Mn^{n+} oxidation state ≤ 3.5) and induces lattice transformation from the cubic to the tetragonal crystal structure. [37] Though the first order Jahn-Teller distortion does not break the inversion symmetry, the structural transformation/electrochemical reaction can manifest itself via a butterfly-like amplitude response and phase switching, which was observed even in silicon at very high values of the applied voltage. [137]

It follows that not all contributions can be quantitatively estimated and subtracted. Fortunately, the qualitative approach still allows distinguishing the presence of non-Vegard contributions. Ferroelectric, electrostatic, electrostriction, and dipole non-Vegard contributions to the first harmonic considered above are polar and, therefore, should possess the characteristic V- of butterfly-like shape of the amplitude hysteresis loop (as in

Figure 6.4 (b)) and 180° phase switching. Alternatively. the concentration controlled ESM amplitude loop should possesses the diamond-like shape (as in Figure 6.4 (a)) and its phase does not switch at 180° due to the non-polar nature of the Vegard strain response, [106] which depends mainly on the Li concentration and the Li diffusion coefficient in the host lattice. Such qualitative approach is sufficient to differentiate polar and non-polar contributions.

6.3 Voltage spectroscopy on $LiMn_2O_4$

6.3.1 Voltage spectroscopy measurements

Kumar et al [101] showed that the ESM loop's shape is controlled by relaxation kinetics and thermodynamics of an electrochemical reaction. The representative results on the cross-section of the 0% SOC 100% SOH $LiMn_2O_4$ sample are shown in Figure 6.6. Here, we measured electrochemical loops for three different times after dc pulses at the same location. Loop opening corresponds to the change of local Li^+ concentration and strain below the tip. The obtained loop shapes are nonpolar and similar to those reported by Balke et al. [138]
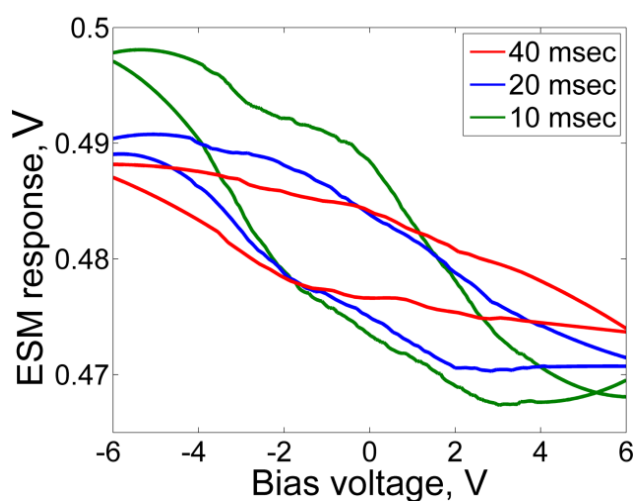
Figure 6.6. Voltage spectroscopy (electrochemical hysteresis loops) for 10, 20, and 40 ms pulse period.

Loops measured over a grid of points on surface can reveal distribution of electrochemical activity (Li^+ mobility/concentration) as a function of position. Figure 6.7 represents mapping of the hysteresis loop opening measured over a grid of points on the fresh (a), (c), (e) and fatigued (b), (d), (f) samples at different states of charge. The loop opening (represented by the color scale) is overlaid with the surface topography. On the epoxy the loops are closed as expected because there are no mobile ions responsible for the ESM signal. On the active particles the loops are open. On the fresh samples loop opening is relatively uniform and does not exceed 0.1 a.u. for this experiment In contrast, loop
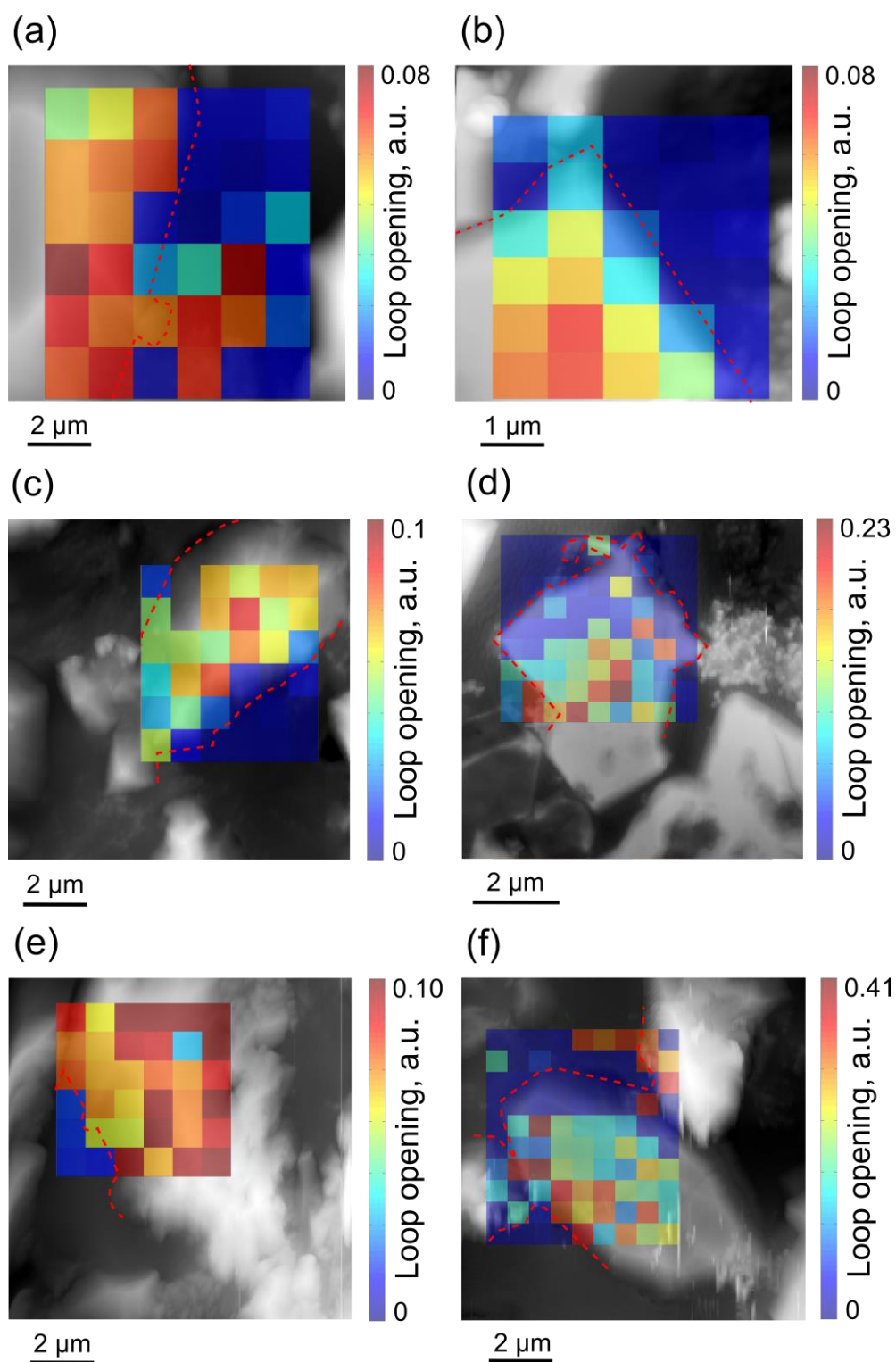
Figure 6.7. ESM loop opening maps on the fresh and fatigued cathodes: (a) 0% SOC, 100% SOH; (b) 0% SOC, 78% SOH; (c) 50% SOC, 100% SOH; (d) 50% SOC, 78% SOH; (e) 100% SOC, 100% SOH; (f) unchargable, 78% SOH. Each loop is average of 3 loops measured consequently at the same point. Dash line traces the particles edges. Topography images are the same as in Figure 6.8.

opening on the fatigued samples is less uniform, indicating less uniform properties determining the measured response. The loop opening irregularity and the amplitude increase with the SOC, i.e. with sample delithiation.

More information can be extracted from the loop's shape. Figure 6.8 compares typical electrochemical hysteresis loops measured on the same fresh (a), (c), (e) and fatigued (b), (d), (f) samples. Loops 1 on all samples were measured on the epoxy that filled porosity in the PVDF binder. They are expectedly closed. Loops 2, 3, and 4 were obtained on different places within $LiMn_2O_4$ particles. They are open, clearly indicating presence of mobile Li^+ ions. The ESM hysteresis loops from the fresh samples are uniformly open over the particle with the response gradually changing with the applied dc voltage (corresponding to change of local Li^+ concentration and strain below the tip). In contrast, stronger variation of the loop opening was observed on the fatigued samples. As compared to the loops from the fresh sample, they possess noticeably different shapes and wider range of amplitudes.

Considering only the Vegard contribution, such increase of the loop opening can be explained by lower Li^+ diffusion coefficient. Taking into account the complex dependence of the Li diffusion coefficient on the Li concentration, [53] the observed change of loop's shape can also indicate wider variation of the Li diffusion coefficient over the dc voltage cycle on the fatigued sample.

What is more interesting, some of the loops (for example, loop 4 in Figure 6.8 (e)) possess the butterfly-like shape with significantly asymmetric shoulders (like those in Figure 6.4 (b)): the negative bias shoulder is higher than the positive bias one. Such behavior indicates the appearance of additional non-Vegard contribution(s). The ratio of the Vegard to the non-Vegard contributions can determine the final shape of the hysteresis loop.

In view of complex nature and multiple sources of the total non-Vegard contribution, it is hard to estimate it numerically. Nevertheless, one hypothesis can be proposed based on previously published results by Proksch [139] and Chen et al [106].

6.3.2 Analysis of the loop's shape

Proksch employed ESM to measure potassium mobility in a soda-lime glass. [139] Until a certain dc voltage, amplitude hysteresis loops were opened only from one side. Upon the dc voltage increase, the loops started to open up from another side, forming a butterfly-like shape. It was attributed to mobile potassium ions. However, the pure Vegard expansion caused by *only one type of mobile ions* cannot explain this phenomenon. Chen et al [106] suggested that such butterfly amplitude loops from the soda-lime glass can be caused by induced dipoles.

Indeed, in dielectric materials strain induced by electric field is

$$u_{ij} = Q_{ijmn} P_m P_n,$$ (6.1)

where Q_{ijmn} are the elements of the fourth rank polarization related electrostriction tensor,
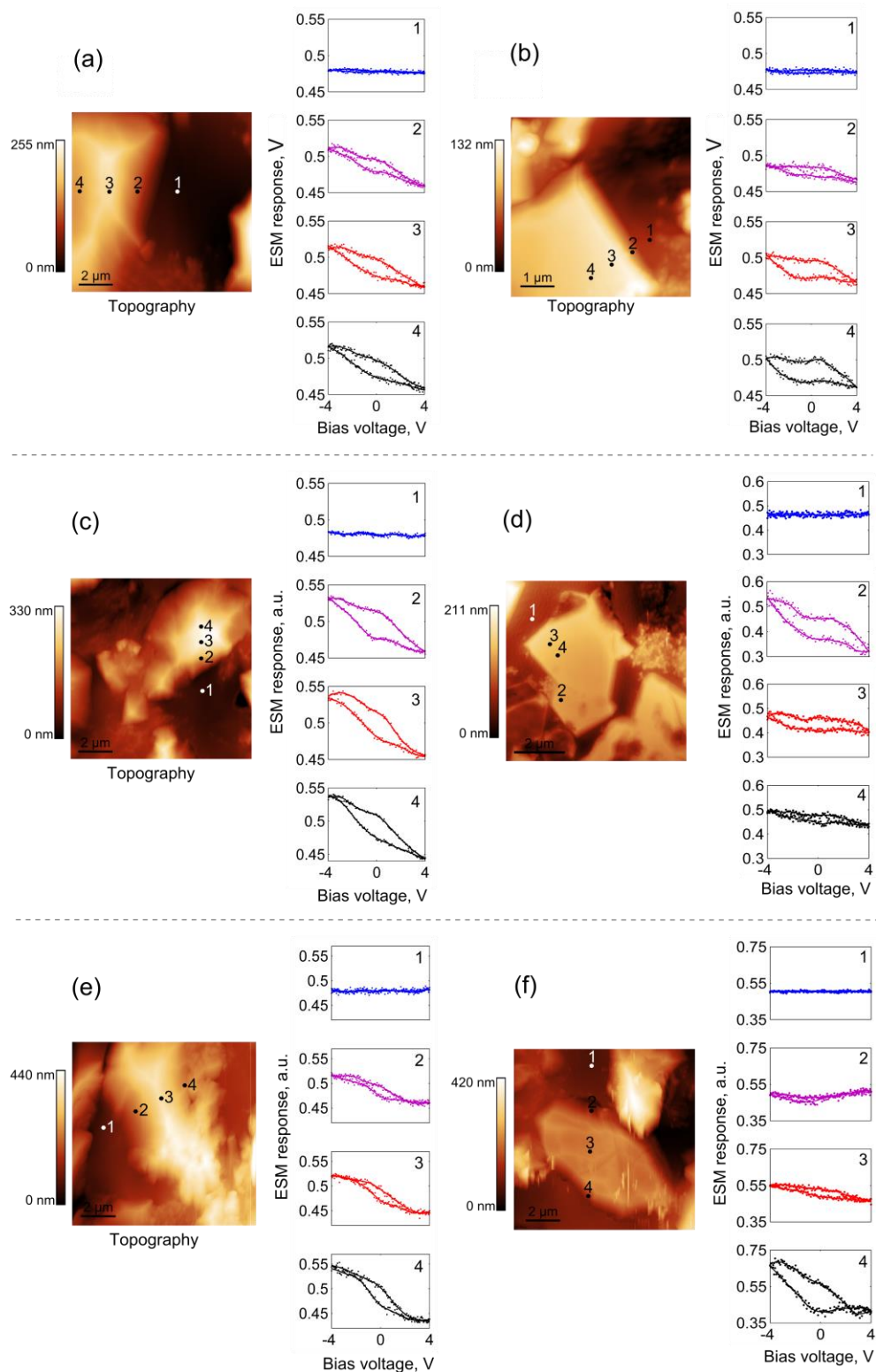
Figure 6.8. ESM loops on the fresh and fatigued cathodes: (a) 0% SOC, 100% SOH; (b) 0% SOC, 78% SOH; (c) 50% SOC, 100% SOH; (d) 50% SOC, 78% SOH; (e) 100% SOC, 100% SOH; (f) unchangeable, 78% SOH. Each loop is average of 3 loops measured consequently at the same point.

P_m and P_n are the components of the polarization vector **P**. [140] Normally, in ESM we measure only deformation normal to the surface, so, for simplicity, we consider only one component of the strain. In this case, the strain expression simplifies as follows:

$$u_{33} = Q_{33}P^2 , \qquad (6.2)$$

where the total polarization $P = P_i + P_{sp}$ with the induced polarization $P_i = \chi\varepsilon_0 E$ and the spontaneous polarization P_{sp}. Then the strain can be expressed as follows:

$$u_{33} = Q_{33}(\chi\varepsilon_0 E + P_{sp})^2 = 2Q_{33}\chi\varepsilon_0 P_{sp}E + Q_{33}P_{sp}^2 + Q_{33}\chi^2\varepsilon_0^2 E^2 . \qquad (6.3)$$

The applied electric field is $E = E_{dc} + E_{ac}\cos(\omega t + \varphi_0)$. Then Eq. (6.3) takes form

$$
\begin{aligned}
u_{33} = &\left(2Q_{33}\chi\varepsilon_0 P_{sp}E_{dc} + Q_{33}P_{sp}^2 + Q_{33}\chi^2\varepsilon_0^2 E_{dc}^2 + \frac{1}{2}Q_{33}\chi^2\varepsilon_0^2 E_{ac}^2 \right) + \\
&+ \left(2Q_{33}\chi\varepsilon_0 P_{sp}E_{ac} + 2Q_{33}\chi^2\varepsilon_0^2 E_{ac}E_{dc} \right)\cos(\omega t + \varphi_0) + \\
&+ \frac{1}{2}Q_{33}\chi^2\varepsilon_0^2 E_{ac}^2 \cos(2\omega t + \varphi_1)
\end{aligned} \qquad (6.4)
$$

The first harmonic response $2Q_{33}\chi\varepsilon_0 P_{sp}E_{ac} + 2Q_{33}\chi^2\varepsilon_0^2 E_{ac}E_{dc}$ includes the spontaneous polarization term $2Q_{33}\chi\varepsilon_0 P_{sp}E_{ac}$ with the polarization coefficient $2Q_{33}\chi\varepsilon_0 P_{sp}$ [140,141] and the electrostrictive term $Q_{33}\chi^2\varepsilon_0^2 E_{ac}E_{dc}$ that appears if the dc component of the electric field $E_{dc} \neq 0$ is present.

As one can see from Eq. (6.4), the response driven by the spontaneous polarization P_{sp} does not require $E_{dc} \neq 0$ and can be sufficiently measured in the off field state. The total response at the first harmonic is not limited by the $2Q_{33}\chi\varepsilon_0 P_{sp}E_{ac}$ contribution. Additional dc-mediated electrosctrictive response $Q_{33}\chi^2\varepsilon_0^2 E_{ac}E_{dc}$ should be present.

Dc component always exists due to the contact potential difference between the tip and the sample. Usually it is not sufficiently large to cause a response big enough to exceed the Vegard response. It can be derived from comparison of the fresh and the fatigued samples, where the contact potential difference between the tip and the sample must be the same. However, on the fresh samples Vegard's response clearly dominates. It means that the contact potential difference dc is not sufficiently large to cause significant electrostrictive signal. Additional source of charge traps or spontaneous polarization must be present in the fatigued samples.

One possible source of the charge traps are point defects introduced into the structure by the 16C-rate cycling. If this statement stands, then the local charge injection, being trapped on the defects, increases the local background dc bias, thus increasing the first harmonic electrostriction contribution $Q_{33}\chi^2\varepsilon_0^2 E_{ac}E_{dc}$ (it can increase the spontaneous polarization contribution as well if $P_{sp} = f(E_{dc})$).

Presence of the non-Vegard contributions in the fatigued samples may indicate spontaneous polarization of unidentified nature.

Under ambient conditions additional bias can appear due to dissociation of the adsorbed water in the applied electric field and injection of the dissociate ions into surface. [142] To avoid unnecessary charge injection, one should conduct experiments under controlled conditions (low humidity, etc.)

6.3.3 Analysis of loop's opening

In view of irregular and complex shape of the loops from the fatigued samples, further analysis was done on the loops from the fresh samples.

Figure 6.9 illustrates average ESM amplitude loops measured on the fresh $LiMn_2O_4$ samples with different Li concentration and on the $LiMn_2O_4$ thin film. The loops exhibit typical concentration dependent shape as described above. The first loop on the left is taken on the epoxy.

The loops open wider with increasing SOC, i.e. with the lower Li concentration. Taking into account that the loop opening represents the amount of mobile Li redistributed by the dc electric field, the difference may origin from two sources: (i) different diffusion coefficients of Li in the host lattice; (ii) saturation of available Li positions within the cubic phase.

(i) Higher diffusion coefficient of Li in the spinel host lattice results in a more complete relaxation of the local Li concentration excess and strain for the same period of time. Consequently, the ESM response, representing the amount of local strain, will show smaller deviation from equilibrium for the higher diffusion coefficient after each dc pulse, thus leading to a more closed loop. Therefore, more closed loops represent higher local diffusion coefficient ceteris paribus. Taking into account that the Li diffusion coefficient in $LiMn_2O_4$ indeed depends on Li concentration, [53] this explanation looks reasonable.
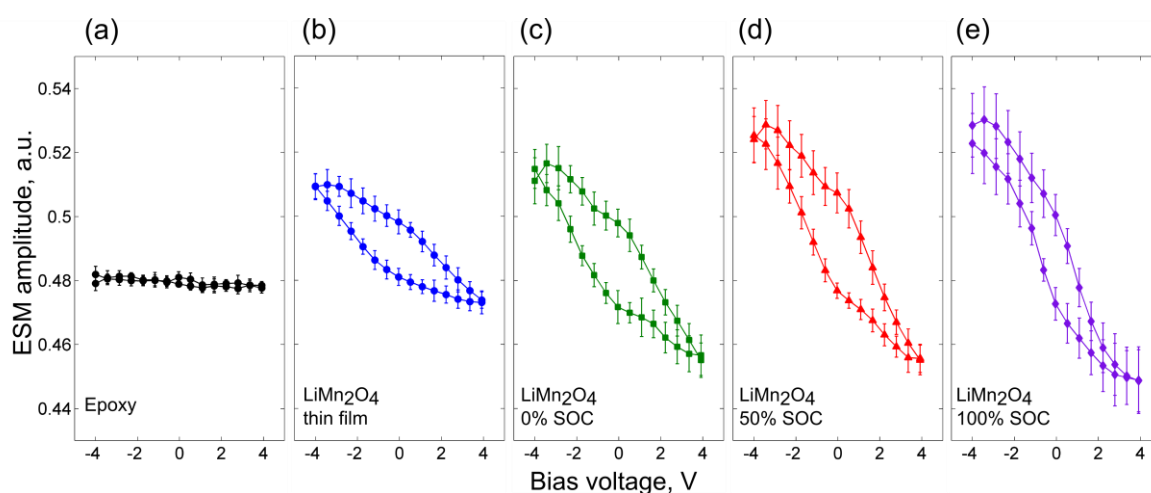
Figure 6.9. ESM loops on the fresh cathodes: (a) epoxy (b) $LiMn_2O_4$ thin film; (c) 0% SOC, 100% SOH; (d) 50% SOC, 100% SOH; (e) 100% SOC, 100% SOH. Each loop (except of the epoxy one) is an average of 75 loops measured over 25 points with 3 loops at each point.

(ii)   Saturation of available Li positions should decreases the loop opening with increasing Li concentration. Li cannot occupy more than $1/8^{th}$ of the 8a octahedral positions within the cubic phase of $LiMn_2O_4$ (otherwise, the structure transforms into the tetragonal phase). As a consequence, ideally when all available 8a positions are occupied, i.e. the stoichiometric spinel is fully lithiated $Li_{x=1}Mn_2O_4$, the ESM Vegard response should be null due to absence of concentration variation (without source and drain of Li^+ ions and with the ideally blocking tip-surface contact interface). Delithiation of the stoichiometric fully lithiated spinel creates vacant 8a positions available for Li and allows local concentration variation below the tip, thus opening the loop. Higher local concentration variation results in wider loop opening. Thus, lower concentration of mobile Li^+ ions within the single spinel phase wider opens the loop, which is the case in Figure 6.9. This stands until a certain degree of delithiation, below which the loop starts to close due to lack of mobile Li.

In principle, both (i) and (ii) mechanisms can act in parallel.

Figure 6.10 illustrates the average loop openings based on two parameters: the min-max loop opening was measured between the minimum and maximum points of the loop; the mean loop opening was measured between the forth and back branches of the loop at 0 V_{dc}. The min-max loop opening increases with the SOC, while the middle loop opening remains constant. The min-max loop opening was explained above by the diffusion and saturation mechanisms. Obviously, the mean loop opening cannot be attributed to the saturation mechanism. It represents a difference between the remaining concentration excess and lack during the bias voltage sweep from plus to minus and vice versa. Apparently, this value is the same for different SOCs. It may thus represent thermodynamics of the system rather than its kinetics. This question is still open and requires detailed theoretical description and computer modeling.

In the end, the ESM loop is a complex type of measurements. Each data point depends on the length of the pulse, the history of the measurement (the accumulation of all the previous pulses in the spectroscopy) and the time lag between the release of the dc pulse and the data point (longer time lags give smaller loops as illustrated in Figure 6.6). Qualitative data with a certain physical meaning cannot be extracted at present. Voltage spectroscopy has the advantage of giving a qualitative overview within seconds of voltage dependences in the ESM signal and the reversibility of the measurement. It can clearly represents spatial variation of the voltage induced local concentration variation and indicate presence of additional non-Vegard contributions. Further development of ESM theory is prerequisite for separation and quantification of multiple data containing in the ESM loop.

Deeper insight into battery functionality with possible quantitative interpretation can be done by the time spectroscopy.
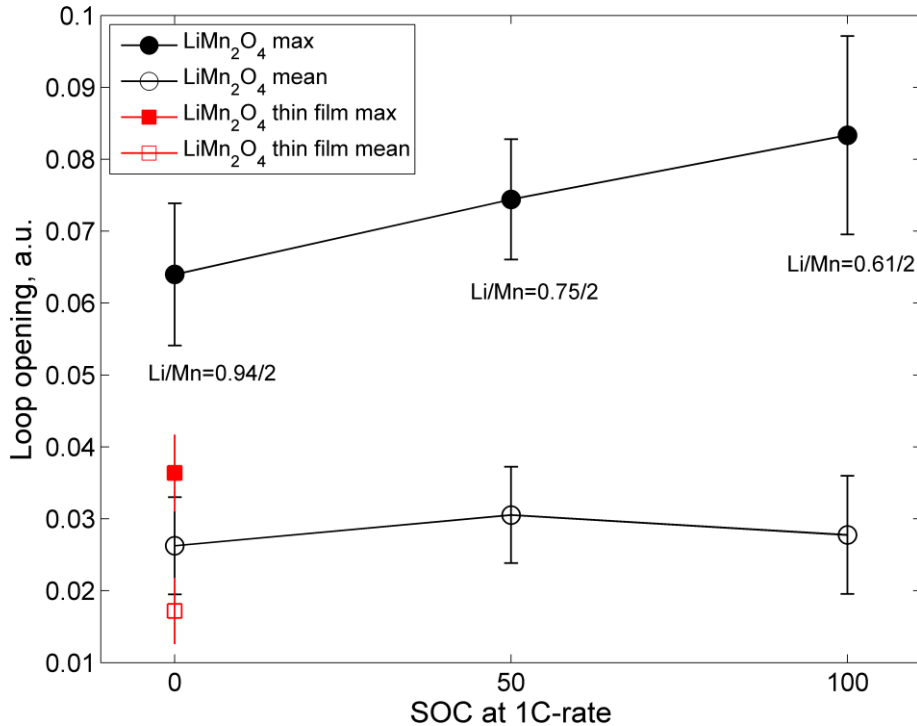
Figure 6.10. Average ESM loop opening as a function of SOC. The top graph is the min-max loop opening, measured between the maximum and minimum points of the loop. The bottom graph is the mean loop opening, measured between the forth and back branches at 0 V_{dc}.

6.4 Time spectroscopy on LiMn$_2$O$_4$

6.4.1 Time spectroscopy measurements

In time spectroscopy, a sequence of dc pulses with the same magnitude and consequently different signs is applied between the tip and the sample's counter electrode, and the ac mediated surface vibrations (ESM response) are typically measured after the dc pulses. Dynamics of the ESM response represents dynamics of the local deformations and presumably reflects the instant change of Li$^+$ concentration and, therefore, serves as a signature of the ionic mobility.

Figure 6.11 illustrates results of time spectroscopy measurements on both fresh and fatigued samples at 0% SOC. Here we measured ESM response not only when the dc bias is off, but also when dc is on to observe both electro-migration and diffusion processes. The same measurements were performed on the samples at 50% SOC and 100% SOC, and on the thin film. The obtained migration and relaxation curves were similar to those from the fresh 0% SOC sample (they are not shown). On the thin film, all fresh samples, and fatigued samples at 50% and 100% SOC ESM response increased during electric potential gradient induced migration for all voltages and almost completely relaxed during chemical

potential gradient induced diffusion, thus indicating stable and reversible migration (dc on) and diffusion (dc off) processes. Contrary, on the fatigued sample at 0% SOC (fully lithiated) the migration in the electric field was stronger than the following relaxation, and not symmetrical with respect to 0 V. The relaxation process was not complete.
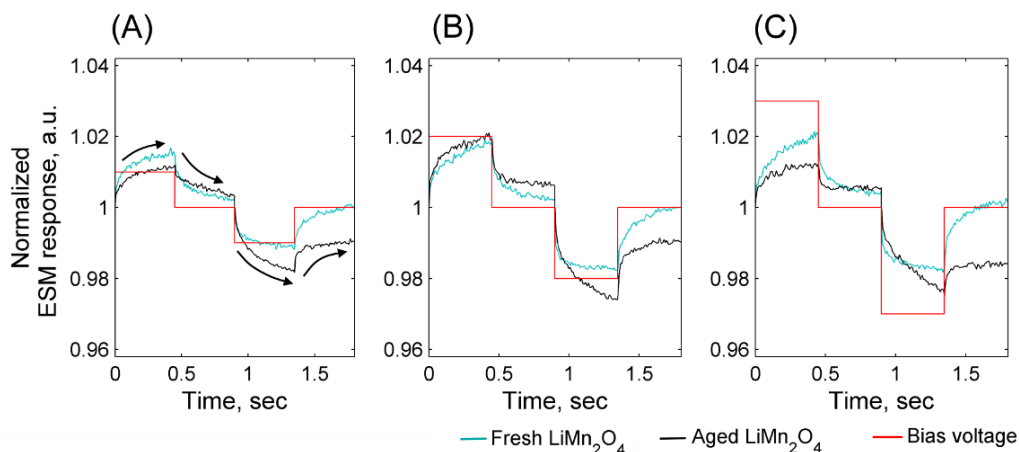
Figure 6.11. Time dependence of the ESM signal. Probing ac voltage was maintained at 3 V. 500 msec dc voltage pulses of ±3, ±4, and ±5 V were applied (red line). ESM response during and after the pulses is measured as a function of time on the fresh (blue curve) and fatigued (black curve) samples at 0% SOC. Curves were averaged over 10 consequent measurements from a single point. Electrostatic linear contribution (when the dc is on) was subtracted.
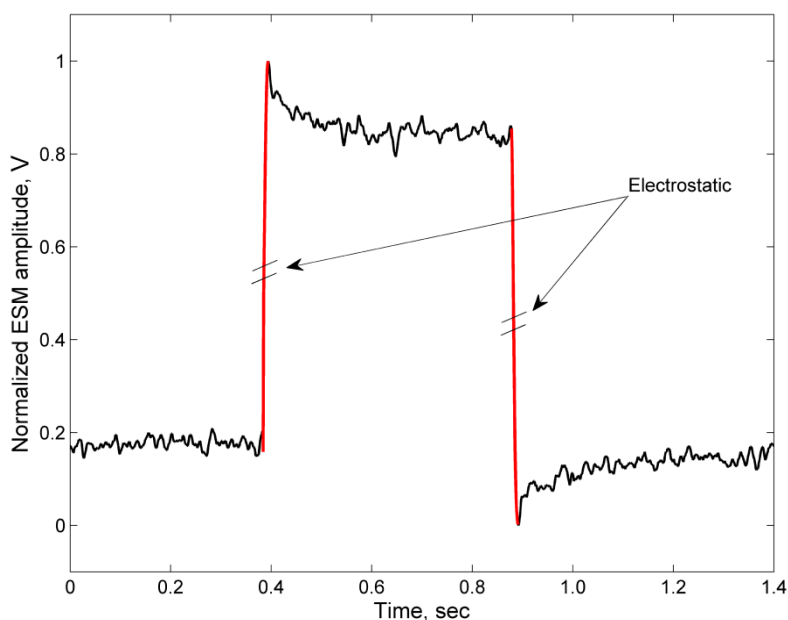
Figure 6.12. ESM response measured vs time during time spectroscopy. The dc pulse was applied between 0.4-0.85 sec. Red lines show electrostatic contribution that emerged when the dc was on and vanished when the dc was off.

The linear electrostatic response when dc is on was subtracted in order to make the migration-relaxation dynamics easier to understand. Figure 6.12 illustrates the ESM time spectroscopy response with the dc on electrostatic contribution.

The obtained relaxation data can be used to qualitatively estimate the local value of diffusion coefficient of Li in $LiMn_2O_4$.

6.4.2 Calculation of the Li diffusion coefficient

Up to now, no theory describing high frequency ESM response in the time domain has been developed. Analytical equations derived by Morozovska et al in Ref. 3 (see Eq. 3.10 and 3.11) are applicable only for the static case, i.e. when the driving ac frequency $\omega=0$, and for D=const. Nevertheless, qualitative estimations can be done using the simplistic approach based on the concept of characteristic diffusion time (see Ref. [143] and Ref. [92] for systems where its use is appropriate).

Characteristic diffusion time approach

Following Jesse et al, [96] we estimated characteristic diffusion times for volumes typically probed by ESM in $LiMn_2O_4$. For the probed diffusion length equal to the tip radius $R_0 \approx 30$ nm and $D_{Li}=10^{-12}–10^{-10}$ cm^{2}s^{-1} [53] the characteristic diffusion time $\tau = l^2 \big/ D =$ 0.1-10 s. In order to compare the diffusion coefficients of Li in the fresh and the fatigued samples, we fitted the relaxation (dc off) curves by the exponential function:

$$u(o,t) = u_0 + A_1 \exp\left(-\frac{t-t_0}{\tau_1}\right) + A_2 \exp\left(-\frac{t-t_0}{\tau_2}\right).$$

The characteristic decay times $\tau_1 \sim 10^{-3}$ s and $\tau_2 \sim 0.1$-10 s were extracted. The slow decay time $\tau_2 \sim 0.1$-10 s is in agreement with the estimated diffusion time and was used to estimate the Li diffusion coefficients via the expression $D = l^2 \big/ \tau$. The calculated diffusion coefficients are plotted in Figure 6.13 as functions of the applied voltage.

The estimated $D_{Li} \sim 10^{-10}–10^{-11}$ cm^{2}s from the thin film and the fresh samples are stable vs the bias voltage and slightly lower after the positive dc pulses than after the negative ones. The diffusion coefficients from the fatigued samples at 50% and 100% SOC are similar to ones from the fresh samples. These data are in good agreement with literature. The only deviation was observed on the fully lithiated fatigued sample at 0% SOC. The estimated diffusion coefficients are 1–2 orders of magnitude lower as compared to the others and decrease with the bias voltage, especially after the negative bias where D_{Li} drops by 2 orders of magnitude. Possible origin of this phenomenon will be discussed below.
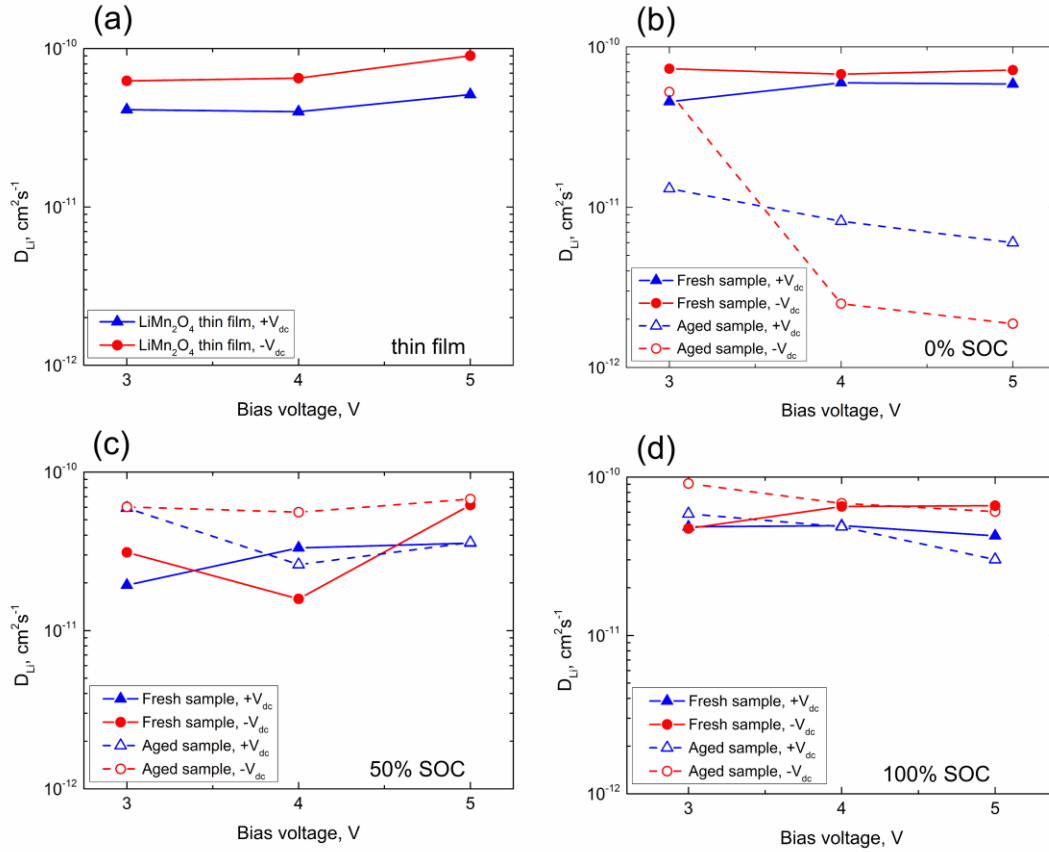
Figure 6.13. Li diffusion coefficient as a function of dc bias estimated from the ESM relaxations on $LiMn_2O_4$: (a) thin film, (b) 0 SOC, (c) 50 SOC, (c) 100 SOC. Integral lines represent the fresh samples. Dash lines represent the fatigued samples.

Static case approach

In the beginning of this paragraph we indicated that the analytical equations for migration and diffusion were derived only for the static case. Here we denote them as "static" in order to highlight that the ac frequency $\omega=0$. Nevertheless, applied to the obtained migration and relaxation curves, they give realistic diffusion coefficients.

In the case of static ($\omega=0$) migration and relaxation curves the local diffusion coefficient for the case of blocking cantilever can be described in the following way (see Eq. 3.10):

$$u(0, t < t_0) \approx -(1+v)\left(\frac{4\beta V_{dc}}{\eta\sqrt{\pi}}\right)\sqrt{Dt} = AV_{dc}t^{1/2} \tag{6.5}$$

$$u(0, t \gg t_0) \approx -(1+v)\left(\frac{\beta V_{dc}R_0^2 t_0}{6\eta\sqrt{\pi D}t^{3/2}}\right) = BV_{dc}t^{-3/2} . \tag{6.6}$$

Eq. (6.5) describes migration during a dc pulse ($t<t_0$), and Eq. (6.6) describes relaxation after a dc pulse ($t \gg t_0$). From the data fitting we can extract numerical coefficients at $V_{dc}\cdot t^{1/2}$ and $V_{dc}\cdot t^{-3/2}$:

$$\begin{cases} A = -(1+\nu)\left(\dfrac{4\beta}{\eta\sqrt{\pi}}\right)\sqrt{D} \\ \\ B = -(1+\nu)\left(\dfrac{\beta R_0^2 t_0}{6\eta\sqrt{\pi D}}\right) \end{cases}. \tag{6.7}$$

After division $A\big/B$ the diffusion coefficient is

$$D = \frac{A}{B}\frac{R_0^2 t_0}{24}, \tag{6.8}$$

where R_0 is the only unknown variable that can be estimated as the tip radius.

More precisely R_0 can be calculated from the point contact resistance equation (if measurable) [144]

$$R_S = \frac{\rho}{2\pi a}\arctan\left(\frac{2b}{a}\right), \tag{6.9}$$

where ρ is the sample's resistivity, a is the contact radius that is equal to R_0, and b is the sample's thickness. In case of $b>>a$ Eq. (6.9) transforms to $R_S = \dfrac{\rho}{4a}$.

Estimations based on Eq. 6.8 gave $D_{Li}\sim10^{-11}$–10^{-12} cm^{2}s^{-1} with the diffusion coefficients after the positive pulses 1.5–2 times lower than after the negative pulses.

Note that under ambient conditions the water meniscus around the ion blocking Pt tip can serve as a reservoir for Li$^+$ ions, so the real tip-surface contact can be not ideally ion blocking. Moreover, equations 6.5 and 6.6 were obtained for the constant diffusion coefficient, while in LiMn$_2$O$_4$ it varies with the Li concentration.

In the end, both approaches gave realistic diffusion coefficient parameters that, however, can be only used to compare to each other within a single approach.

The detailed theoretical description is the future task in this field.

6.4.3 Contribution of the elastic energy to the diffusion coefficient

As was described in Chapter 3 and illustrated in Figure 3.4, the local volume below the tip is clamped and can free-expand only in the direction normal to the surface. Hence, after application of a dc pulse and the local expansion/contraction (strain), the local volume is under compression/tension elastic stress. Corresponding elastic energy contributes to the local diffusion coefficient. Below we describe how the local elastic energy increases the ESM measured diffusion coefficient. For simplicity, in the end we will neglect the anelastic effect, which is present in the anisotropic strain field. [55,145]

In the most general form stress and strain are related by Hooke's law as follows:

$$\sigma_{kl} = \sum_{ij} c_{klij} u_{ij}, \tag{6.10}$$

where σ_{kl} are the components of the second rank stress tensor, c_{klij} are the components of the forth rank tensor of the elastic modules, and u_{ij} are the components of the second rank

strain tensor. Strain in the solid body is described by the dependence of the displacement vector $\boldsymbol{u}$ on the position $\boldsymbol{r}$. The second rank tensor of infinitesimal strain u_{ij} is defined as:

$$u_{ij} = \frac{1}{2}\left\{\frac{\partial u_i}{\partial x_j} + \frac{\partial u_j}{\partial x_i}\right\}. \tag{6.11}$$

Due to the symmetry of the stress (σ_{kl}) and strain (u_{ij}) tensors the number of independent components of the elastic tensor c_{klij} is reduced: $c_{klij} = c_{lkij} = c_{klji}$. It is further reduced by the requirement of the elastic energy to be a unique function of the strain. Thus, in case of the Vegard expansion $\delta u_{kl} = \beta_{kl}\delta C_i$ the elastic energy density δU_{elast} can be expressed as follows:

$$\delta U_{elast} = \sum_{kl}\sigma_{kl}\delta u_{kl} = \sum_{kl}\sigma_{kl}\beta_{kl}\delta C_i , \tag{6.12}$$

where σ_{kl} and u_{ij} are functions of position $r = (r_x, r_y, r_z)$.

Considering a small volume ΔV and a corresponding number of mobile ions $\Delta N_i = \Delta V \delta C_i$ in the volume, the elastic energy takes the form

$$\Delta U_{elast}(\Delta N_i) = \Delta V \cdot \delta U_{elast} = \Delta V \sum_{kl}\sigma_{kl}\delta u_{kl} = \sum_{kl}\sigma_{kl}\beta_{kl}\Delta N_i . \tag{6.13}$$

By definition, the chemical potential $\mu = \Delta U(\Delta N_i = 1)$, so the chemical potential induced by strain can be expressed in terms of stress as follows:

$$\mu_{elast} = \sum_{kl}\sigma_{kl}\beta_{kl} . \tag{6.14}$$

In case of a rectangular lattice with the unit cell natural basis a_i, the i component of the flux density induced by the chemical potential μ_{elast} is:

$$j_i^{elast} = N_i a_i \nu \left(\exp\left(-\frac{1}{k_B T}\left(E_a + \frac{a_i}{2}\cdot\frac{\partial\mu_{elast}}{\partial r_i}\right)\right) - \exp\left(-\frac{1}{k_B T}\left(E_a - \frac{a_i}{2}\cdot\frac{\partial\mu_{elast}}{\partial r_i}\right)\right)\right) =$$

$$= -\frac{\dfrac{\partial\mu_{elast}}{\partial r_i}}{k_B T}N_i a_i^2 \nu \cdot \exp\left(-\frac{E_a}{k_B T}\right) = -D_i\frac{N_i}{k_B T}\frac{\partial\mu_{elast}}{\partial r_i} \tag{6.15}$$

Figure 6.14 schematically illustrates the potential energy barrier distortion caused by the chemical potential gradient and the resulting flux.

For the isotropic diffusion coefficient $D_i = D$ the elastic energy induced flux density j_i^{elast} can be written as:

$$j^{elast} = (j_x^{elast}, j_y^{elast}, j_z^{elast}) = D\frac{N_i}{k_B T}grad(\mu_{elast}).$$

The total flux density includes three parts:

$$j = (j_x, j_y, j_z) = -D\cdot grad(N_i) + D\frac{N_i}{k_B T}grad(\varphi) + D\frac{N_i}{k_B T}grad(\sigma_{kl}\beta_{kl}), \tag{6.16}$$
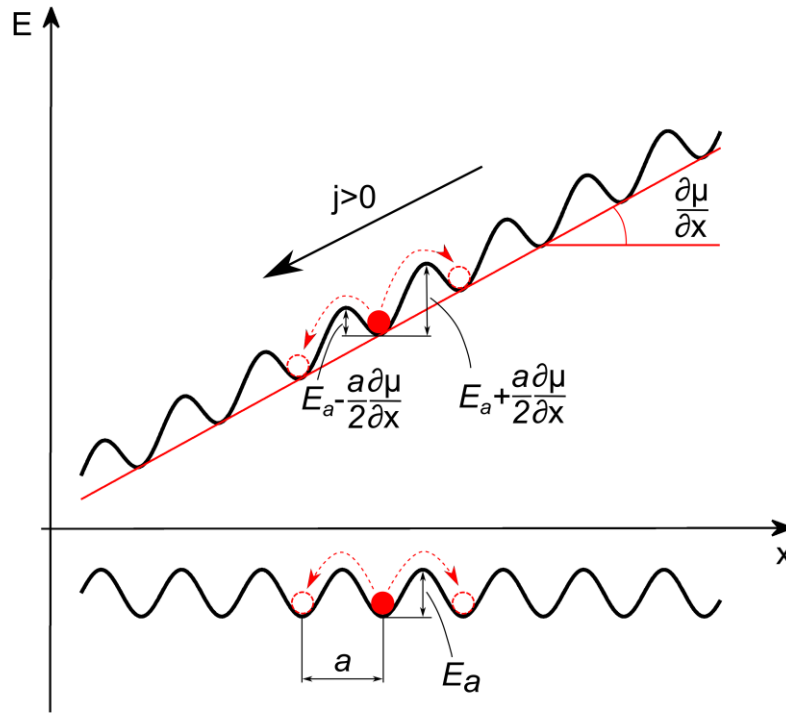
Figure 6.14. Chemical potential originated from the elastic energy $\mu_{elast} = \sum_{kl} \sigma_{kl} \beta_{kl}$ increases the total $\dfrac{\partial \mu}{\partial x}$ and additionally distorts the potential energy barrier, increasing the diffusion coefficient.

where $\varphi = \varphi(r,t)$ is the electrostatic potential distribution. The first term $-D \cdot grad(N_i)$ describes the concentration dependent flux, the second term $D\dfrac{N_i}{k_B T} grad(\varphi)$ describes the electrostatic potential dependent flux, and the third term $D\dfrac{N_i}{k_B T} grad(\sigma_{kl} \beta_{kl})$ describes the elastic energy dependent flux.

Now, consider only the elastic component $\sigma_{kl} \beta_{kl}$. The stress tensor σ_{kl} can be found from the equation of state for the anisotropic elastic media with the concentration excess δN_i, the mechanical stress tensor σ_{ij}, and the elastic strain u_{ij} : [3,93]

$$u_{ij} = \beta_{ij} \delta N_i + s_{ijkl} \sigma_{kl} . \tag{6.17}$$

According to Morozovska et al, [3] displacement field under the tip for the isotropic case is $u_3 \propto -\dfrac{(1+v)}{\pi} \beta h \langle \delta N_i \rangle$, where h is the film thickness, v is Poisson's ratio, and

$\left\langle \delta N_i \right\rangle = \frac{1}{h}\int_0^h \delta N_i(\rho,z)dz$ is the average concentration variation. For the small volume

below the tip $\left\langle \delta N_i \right\rangle \approx \delta N_i$ the maximum elastic strain can be estimated as:

$$u_{ij} \leq -\frac{u_3}{h} \propto \frac{(1+\nu)}{\pi}\beta_{ij}\delta N_i \ . \tag{6.18}$$

Substituting Eq. (6.18) in Eq. (6.17) and multiplying both parts by the tensor of elastic stiffness c_{ijkl} gives the following expression:

$$\sigma_{ij} = -\left(1-\frac{(1+\nu)}{\pi}\right)c_{ijkl}\beta_{kl}\delta N_i \ . \tag{6.19}$$

For an isotropic Young modulus Y the tensor of elastic stiffness for an isotropic linear

elastic solid $c_{ijkl} = \frac{Y}{2(1+\nu)}\left((\frac{2\nu}{1-2\nu})\delta_{ij}\delta_{kl} + \delta_{ik}\delta_{jl} + \delta_{il}\delta_{jk}\right)$ and the Vegard tensor of

chemical expansion $\beta_{kl} = \beta$. Consequently

$$\sigma_{ii} = -\left(1-\frac{(1+\nu)}{\pi}\right)\frac{Y}{1-2\nu}\beta\delta N_i \tag{6.20}$$

Substituting Eq. (6.20) in Eq. (6.16) and changing β_{ikl} to β gives the total flux density in the following form:

$$j = -D\cdot grad(N_i) + D\frac{N_i}{k_BT}grad(\varphi) - D\frac{N_i}{k_BT}\beta^2\left(1-\frac{(1+\nu)}{\pi}\right)\frac{Y}{1-2\nu}grad(N_i) =$$

$$= -D\left(1+\frac{N_i}{k_BT}\beta^2\left(1-\frac{(1+\nu)}{\pi}\right)\frac{Y}{1-2\nu}\right)grad(N_i) + D\frac{N_i}{k_BT}grad(\varphi) = \tag{6.21}$$

$$= -D(1+\alpha)grad(N_i) + D\frac{N_i}{k_BT}grad(\varphi)$$

This equation shows that μ_{elast} effectively increases the diffusion coefficient by the

additional term $\alpha = \frac{N_i}{k_BT}\beta^2\left(1-\frac{(1+\nu)}{\pi}\right)\frac{Y}{1-2\nu}$.

In the case of LiMn$_2$O$_4$ with $\beta \approx 10^{-30}$ m^3, $Y \approx 10^{11}$ N/m^2, $\nu \approx 0.3$, $N_i \approx 1.4\cdot10^{28}$ m^{-3}, and $k_BT = 4.14\cdot10^{-21}$ N·m we calculated $\alpha \approx 0.4$, i.e. the effective diffusion coefficient measured by ESM is about 1.4 times higher than the diffusion coefficient in the decoupling approximation due to the elastic strain contribution.

Using N_i for the samples from Table 4.1 and Y from Ref. [129], we can estimate the effective increase of the diffusion coefficient of Li for each LiMn$_2$O$_4$ sample. In the Ref. [129] the Young modulus' were measured on the fresh samples and on the aged one at 0% SOC. The values for the fresh and for the aged samples at 0% SOC were almost equal. We assume that the same stands for the other samples and will use the same Y for the fresh and aged samples at the same SOC. Calculated results are presented in Table 6.1.

As one can see, the diffusion coefficients are stronger effectively increased for the

Table 6.1. Elastic modulus (Y), Li concentration (N_i), and ($1+\alpha$) coefficient for the $LiMn_2O_4$ samples at different SOC and SOH

Composition	SOH, %	SOC, %	Y, GPa [129]	N_i, 10^{28} m^{-3}	$(1+\alpha)$
$Li_xMn_2O_4$	100	0	87	1.316	1.33
$Li_xMn_2O_4$	100	50	97	1.05	1.29
$Li_xMn_2O_4$	100	100	104	0.854	1.25
$Li_xMn_2O_4$	80	0	87	1.246	1.31
$Li_xMn_2O_4$	78	50	97	1.064	1.29
$Li_xMn_2O_4$*	78	100	704	0.91	1.27

* the cell is unchargable, stopped at 4.08 V

samples at lower SOC, viz. with higher concentration of Li.

Earlier, Zhang et al [146] showed that for the case of spherical $LiMn_2O_4$ particle and hydrostatic intercalation pressure the strain-diffusion coupling effect gives α_{max}=0.356, which is consistent with our results.

6.4.4 Mechanism of the observed diffusion coefficient reduction

In the paragraph 6.4.2 we estimated the local diffusion coefficients of Li in $LiMn_2O_4$ and observed 1–2 order of magnitude drop of the diffusion coefficient on the fully lithiated fatigued sample. Such behavior can be attributed to a number of causes: (i) decrease of the local structural order due to increased concentration of point defects; (ii) cubic to tetragonal phase transition.

(i) Increased concentration of point defects (vacancies, interstitials, composition change of Mn and O atoms) induced by cyclic Li insertion and extraction [147] is a common cause of the Li diffusion reduction because it leads to a partial destruction of the Li transport network within the spinel host structure.

(ii) The tetragonal phase of the lithium manganese oxide has the Li diffusion coefficient that is about an order of magnitude lower than the cubic one. [60] Transition from the cubic to the tetragonal phase below the tip can happen due to local overpotential, thus decreasing the diffusion coefficient. Nucleation of a new phase occurs inhomogeneously on defects, where the nucleation barrier ΔG is reduced. Thus, the sample with higher concentration of defects under the same conditions is expected to experience earlier phase transition and reduction of the diffusion coefficient.

The first case stands for all fatigued samples, but the suppression of the diffusion coefficient was detected only in the fatigued $LiMn_2O_4$ at 0% SOC. It seems that the diffusion coefficient reduction happens not only because of higher concentration of point

defects, but also due to the high initial Li concentration in the 0% SOC fatigued sample (0.89/2 Li/Mn ratio). The higher the initial average Li concentration in the sample, the lower overpotential is needed to locally reach critical Li concentration and initiate the phase transition. The fact that at the same overpotential the phase transition did not happen in the fresh sample at 0% SOC (0.94/2 Li/Mn ratio) indicates that the nucleation barrier *ΔG* for the phase transition is higher in the fresh sample than in the fatigued one. It is possible in case of lower concentration of point defects than in the fatigued sample.

The data were obtained from the polished cross-section of the particles and cannot be attributed to the surface Mn dissolution caused by the disproportional reaction $2Mn^{3+}_{solid} \rightarrow Mn^{4+}_{solid} + Mn^{2+}_{solution}$ or other surface degradation effects. Li insertion/extraction and associated effects (such as instability of the delithiated spinel and onset of the Jahn-Teller distortion in the lithiated spinel) affect the whole particle, increasing concentration of defects. This mechanism is especially important for the case of 16C-rate of discharge, when local Li concentration in the surface region of a $LiMn_2O_4$ particle can exceed the cubic to tetragonal transformation threshold. [148]

Unsaturated and asymmetric migration parts of the time spectroscopy data (shown in Figure 6.11) as well as the characteristic plunge in the beginning of the relaxation curves could indicate additional – non-Vegard – contributions as discussed above. It is worth to point out that such effects have to be considered in order to prevent possible misinterpretation of experimental results, especially in complex oxides. Moreover, they could constitute the sources of additional information about material properties.

Previously reported drop of Li diffusion coefficient during fatigue was attributed to the Mn dissolution and increase of surface resistivity. [149] Our results suggest that it is not the only cause of Li diffusion reduction and at high C-rates the structural instability could extensively contribute to $LiMn_2O_4$ degradation as compared to low and moderate C-rates. Additional information can be obtained by macroscopic measurements of Li diffusion coefficient at different C-rates and SOH in bare $LiMn_2O_4$ particles and in those with a coating reducing Mn dissolution. [150]

6.5 Computer modeling

Earlier in Chapter 3 we noted that previously developed computer models based on the diffusion mechanism of the ac strain generation showed that for $LiCoO_2$ and $LiMn_2O_4$ systems with ion-blocking boundary conditions displacements much below 1 pm are expected for frequencies above 10^4 Hz. [90,108] Such displacements are well below the detection limit of modern SPMs. Nevertheless, the ac mediated Li concentration dependent ESM signal is experimentally detected at hundreds kHz as shown in previous works and in the present study (remember that the ac electric field is used to probe local strain during dynamic processes caused by the dc electric field, and thus should be concentration dependent). This fact arises the question about the real origin of the ESM signal.

In order to get deeper understanding of the ESM, the thermodynamic finite element model was developed by Hugues-Yanis Amanieu (Robert Bosch GmbH, Gerlingen-

Schillerhoehe, Germany; University of Duisburg-Essen, Essen, Germany) and Huy N.M. Thai (University of Duisburg-Essen, Essen, Germany) and compared with the experimental data obtained by Sergey Luchkin and Hugues-Yanis Amanieu in University of Aveiro. The model implemented approach based on the ionic polarization mechanism where the lithium ions are vibrating within their interstitial sites without hopping. This mechanism, being electrostrictive, is active up to THz frequency as shown in Figure 6.15 and can explain the high frequency experimentally obtained response if a background dc is present.

In this model the ESM response is considered linearly proportional to the concentration dependent force $\Im_{ac}(t) = \int_{\tilde{V}} z_{Li} c_{Li}(t) F \nabla \phi_{ac} d\tilde{V}$, where ϕ_{ac} is the local RMS electric potential, F is the Faraday constant, z_{Li} is the Li charge, c_{Li} is the Li concentration, and $\tilde{V}$ is the particle volume. This force is a simplified version of the Lorentz force and should be considered as a mathematical tool to probe the concentration of lithium within a small volume defined by the electric field just under the tip.

In order to compare simulation and experimental results, the model emulated a semispherical particle of a $Li_xMn_2O_4$ single crystal with $x=0.5$ (Li occupies half of the available sites) and $D_{Li}=10^{-14}$ m²s⁻¹. The particle was electrically connected to the closed circuit through the back surface emulating the contact provided by the carbon black in the real battery. The tip-surface junction was blocking and the balance laws of momentum for the mechanical stress, conservation of mass, and conservation of charge were preserved.
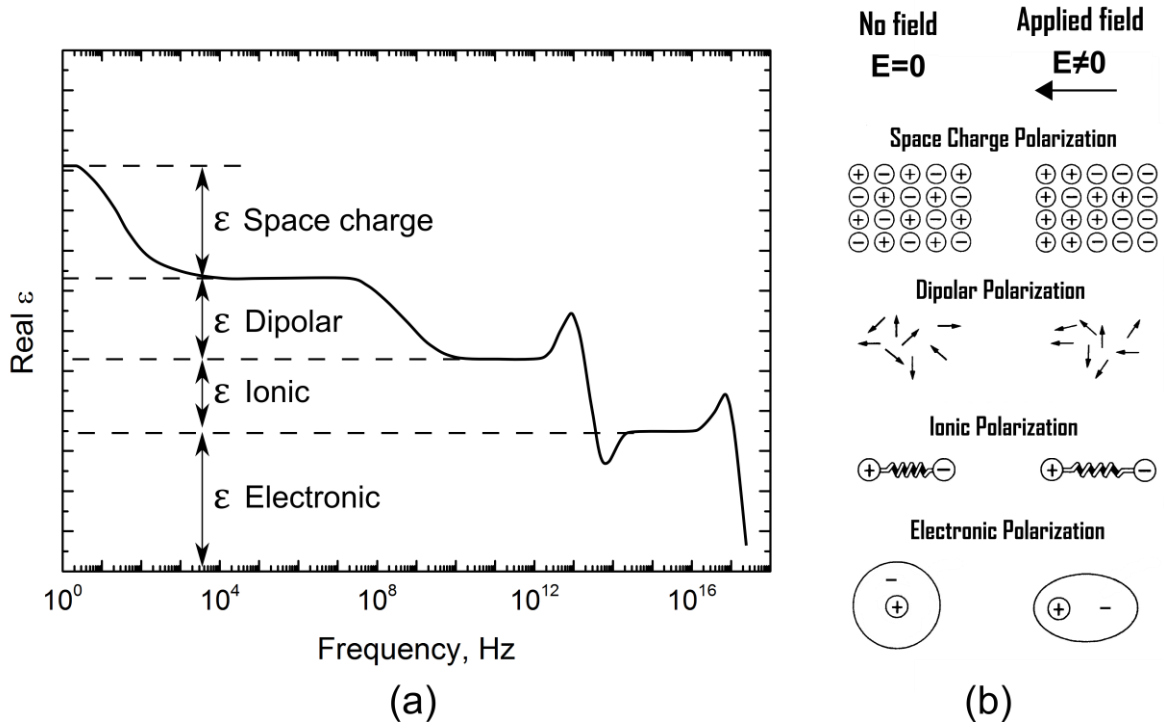
Figure 6.15. (a) Frequency dependence of the real part of the dielectric constant and polarization contributions; (b) schematic representation of different polarization mechanisms (Adopted from Refs. [151,152])

The local electroneutrality below the tip was assumed for simplicity. Coupling between Li^+ ions in real $LiMn_2O_4$ was taken into account through the concentration dependent effective Li diffusion coefficient. The effective diffusion coefficient was derived from the experimental open-circuit voltage in a $LiMn_2O_4/Li(m)$ half-cell as explained in Refs. [14,153] The model was implemented in COMSOL Multiphysics 4.4.

Voltage and time spectroscopies were simulated in order to compare loops and relaxations. The voltage ramp for a simulated loop was 20 dc pulses with 200 msec pulse period (scheme of pulses is similar to one in Figure 3.11). The response was recorded in the dc-off mode.

Figure 6.16 compares the experimentally obtained (a) and the simulated (b) voltage spectroscopy loops. The simulated ESM loop is open resembling experimentally measured ESM amplitude loops with characteristic asymmetrical concentration dependent shape. The presented experimental loop was additionally measured on the 0% SOC 100% SOH $LiMn_2O_4$ sample with the same VS parameters as before, but at 1100 kHz ac frequency. The new experimental result is similar to those presented in Figure 6.4, thus confirming the same nature of the response at 1100kHz as at 100 kHz.

Simulated time spectroscopy relaxations after a single dc pulse possessed the relaxation time of the order of 0.1 sec and the shape similar to the experimental curves. This is in agreement with the characteristic diffusion times estimated above.

The proposed mechanism of the ESM response due to the ionic polarization rather than the ac mediated short range electro-diffusion gives realistic qualitative results for voltage spectroscopy and qualitative results for time spectroscopy. However, the SI numerical ac mediated displacements were not calculated and the solid conclusion about the real origin of the ESM response cannot be made. At this stage, we know that the response is concentration dependent and can be used to qualitatively evaluate Li mobility/concentration. In order to make it quantitative, the real origin of the ESM signal generation have to be understood.
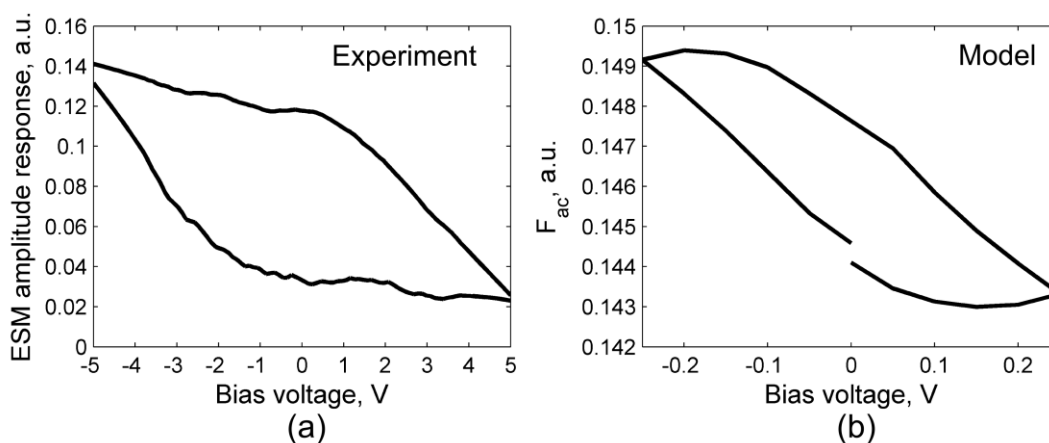
Figure 6.16. The experimentally measured at 1100kHz ESM amplitude hysteresis loop (a) and the simulated hysteresis loop (b).

Conclusions

In this Chapter, the appropriate voltage range for ESM measurements on $LiMn_2O_4$ was experimentally determined. Additional non-Vegard response was demonstrated and its possible origins were discussed. We showed that the ESM method cannot be blindly applied to any ion conducting material. Beforehand, material's specific properties have to be analyzed in order to reveal possible contributions to the measured signal. This is an essential step for correct interpretation of experimental results.

Voltage spectroscopy measurements showed less uniform distribution of loop opening on the fatigued $LiMn_2O_4$ samples as compared to the fresh ones. It was explained by stronger contribution of non-Vegard terms on the fatigued samples due to increased concentration of point defects upon cycling. Moreover, the wider loop opening was observed on the samples with lower lithium concentration. Two possible mechanisms were suggested to explain the observed behavior: (i) higher Li diffusion coefficient in the samples with higher Li concentration, and (ii) saturation of available Li positions in the host lattice within the cubic phase.

Time spectroscopy measurements were used to estimate local Li diffusion coefficients in the samples at different states of charge and health. The obtained results revealed a reduction of Li diffusion coefficient in the fatigued sample at 0% SOC (fully lithiated) as compared to all other samples. This effect was attributed to the structural degradation during 16C-rate cycling and the electric field mediated cubic to tetragonal phase transition below the tip.

Further, we calculated contribution of the elastic energy to the diffusion coefficient. The effect can effectively increase the diffusion coefficient by 1.3-1.4 times in $LiMn_2O_4$, thus the strain-diffusion coupling cannot be neglected when Li diffusion is quantifed.

The finite element modeling was performed and compared with the experimentally obtained data in order to deeper understand origin of the ESM response. Since the earlier performed calculations showed the ac mediated displacements well below the SPM detection limit, the implemented model utilized the ionic polarization mechanism of the ac mediated response rather than the Vegard one. The obtained simulation results were qualitatively similar to the experimental one. Quantitative estimation (in SI units) of the ac mediated displacements for the case of ionic polarization was not done, and the solid conclusion about origin of the ESM response cannot be made at this stage. Further experiments and theoretical calculations are required.

Summarizing, we conclude that the ESM is a potentially powerful technique able to probe local transport properties in ion conducting materials at the nanoscale. We established that the response is concentration dependent and can be used to qualitatively evaluate ionic mobility/concentration. However, since the real origin of the ESM response is not fully understood, the complete interpretation and quantification of the experimental results is still challenging.

Chapter 7

Li concentration in graphite via KPFM

In the previous Chapter we showed how to use ESM to study transport properties of the $LiMn_2O_4$ cathodes of commercial Li-ion batteries. ESM locally affects Li ions by the applied electric field and receives information about local Li mobility/concentration by measuring dynamic surface strain. At present, reliable quantification of physical variables from ESM data is challenging. Additional information about local Li concentration can be obtained by Kelvin Probe Force Microscopy. KPFM is sensitive to the electronic structure of materials and, consequently, to its composition, so it can detect spatial distribution of Li^+ ions inside electrode materials with a resolution down to the nanoscale.

This Chapter summarizes KPFM results obtained mainly on graphitic anodes at different stages of charge and health. The results revealed that at 16 C-rate cycling relatively big structurally integral particles possess a core-shall distribution of the surface potential (presumably indicating Li concentration). By contrast, similar particles without cycling showed a mosaic distribution of the surface potential, which was attributed to inactivated regions of lithiated graphite at the early stage of cycling. Additional results obtained on the $LiMn_2O_4$ cathodes showed that the pitting corrosion of the Al current collector could be another source of internal resistance and associated capacity fading.

7.1 Methodology and calibration

Surface potential of the samples was measured by means of the 2-pass amplitude modulated Kelvin Probe Force Microscopy (AM-KPFM). [79] Ac voltage of the second pass was 0.5 V in amplitude, lifting height was always 15 nm; scan resolution is 256×256 points. To avoid a shift of ΔV_{CPD} measured on a biased device in AM-KPFM mode, [86] the investigated samples were not electrically biased.

One can argue that AM-KPFM has lower spatial resolution than FM-KPFM. [85] However, AM-KPFM has higher energy resolution and can detect lower minimum detectable ΔV_{CPD} as compared to FM-KPFM, which was described in details in Chapter 3.

We used Pt/Ir coated cantilevers (NT-MDT NSG10, resonance frequency ≈ 250 kHz, force constant ≈ 12 N·m^{-1}) which were calibrated on a sputtered Au thin film and on a cleaved HOPG calibration sample. The calibration and measurements were performed under ambient conditions at 40% relative humidity (RH). Measured contact potential difference between the Au film and the tip was $V_{CPD} = -(57.8 \pm 0.3)$ mV. According to the recommended values of work functions [81] (see Table 7.1), V_{CPD} should be in -(19–11) mV range. The difference can be explained by the impact of the ambient humidity, resulting in the absorbed water layer that can screen the work function difference. [154] Measured contact potential difference between the HOPG calibration sample and the tip was $V_{CPD} = (318.8 \pm 5.6)$ mV that is within the table range. Note that presented in literature work function values for Au and Pt are scattered in a wider range as compared to those presented in Table 7.1.

Table 7.1. Recommended work functions for polycrystalline materials (Ref. [81])

Material (polycrystalline)	Work function, eV
Au	5.31±0.07
Pt	5.27±0.08
Cu	4.51±0.07
Graphite	4.6±0.1; 5.0

The Pt/Ir tip coating is 25 nm thick and is subjected to wearing during scanning. As a result, the tip apex could become the bare n-type silicon while the rest of the tip will remain covered by the Pt/Ir alloy. This defect leads to change of the measured V_{CPD} [155] and, being ignored, could cause erroneous interpretations of results. Similar effect can be caused by contamination of the tip apex. On this account, areas subjected to measurements in our experiments always included a part of the Cu current collector, which work function was considered as a reference. As illustrated in Figure 7.1, the tip damage effect can be clearly noticed by the shift of the Cu V_{CPD}. This is a simple way to recognize the described error.

7.2   Surface potential of the graphitic anodes

7.2.1 Measurements

The main measurements were performed on the graphitic anodes in the delithiated state (samples №2 – fresh – 100% SOH, 0% SOC; sample №6 – fatigued – 80% SOH, 0%
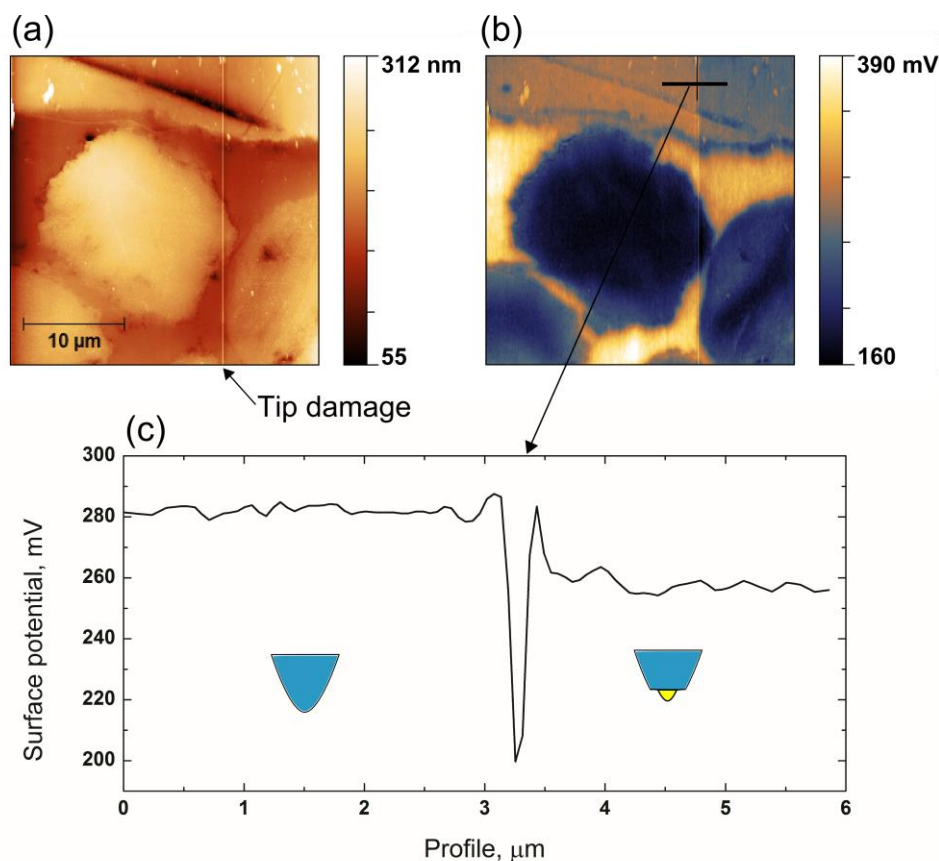
Figure 7.1. Illustration of the Pt/Ir coating damage effect on the KPFM surface potential of the graphitic anode at 80% SOH 0%SOC: (a) topography, (b) surface potential, (c) surface potential profile. V_{CPD} before and after the damage is ≈20-25 mV.

SOC). The lithiated graphite samples were not studied because they are not thermodynamically stable under ambient conditions that results in formation of a film on the particle's surface due to reaction of Li with ambient gases and absorbed water. The lithiated sample №8 (78% SOH, 50% SOC) was used to gather additional data.

Figure 7.2 (a, b) illustrates simultaneous mapping of topography and surface potential (SP) of the fresh anode (100% SOH, 0% SOC). Graphite particles and the Cu current collector are clearly distinguishable inside the polyvinylidene fluoride (PVDF) binder filled with the epoxy resin. Surface potential on the graphite particles is not uniform: there are internal regions with reduced down to 200 mV surface potential (Figure 7.2 (b), dark color). Cross-section of the KPFM signal (line 1 in Figures 7.2 (a) and (b) correspond to Figure 7.2 (c)) clearly demonstrates that the surface potential within these regions is flat around 200 mV with sharp boundaries.

Though the surface potential image looks similar to the topography image, it is not due to the topography crosstalk. The sample is a composite that contains a number of different materials, viz. copper, graphite, PVDF with carbon black, and epoxy. Each of these materials has its own surface potential, therefore the topography and the surface potential images correlate with each other, but not identical. The comparison of the surface
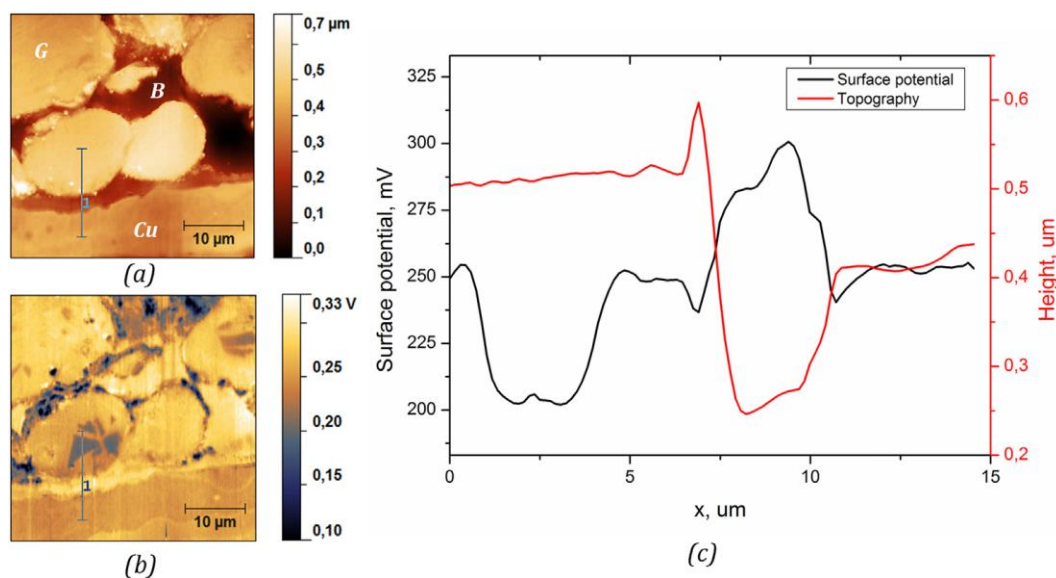
Figure 7.2. Topography (a), surface potential (b), and cross-sections (c) of the fresh graphitic anode (100% SOH, 0% SOC). On the topography image "Cu" denotes the Cu current collector, "G" – active graphite particles, "B" – the binder filled with the epoxy. Notice regions of the reduced surface potential inside graphite particles on the surface potential image (b). (Reproduced from Ref. [109])

potential profile with the topography profile (Figure 7.2 (c)) unambiguously proves that the reduced potential did not come from the topography crosstalk.

Figure 7.3 illustrates a peak distribution assigned to the Cu current collector, the "normal" graphite, and the graphite with the reduced potential (internal areas) from Figure 7.2. All peaks are narrow enough with similar full width at half maximum (FWHM) and without broad transition regions (as for the fatigued sample, see below). It indicates uniform composition of the areas from which the peaks were collected.

Figure 7.4 (a, b) illustrates topography and surface potential of the fatigued sample. The first striking observation is that the surface potential of graphite particles strongly depends on the particle's mechanical integrity. Several particles on the upper half of the topography image have open cracks that are filled with epoxy (that also prove cracks are not due to the polishing process). Surface potential on these particles is less uniform and is lower (vs. Cu) than in the fresh sample, but not as low as on dense particles on the bottom half of the image. The second striking observation is that the surface potential on the big (≈ 25×15 μm) dense particle forms the core-shell structure with almost linear decay in the ≈ 5 μm shell region toward the constant bottom level in the core region (Figure 7.4 (b, c)). The shell region corresponds to the broad transition part in the surface potential peak distribution in Figure 7.5 ("Graphite 2" peak). The reduced potential in the core corresponds to the narrow peak at the end of the transition region in Figure 7.5. Small (≈ 10 μm) dense particle in contact with the big one shows quite low SP without the core-shell structure.

Peak distribution in Figure 7.5 clearly demonstrates that the Cu surface potential peak remains narrow without transition regions – similar to the Cu surface potential peak
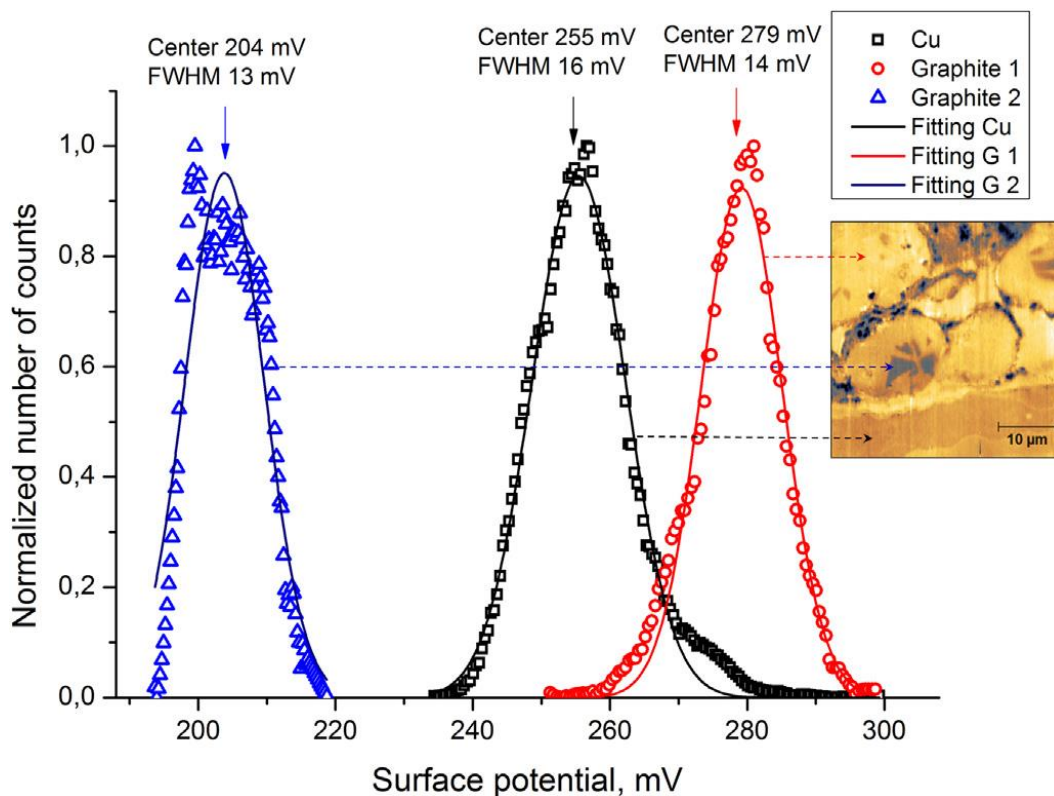
Figure 7.3. Surface potential distribution from Cu and graphite parts of the fresh sample. Arrows show corresponding surface potential on the surface potential image of the sample. (Reproduced from Ref. [109])
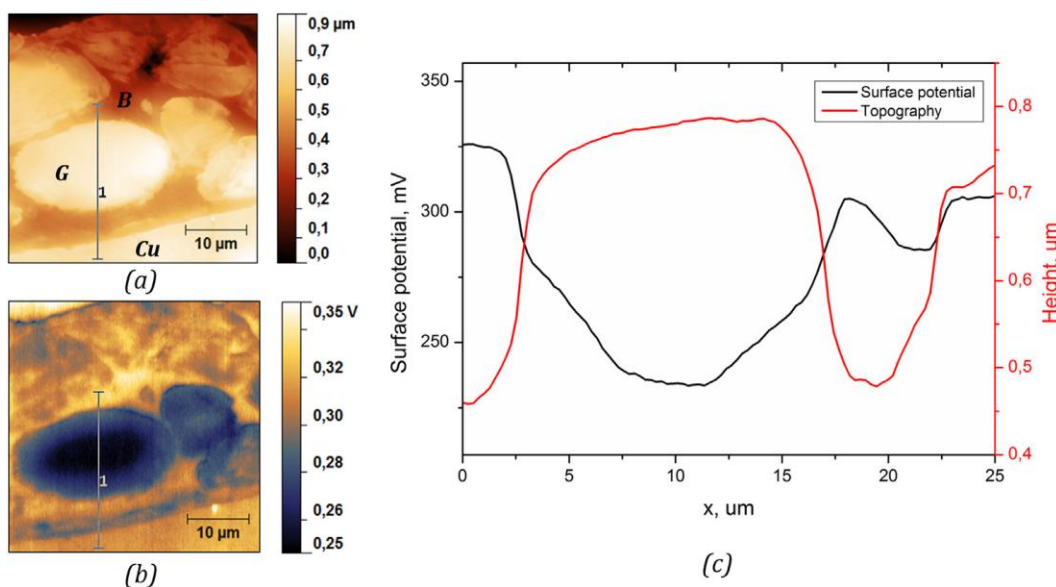
Figure 7.4. Topography (a), surface potential (b), and cross-sections (c) of the fatigued anode. On the topography image "Cu" denotes the Cu current collector, "G" – active graphite particles, "B" – carbon black enriched with PVDF binder filled with epoxy. Core-shell structure is evident on the big dense particle on the surface potential image (b). (Reproduced from Ref. [109])
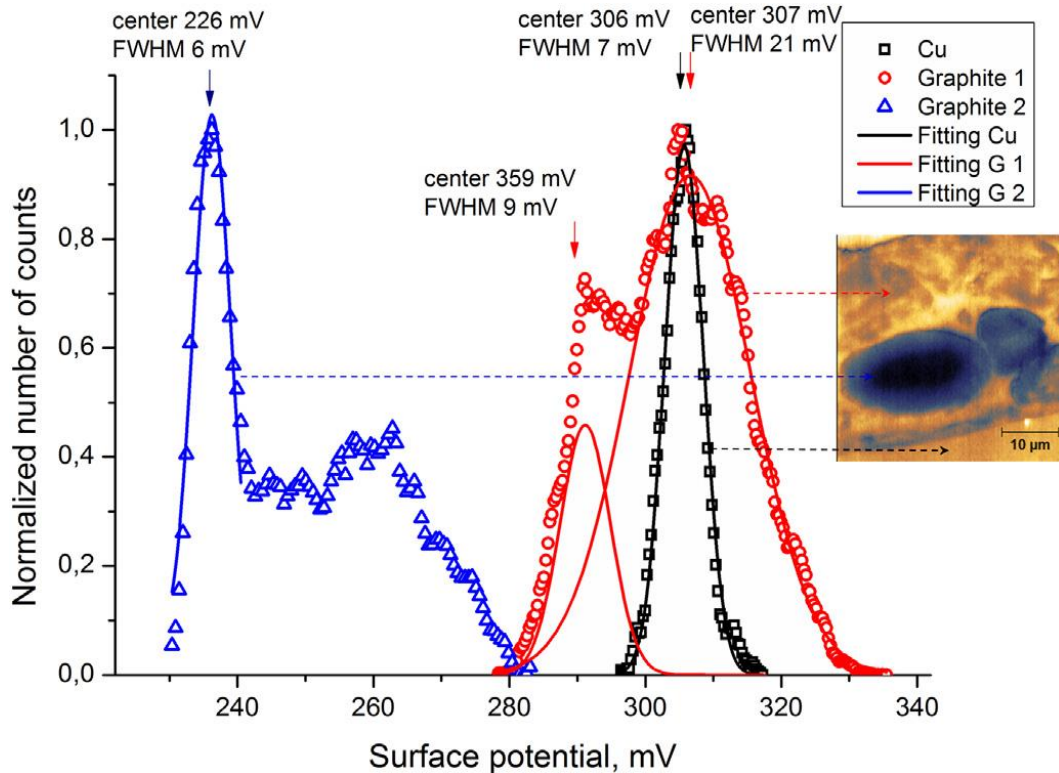
Figure 7.5. Surface potential distribution from Cu and graphite parts of the fatigued anode. Arrows show corresponding surface potential on the surface potential image of the sample. (Reproduced from Ref. [109])

of the fresh specimen. On the contrary, both graphite peaks are drastically different in comparison with the fresh sample: they are much broader and have transition regions.

A total of 8000 μm^2 were scanned in order to exclude the statistical error. Each crack-free particle with more than 10 μm minimum size has similar core-shell type of surface-potential with the shell width around 5 um.

For 40×40 μm scan size with 256×256 points density the resolution is 156 nm/point. Taking into account 10–50 nm thickness of the SEI layer [29] and the blur effect of the absorbed water layer the resolution is not sufficient to observe the SEI layer effect on edges of graphite particles.

7.2.2 Impact of humidity

The measurements were performed under ambient conditions. This means that there is inevitable an adsorbed water layer on top of the surface. It is well known that the adsorbed water layer screens surface potential due to formation of dipoles. Hence, the measured potential difference is lower than the actual one. Different authors have reported different impacts of absorbed water. On the one hand, Bluhm et al [154] demonstrated a decrease of the surface potential on dry mica from +350 mV at RH=0% down to zero at RH=40%. Zaghloul et al [156] documented similar results on SiN$_x$ surface, where surface potential of the trapped charge was reduced from ≈ 5 V at RH = 0.02% to ≈ 2 V at RH =

40%. On the other hand, Hansen and Hansen [157] reported almost negligible contribution of humidity to the measured surface potential in highly ordered pyrolytic graphite (HOPG). Ono et al [158] found that the surface potential of InAs decreased more than 25% after the thermal treatment that removed the adsorbed water layer from the surface. Obviously, the humidity impact on KPFM results strongly depends on a type of probed materials due to its different hydrophobic properties.

We consider the impact of humidity only on the graphite and Cu surfaces and ignore the epoxy. Based on the calibration data taken on the Au thin film and on the HOPG sample, we assume that the impact of the absorbed water layer on the graphite and the Cu potential is similar and ~50 mV.

7.2.3 Effect of the Cu oxide layer

Another reason for the surface potential deviation from the table values of the work function difference (see Table 7.1) is presence of oxides. Apart of the adsorbed water, only Cu_2O can change the surface potential. According to Przychowski et al, [159] presence of the copper oxide leads to an increase of the work function as compared to the pure metal. They reported a change in the work function from 4.45–4.95 eV on the pristine surface to 4.65–5.05 eV on the surface exposed to oxygen. Remarkably, the work function increased with time of the exposition and tended to saturation at 5.05 eV. It is equal to a drop of the surface potential on the oxidized surface as compared to the unoxidized one. Using data from Table 7.1, the work function difference between Pt and Cu is W_{Pt} - W_{Cu} = (0.76 ± 0.11) eV. Using data from Przychowski et al, [159] W_{Pt} - $W_{Cu/Cu2O}$ ≈ 5.3 - 5.05 = 0.25 eV that is equal to 0.25 V surface potential value. Hence, the copper oxide should decrease the measured surface potential down to 250 mV. The copper surface potential peaks in Figures 7.3 and 7.5 are in the same range ≈ (250–300) mV (i.e., 0.25–0.30 eV) being in a good agreement with the above result.

Further, we use the Cu surface potential as the reference value that should be the same for both samples and which shift is related to the RH change. Quantitative comparison of the graphite surface potentials from different samples was done with respect to the Cu surface potential.

7.2.4 Graphite surface potential

Figure 7.3 revealed that the surface potential value of graphite on the fresh sample is 279±14 mV. According to Table 7.1, W_{Pt} - W_G ≈ 5.3 - (4.5–5.0) = 0.6–0.3 eV (equal to 600–300 mV). As one can see, the experimental value of the graphite potential is in a good agreement with the table data if the graphite work function ≈ 5.0 eV. Small difference can be attributed to the absorbed water layer.

Surface potential reduction

We consider three possible physical mechanisms of the observed surface potential change in the graphitic anodes: (i) graphite structural disorder, (ii) Li intercalation, and (iii) appearance of the reaction products and following contamination of the surface.

(i) Structural disorder of graphite during cycling is a well known phenomenon. Obraztsov et al [160] show that a disordered graphite with sp^3-like defects in the sp^2 network possesses a lower work function as compared with a highly ordered pyrolytic graphite (HOPG). This should apparently result in the surface potential increase. However, the experimental results show that graphite of the fresh and the fatigued anodes has surface potential equivalent to the fresh graphite work function (Figure 7.3 (b)) or lower (Figure 7.5 (b)), i.e. opposite to what is expected. This fact rules out the structural disorder effect as the main contribution to the surface potential variation.

(ii) Another possible source of the surface potential change is presence of remnant Li^+ ions in the graphite active particles. It is long time known that doping of graphite by alkali, alkali-earth, and rare-earth elements leads to formation of a surface dipole layer that reduces the initial work function. [161] Thus, the Li-intercalated graphite must have lower work function as compared with the fresh graphite. According to $V_{CPD} = \dfrac{W_{tip} - W_{sample}}{-e}$, it should also results in the higher surface potential, that is not the case. It means that the Li intercalation may not be the dominant mechanism responsible for the observed effect.

(iii) As pointed out above, the KPFM measurements were performed under ambient conditions, i.e. the anode samples (polished cross-sections) were exposed to humid atmosphere. Lithiated graphite is not stable under ambient conditions, hence we suggest that Li^+ ions reacted with the ambient gases and the adsorbed water, and formed a layer of reaction products on the graphite surface. The surface film typically is a mixture of the following reaction products: Li_2O, Li_3N, $LiOH$, and Li_2CO_3. All these compounds reduce the overall surface potential relative to the fresh graphite. [162–164] Moreover, the thicker layer of the products – the stronger should be the surface potential reduction. [162] Hence, the observed decrease of the surface potential on the cross-sections of the graphite active particles in the fatigued sample can be attributed to the surface layer of the Li reaction products. We believe that almost linear decline in the shell region is a natural result of the increasing thickness or density of the surface film towards the core region that correlates with the Li concentration in the graphite material underneath. Consequently, the lowest surface potential in the core region must correspond to the highest Li concentration in the graphite.

To confirm the proposed model we studied the lithiated anode with 78%SOH and 50% SOC. At this SOC significant concentration of Li is certainly present in the graphite. Under ambient conditions the layer of reaction products is formed on the surface. Measured surface potential and topography are shown in Figure 7.6. The topography after the ion polishing is equivalent to the fresh and the fatigued samples. The surface potential of the graphite particles is suppressed as compared to the graphite of the fresh sample
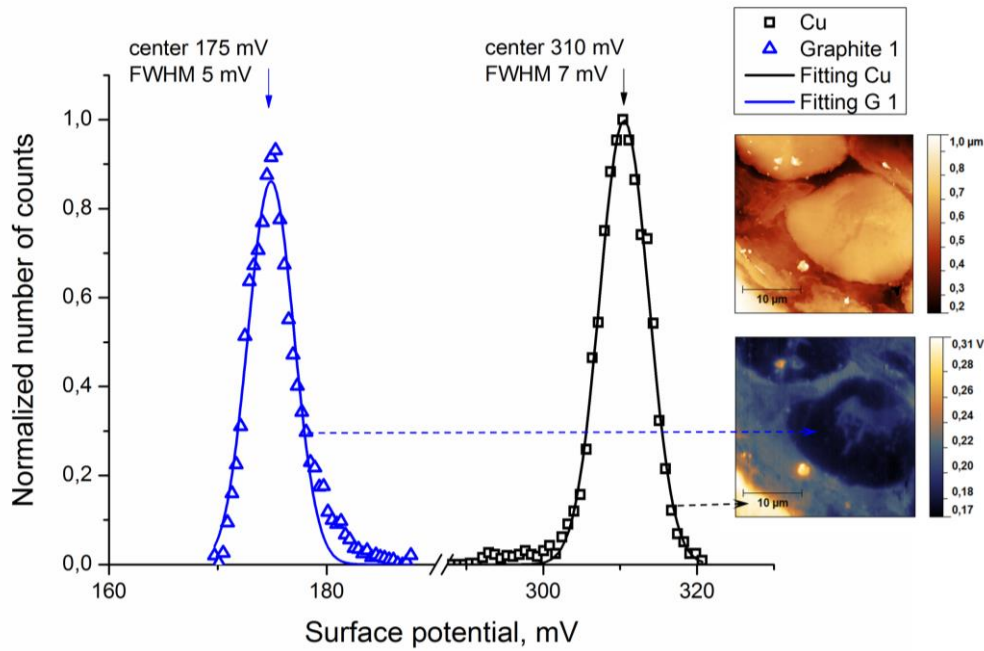
Figure 7.6. Surface potential distribution from Cu and graphite parts of the lithiated sample. Arrows show corresponding surface potential on the sample. Right top and bottom images are topography and surface potential respectively. (Reproduced from Ref. [109])

without Li^+ ions (Figure 7.2). Note, that in the proposed model the higher Li concentration (and the thicker/denser reaction products surface layer) results in the lower surface potential. Using the Cu surface potential (V_{Cu}) as a reference, for the suppressed surface potential regions of graphite V_{Cu} - $V_G \approx 75$ mV for the fresh sample, ≈ 81 mV for the fatigued sample, and ≈ 135 mV for the lithiated 50% SOC sample. This clearly supports the proposed model of the surface potential suppression.

Further prove of the model was obtained by direct observation of the surface film during high-resolution scanning of the fresh sample with the mosaic surface potential suppression (Figure 7.7).

Note that the effect of the surface screening layer should disappear when anodes are not exposed to humid atmosphere and KPFM measurements are done under controlled inert atmosphere or vacuum.

7.2.5 Explanation of the shape of reduced surface potential regions

For quantitative estimations we took the Li diffusion coefficient in graphite in the range 10^{-9}–10^{-10} cm^{2}s^{-1}. [7] Based on these values, at 1C-rate Li can completely deintercalate form a particle with up to 40 μm size, while at 16C-rate Li can deintercalete from a particle with up to 10 μm size as predicted by a simple formula:

$$l = \sqrt{D\tau}.$$
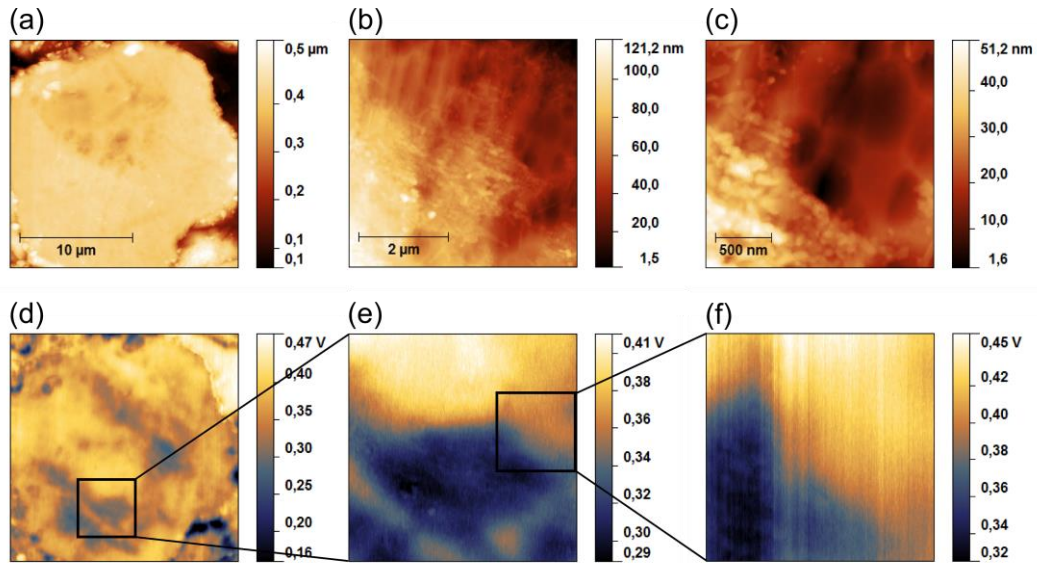
Figure 7.7. Topography (a), (b), (c) and surface potential (d), (e), (f) of the graphite particle of on the sample №2 (100% SOH 0% SOC). 10-20 nm thick layer of the reaction products partly cover the surface and screens the surface potential.

Here D is the Li diffusion coefficient, τ is the diffusion time, and l is the diffusion length.

At 1C discharge rate of the fresh cell lithium ions had enough time to deintercalate from the particles. Still, areas of the suppressed surface potential were observed. These might be Li_xC_6 domains of still electrochemically inactive Li within the delithiated graphite. Indeed, Figure 4.2 shows the discharge capacity increase during the five first cycles, i.e. the activation step. This behavior can be explained by the fact that some lithium ions are not yet activated in the beginning of cycling. Being trapped within the graphite and subjected to polishing and exposure to atmosphere, these remaining ions reacted with the atmosphere gases and reduced the surface potential where they were present.

In the fatigued at 16C-rate sample deintercalation during cycling was not complete. The output battery voltage at a constant current is a combination of a battery electrochemical potential (E_0) and a potential determined by an internal resistance (R_i):[165]

$$V=E_0-IR_i$$

The internal resistance consists of several components such as electrolyte resistance, polarization, SEI layer, etc., but one important cause of increasing resistance is a loss of mobile charges, i.e. Li^+ ions. At 16C-rate Li can pass up to 5 µm that corresponds to the shell region size (Figure 7.4 (b, c)). Consequently, during discharging at 16C-rate battery passes at least two steps. First step with sufficiently small internal resistance until Li^+ diffusion pathway is shorter than the shell width (5 µm). During this step, the number of deintercalating Li^+ ions is high enough to provide a required current. At the second step the amount of available mobile Li^+ ions within the short pathway area is not enough to provide a required current, so the internal resistance leaps upwards. The total battery voltage decreases below the cut off voltage, so the battery indicates discharge though it is not fully

discharged. This might explain the presence of Li in the core region during cycling and the observed core-shell surface potential structure.

The fact that during cycling with 16C-rate discharge Li was extracted only from the shell region and remained blocked in the core region due to the diffusion limitation directly correlates with the reversible reduction of the specific capacity during cycling at higher C-rates as compared to lower C-rates. [1]

Nevertheless, after aging at 16C-rate the battery was finally discharged at 1C-rate and Li^+ ions might fully deintercalate from the particle, but it did not happen (according the proposed model).

Obviously, the shell region – where Li is constantly inserted and extracted – should be much more structurally disordered as compared to the core region (where Li was inserted only during the first charge step). According to Gnanaraj et al, [166] Li intercalation mechanisms into graphite and disordered carbon are different. In the ordered graphite the Li intercalation/deintercalation is the staging process, while in the disordered carbon it is not. Linear decay of the shell region surface potential might indicate absence of the staging phenomena. However, the potential step chronoamperometry did not reveal any correlation between the phase boundary movement and degree of crystallinity. [17] Therefore, different intercalation/deintercalation mechanisms cannot be confidently used to explain the obtained results.

Possible explanation is the continuous network of defects (such as dislocation walls) around the core. Lattice parameter *c* along the z-axis is 3.359 Å for the pristine graphite and 3.712 Å for LiC_6. [22] During the high C-rate cycling the core region interlayer distance (if LiC_6 is the core phase) remained constant at 3.712 Å, while the shell region interlayer distance varied from 3.359 Å to 3.712 Å and vice versa. Moreover, according the model proposed by Yue Qi et al, [167] the Young's modulus of polycrystalline graphite is increased threefold during lithiation of pristine graphite to LiC_6 with simultaneous weakening of C–C bonds in basal planes. Within this model, where phase transitions are: pristine graphite to LiC_{18}, LiC_{18} to LiC_{12}, and LiC_{12} to LiC_6, the maximum tension occurs at the LiC_{12} to LiC_6 transition – what we expect at the surface potential core-shell interphase. Such strong lattice parameter change between the phases with different mechanical properties can lead to significant mechanical stress between the core and the shell that can break the C-C bonds [19] at the interphase. Prolonged cycling that periodically produces mechanical stress within the same area should leads to fatigue and massive structure damage on the surface potential core-shell interface. Due to the fact that Li intercalates inside layers of graphite and hardly can jump from one layer to another, significantly damaged edges within the bulk can hinder Li deintercalation.

Another important observation on the fatigued sample is that the surface potential distribution on the cracked particles and on the dense particles significantly differs. The big cracked particle shows higher surface potential than the dense one and without the core-shell type of the surface potential (Figure 7.4). It means that there are less remnant Li ions inside. Taking into account that all observed cracks are filled with the epoxy (Figure 7.4 (a)), we can conclude that the electrolyte had access to all internal surfaces and Li diffusion

paths were significantly shorter than in the dense particle of the same size. Consequently, the remnant Li concentration and corresponding surface potential of the cracked particle do not depend on the particles size.

Note that the crack's surface consumes Li due to formation of the new SEI layers as soon as the crack is formed. This process continuously happens upon cycling.

Furthermore, the mosaic and radial models [168] can be introduced in order to explain the observed behavior. It summarizes the discussed above experimental data and proposed mechanisms.

According to the mosaic model (Figure 7.8 (a)), inactive Li^+ ions are trapped within the Li_xC_6 domains after the full discharge. The domain boundaries can be pinned by localized crystallographic defects such as dislocations. During cycling, lithium insertion and extraction gradually redistribute these localized defects along with generation of new randomly distributed defects. This process activates trapped Li^+ ions during first several cycles (5 in the present 16C discharge rate case). The mosaic model is size independent.

(a)

(b)
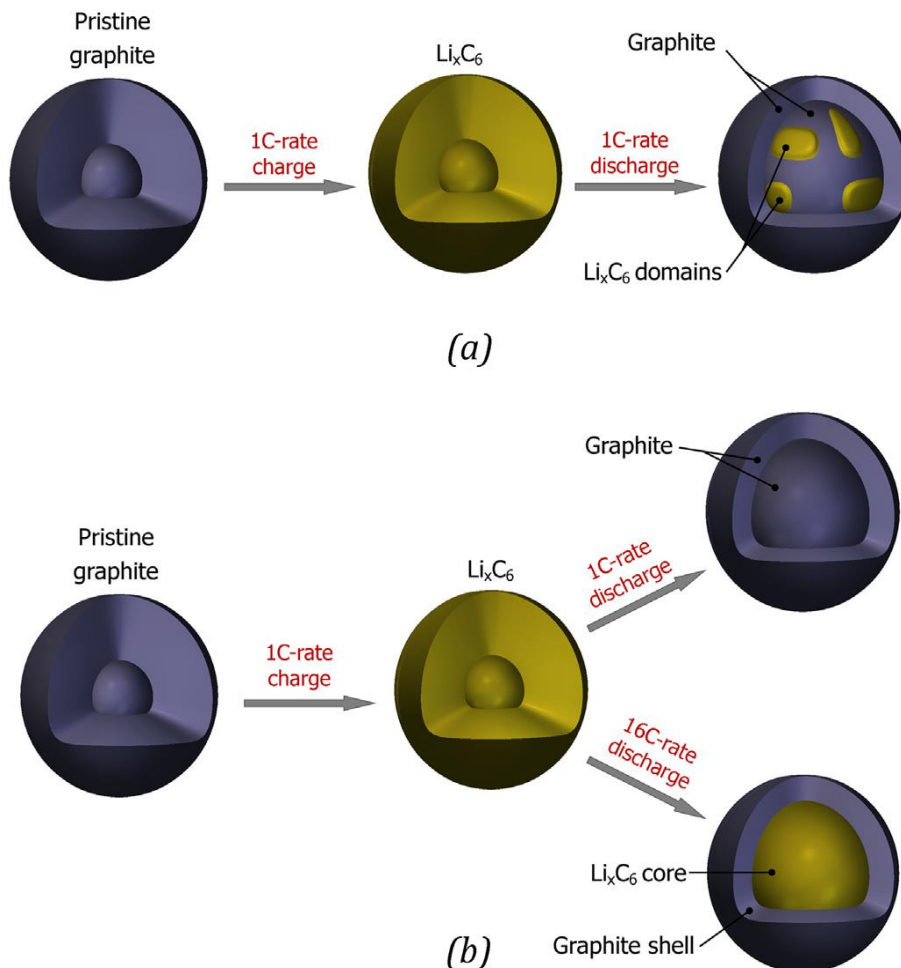
Figure 7.8. Schematic illustration of the "mosaic" (a) and the "radial" (b) models of Li blocking within the bulk. (Reproduced from Ref. [109])

According to the radial model (Figure 7.8 (b)), at the high C-rate the core of the blocked Li_xC_6 phase is formed due to the diffusion limitation: at a given C-rate (discharge time) Li can diffuse at a certain length determined by $l = \sqrt{D\tau}$. After the prolonged cycling at high C-rate the shell region is much more structurally disordered than the core one, and the continuous network of defects (C–C bonds disruption) around the core hinders Li of the core from deintercalation even at low C-rate discharge. This model is applicable only if the diffusion length is smaller than the particle radius, i.e. it is size dependent.

These two models can coexist within a single particle: experimental results suggest a transition from the mosaic model at the beginning of cycling to the radial model after the prolonged cycling.

7.4 KPFM of the $Li_xMn_2O_4$ cathodes

Measurements performed on the fresh and the fatigued $LiMn_2O_4$ samples did not reveal any consistent dependence of V_{CPD} on both SOC and SOH. We expected around 2 V V_{CPD} between the $Li_xMn_2O_4$ particles and the Pt/Ir tip with slightly higher V_{CPD} for the lithiated samples. Indeed, the calculated Fermi levels for λ-MnO_2 is -3.213 eV, for $LiMn_2O_4$ is -3.097 eV, and for $Li_2Mn_2O_4$ is -2.578 eV. [169] Owing to the fact that $LiMn_2O_4$ is a semiconductor, deviations from these values can be caused by the band banding that in principle can be different for different Li content for the same external voltage (Li is the n-doping element). Nevertheless, we did not expect the drastic drop of the V_{CPD} that was observed – the measured V_{CPD} were around 0 V independently of SOC and SOH. We assume that $LiMn_2O_4$ surface potential was almost completely screened by the inherent surface water layer at 40% RH. As it was mentioned earlier, the screening effect is different on different materials. Therefore, such experiments on $LiMn_2O_4$ should be done under controlled conditions, i.e. under vacuum or dry inert atmosphere.

Instead, we observed a significant V_{CPD} drop on the Al current collector of the fatigued samples. This is illustrated in Figure 7.9 where two cathode samples are compared: the fresh 100% SOH 50% SOC sample and the fatigued 78% SOH unchangeable sample. The Al current collector from the fresh sample has uniform $V_{CPD} \approx$ 0.9V, while the one from the fatigued sample has large areas of strongly reduced surface potential.

Origin of this phenomenon is the pitting corrosion of Al in electrolyte (solution of $LiPF_6$ dissolved in dimethyl carbonate (DMC) and ethylene carbonate (EC)). This problem is well known especially in high-voltage Li-ion batteries due to high oxidation potential of the battery discharge. [170,171] Such corrosion can cause additional internal resistance and the consequent capacity drop.

KPFM is proved to be a useful method for local investigation of the Al pitting corrosion [172–174] in addition to conventional electrochemical and structural methods (such as IS, SEM, EDX, etc.) This problem is out of the scope of the present thesis and will be the object of future investigations.
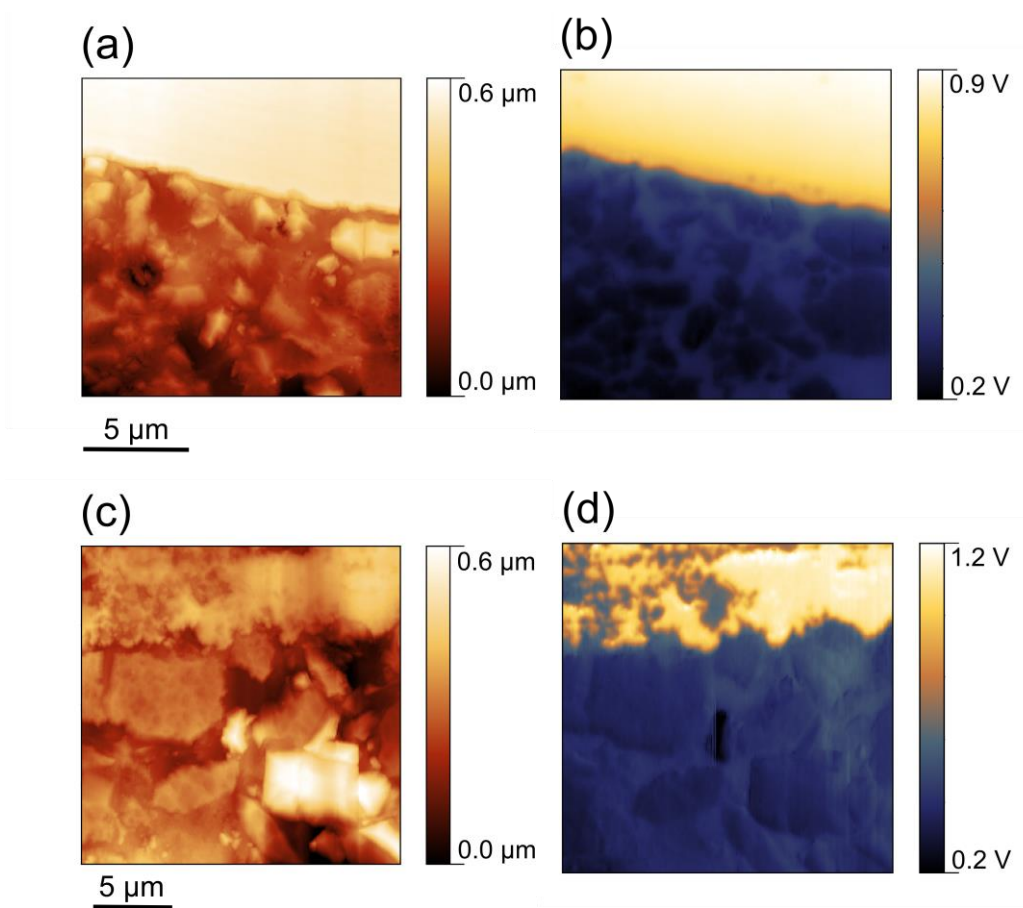
Figure 7.9. Topography (a) and surface potential (b) of the fresh 100% SOH 50% SOC sample; topography (c) and surface potential (d) of the fatigued 78% SOH unchargable sample. The Al current collector of the fatigued sample is severely affected by the pitting corrosion while the one from the fresh sample is not.

Conclusion

In this Chapter, both cathode and anode samples were investigated by means of KPFM. The study revealed the presence of remnant Li after delithiation within the bulk of both fresh and fatigued samples. We found that at 1C-rate small fractions of Li^+ ions can be trapped as domains of Li_xC_6 phase within the pure bulk graphite. After cycling at 16C-rate to 80% SOH and the final discharge at 1C-rate the apparent core-shell structure within the big dense graphite particles was observed in the fatigued anode sample. The core region might thus represent a "dead" volume within which the Li^+ ions are blocked. Besides this, we found that the cracked particles of the same size did not reveal any core-shell structure. The results are the first direct visualization of the radial model that is used to describe the Li intercalation/deintercalation process in polycrystalline anode materials.

Surface potential of the cathode $LiMn_2O_4$ samples was completely screened by the adsorbed water layer under ambient conditions. KPFM study of the $LiMn_2O_4$ samples is

possible under dry inert atmosphere or under vacuum. Instead, the surface potential reduction caused by the severe pitting corrosion was observed on the Al current collector.

The implemented KPFM method can be used to study Li distribution in graphitic anodes at the nanoscale. Being calibrated on a reference sample with known Li concentration, this method can provide quantitative information about Li concentration distribution in a host material at the mesoscale. If implemented under vacuum, it can be used for other Li-intercalation electrode materials.

Chapter 8

Summary

This thesis presents a detailed study of the local Li mobility and concentration in the $LiMn_2O_4$ cathodes and the graphitic anodes of the commercial Li-ion batteries at different states of charge and health by means of ESM and KPFM. It also addresses further development of the recently introduced ESM method.

ESM has been implemented in a single-frequency mode for the first time. The signal-to-noise ratio of the single- and the multi- frequency modes has been analyzed and compared. Signal-to-noise ratio was calculated taking into account different sources of noise in modern AFM systems. It has been shown that the resonance amplification at the single frequency depends on the ratio of the detection system noise to the thermal excitation white noise and can be lower than that predicted by the SHO theory. In case of the multi-frequency detection the resonance amplification can be additionally attenuated due to distribution of the driving power over a number of points in a frequency domain. The analysis allowed establishing criteria for a cantilever and an experimental setup for the most sensitive detection of surface displacements via the lock-in amplifier. According to the presented SNR analysis, the improvement of the sensitivity of the AFM optical detection system is crucial for the performance of ESM method which can be significantly improved in different – multi-frequency and single frequency – regimes.

The investigation of transport properties of Li in $LiMn_2O_4$ revealed that, except of the Vegard contribution, additional non-Vegard contributions are possible. It has been shown that the ESM method cannot be blindly applied to any ion conducting material. Beforehand, material specific properties have to be analyzed in order to reveal possible contributions to the measured signal. This is an essential step for the correct interpretation of experimental results. Voltage spectroscopy measurements showed less uniform distribution of loop opening on the fatigued $LiMn_2O_4$ particles as compared to the fresh ones. The observed change of the loop's shape can indicate a wider variation of the Li diffusion coefficient over the dc voltage cycle on the fatigued sample. Alternatively, it can indicate an additional – non-Vegard – contributions. Moreover, the wider loop opening was observed on the fresh samples with lower lithium concentration. Two possible

explanations were suggested: (i) different Li diffusivity and (ii) saturation of interstitials available for Li within the cubic phase. None of them, however, are totally satisfactory. Time spectroscopy measurements and the consequent quantitative estimations revealed a clear reduction of the Li diffusion coefficient in the fatigued sample at 0% SOC (fully lithiated) as compared to all other samples. This effect was attributed to the structural degradation during 16C-rate cycling and electric field mediated cubic to tetragonal phase transition. Additional contribution of the elastic energy to the diffusion coefficient was estimated. Finally, the question about the true origin of the ESM response was formulated.

KPFM revealed the existence of remnant Li after delithiation within the bulk of both fresh and fatigued anodes. We found that at 1C-rate small fractions of Li^+ ions can be blocked as domains of Li_xC_6 phase within the bulk pure graphite. After cycling at 16C-rate to 80% SOH and the final discharge at 1C-rate the apparent core-shell structure within the big dense graphite particles was observed in the fatigued anode sample. The core region might thus represent a "dead" volume within which the Li^+ ions are blocked. Besides this, we found that the cracked particles of the same size do not reveal any core-shell structure. The results are a direct visualization of the radial model that is used to describe the Li intercalation/deintercalation process in polycrystalline anode materials. Surface potential of the cathode $LiMn_2O_4$ samples was completely screened by the adsorbed water layer under ambient conditions. KPFM study of the $LiMn_2O_4$ samples is possible under dry inert atmosphere or under vacuum. The surface potential reduction caused by the severe pitting corrosion was observed on the Al current collector. The implemented method can be used to observe Li distribution in the graphite anode. Being calibrated on a reference sample with known Li concentration, this method can provide quantitative information about Li concentration in a host material at the mesoscale.

Several questions have emerged during this work.

(i)	The ESM can obtain valuable information, but its quantification is still a difficult task. Taking into account the complex dependence of the Li diffusion coefficient on the Li concentration in battery electrode materials, quantification based solely on the analytical approach can be challenging. Alternatively, the computer modeling seems to be an appropriate method for reasonable quantification.

(ii)	Except of the Vegard contributions, $LiMn_2O_4$ exhibits additional non-Vegard contributions that significantly complicate the correct interpretation of results. Explanation of these contributions would require additional investigations. Being figured out, they could become a valuable source of information about materials properties.

(iii)	The true origin of the ESM response is not fully understood yet. It seems to be the key question that urgently needs to be answered for further development of ESM and its wider application to battery materials.

Bibliography

1.   Park, T.-H. *et al.* Enhancing the rate performance of graphite anodes through addition of natural graphite/carbon nanofibers in lithium-ion batteries. *Electrochim. Acta* **93,** 236–240 (2013).

2.   Nonnenmacher, M., O'Boyle, M. P. & Wickramasinghe, H. K. Kelvin probe force microscopy. *Appl. Phys. Lett.* **58,** 2921 (1991).

3.   Morozovska, A. N., Eliseev, E. A., Balke, N. & Kalinin, S. V. Local probing of ionic diffusion by electrochemical strain microscopy: Spatial resolution and signal formation mechanisms. *J. Appl. Phys.* **108,** 053712 (2010).

4.   Dunn, B., Liu, P. & Meng, S. Nanoscience and nanotechnology in next generation lithium batteries. *Nanotechnology* **24,** 420201 (2013).

5.   Xu, W. *et al.* Lithium metal anodes for rechargeable batteries. *Energy Environ. Sci.* **7,** 513 (2014).

6.   Orsini, F. *et al.* In situ Scanning Electron Microscopy (SEM) observation of interfaces within plastic lithium batteries. *J. Power Sources* **76,** 19–29 (1998).

7.   Park, M., Zhang, X., Chung, M., Less, G. B. & Sastry, A. M. A review of conduction phenomena in Li-ion batteries. *J. Power Sources* **195,** 7904–7929 (2010).

8.   Wu, H. & Cui, Y. Designing nanostructured Si anodes for high energy lithium ion batteries. *Nano Today* **7,** 414–429 (2012).

9.   Yazami, R. & Touzain, P. A reversible graphite-lithium negative electrode for electrochemical generators. *J. Power Sources* **9,** 365–371 (1983).

10.   Landi, B. J., Ganter, M. J., Cress, C. D., DiLeo, R. a. & Raffaelle, R. P. Carbon nanotubes for lithium ion batteries. *Energy Environ. Sci.* **2,** 638 (2009).

11.   Goodenough, J. B. & Park, K. S. The Li-ion rechargeable battery: A perspective. *J. Am. Chem. Soc.* **135,** 1167–1176 (2013).

12.   Goodenough, J. B., Manthiram, A. & Wnetrzewski, B. Electrodes for lithium batteries. *J. Power Sources* **43,** 269–275 (1993).

13.   Brodd, R. J. *Batteries for Sustainability*. (Springer New York, 2013). at <http://link.springer.com/10.1007/978-1-4614-5791-6>

14.   Van der Ven, A., Bhattacharya, J. & Belak, A. A. Understanding Li diffusion in Li-intercalation compounds. *Acc. Chem. Res.* **46,** 1216–1225 (2013).

15. Chung, D. D. L. Review Graphite. *J. Mater. Sci.* **37,** 1475–1489 (2002).

16. Harris, S. J., Timmons, A., Baker, D. R. & Monroe, C. Direct in situ measurements of Li transport in Li-ion battery negative electrodes. *Chem. Phys. Lett.* **485,** 265–274 (2010).

17. Funabiki, A., Inaba, M., Abe, T. & Ogumi, Z. Influence of defects on the phase-boundary movement in a stage transformation of lithium-graphite intercalation compounds. *Carbon* **37,** 1591–1598 (1999).

18. Safran, S. & Hamann, D. Long-range elastic interactions and staging in graphite intercalation compounds. *Phys. Rev. Lett.* **42,** 1410–1413 (1979).

19. Sethuraman, V. A., Hardwick, L. J., Srinivasan, V. & Kostecki, R. Surface structural disordering in graphite upon lithium intercalation/deintercalation. *J. Power Sources* **195,** 3655–3660 (2010).

20. Lauginie, P. *et al.* Graphite lamellar compounds EPR studies. *Phys. B+C* **99,** 514–520 (1980).

21. Dahn, J. Phase diagram of Li_xC_6. *Phys. Rev. B* **44,** 9170–9177 (1991).

22. Whitehead, A. H., Edström, K., Rao, N. & Owen, J. R. In situ X-ray diffraction studies of a graphite-based Li-ion battery negative electrode. *J. Power Sources* **63,** 41–45 (1996).

23. Billaud, D., Henry, F. X. & Willmann, P. Electrochemical synthesis of binary graphite-lithium intercalation compounds. *Mater. Res. Bull.* **28,** 477–483 (1993).

24. Persson, K., Hinuma, Y., Meng, Y. S., Van der Ven, A. & Ceder, G. Thermodynamic and kinetic properties of the Li-graphite system from first-principles calculations. *Phys. Rev. B* **82,** 125416 (2010).

25. Imai, Y. & Watanabe, A. Energetic evaluation of possible stacking structures of Li-intercalation in graphite using a first-principle pseudopotential calculation. *J. Alloys Compd.* **439,** 258–267 (2007).

26. Zhang, S. S., Xu, K. & Jow, T. R. Low temperature performance of graphite electrode in Li-ion cells. *Electrochim. Acta* **48,** 241–246 (2002).

27. Funabiki, A. *et al.* Impedance study on the electrochemical lithium intercalation into natural graphite powder. *J. Electrochem. Soc.* **145,** 172–178 (1998).

28. Lyakishev, P. N. *Phase diagrams of binary metallic systems*. (Mashinostroenie, 1996). (in Russian)

29. Nie, M. *et al.* Lithium ion battery graphite solid electrolyte interphase revealed by microscopy and spectroscopy. *J. Phys. Chem. C* **117,** 1257–1267 (2013).

30. Zhang, S. S. The effect of the charging protocol on the cycle life of a Li-ion battery. *J. Power Sources* **161,** 1385–1391 (2006).

31. Agubra, V. & Fergus, J. Lithium ion battery anode aging mechanisms. *Materials (Basel).* **6,** 1310–1325 (2013).

32. Yoshio, M. *et al.* Improvement of natural graphite as a lithium-ion battery anode material, from raw flake to carbon-coated sphere. *J. Mater. Chem.* **14,** 1754–1758 (2004).

33. Buqa, H. *et al.* Negative electrodes in rechargeable lithium ion batteries — Influence of graphite surface modification on the formation of the solid electrolyte interphase. *Ionics (Kiel).* **6,** 172–179 (2000).

34. Picot, M., Lapinsonnière, L., Rothballer, M. & Barrière, F. Graphite anode surface modification with controlled reduction of specific aryl diazonium salts for improved microbial fuel cells power output. *Biosens. Bioelectron.* **28,** 181–188 (2011).

35. Park, M.-S. *et al.* Incorporation of phosphorus into the surface of natural graphite anode for lithium ion batteries. *J. Mater. Chem.* **21,** 17960–17966 (2011).

36. Xia, Y. An investigation of lithium ion insertion into spinel structure Li-Mn-O compounds. *Journal of The Electrochemical Society* **143,** 825–833 (1996).

37. Berg, H., Göransson, K., Noläng, B. & Thomas, J. O. Electronic structure and stability of the $Li_xMn_2O_4$ (0<x<2) system. *J. Mater. Chem.* **9,** 2813–2820 (1999).

38. Ishizawa, N. & Tateishi, K. Diffusion of Li atoms in $LiMn_2O_4$ – A structural point of view. *J. Ceram. Soc. Japan* **117,** 6–14 (2009).

39. Saïdi, M., Barker, J. & Koksbang, R. Thermodynamic and kinetic investigation of lithium insertion in the $Li_{1-x}Mn_2O_4$ spinel phase. *J. Solid State Chem.* **122,** 195–199 (1996).

40. Iguchi, E., Tokuda, Y., Nakatsugawa, H. & Munakata, F. Electrical transport properties in $LiMn_2O_4$, $Li_{0.95}Mn_2O_4$, and $LiMn_{1.95}B_{0.05}O_4$ (B=Al or Ga) around room temperature. *J. Appl. Phys.* **91,** 2149 (2002).

41. Shimakawa, Y., Numata, T. & Tabuchi, J. Verwey-type transition and magnetic properties of the $LiMn_2O_4$ spinels. *J. Solid State Chem.* **131,** 138–143 (1997).

42. Yamamura, S., Koshika, H., Nishizawa, M., Matsue, T. & Uchida, I. In situ conductivity measurements of $LiMn_2O_4$ thin films during lithium insertion/extraction by using interdigitated microarray electrodes. *J. Solid State Electrochem.* **2,** 211–215 (1998).

43. Guan, J. & Liu, M. Transport properties of $LiMn_2O_4$ electrode materials for lithium-ion batteries. *Solid State Ionics* **110,** 21–28 (1998).

44. Mukerjee, S. *et al.* Structural evolution of $Li_xMn_2O_4$ in lithium-ion battery cells measured in situ using synchrotron X-Ray diffraction techniques. *J. Electrochem. Soc.* **145,** 466–472 (1998).

45. Hunter, J. C. Preparation of a new crystal form of manganese dioxide: λ-MnO_2. *J. Solid State Chem.* **39,** 142–147 (1981).

46. Thackeray, M. M. Manganese oxides for lithium batteries. *Prog. Solid State Chem.* **25,** 1–71 (1997).

47. Gummow, R. J., de Kock, A. & Thackeray, M. M. Improved capacity retention in rechargeable 4 V lithium/lithium-manganese oxide (spinel) cells. *Solid State Ionics* **69,** 59–67 (1994).

48. Ohzuku, T., Kitagawa, M. & Hirai, T. Electrochemistry of manganese dioxide in lithium nonaqueous cell III . X-Ray diffractional study on the reduction of spinel-related manganese dioxide. *J. Electrochem. Soc.* **137,** 769–775 (1990).

49. Verhoeven, V. W. J. *et al.* Lithium dynamics in $LiMn_2O_4$ probed directly by two-dimensional 7Li NMR. *Phys. Rev. Lett.* **86,** 4314–4317 (2001).

50. Sharma, N., Yu, D., Zhu, Y., Wu, Y. & Peterson, V. K. Non-equilibrium structural evolution of the lithium-rich $Li_{1+y}Mn_2O_4$ cathode within a battery. *Chem. Mater.* (2013).

51. Hartley, G. S. Diffusion and distribution in a solvent of graded composition. *Trans. Faraday Soc.* **27,** 10–29 (1931).

52. Darken, L. S. Diffusion of carbon in austenite with a discontinuity in composition. *Trans. AIME* **180,** 430–438 (1949).

53. Chung, M. D., Seo, J. H., Zhang, X. C. & Sastry, A. M. Implementing realistic geometry and measured diffusion coefficients into single particle electrode modeling based on experiments with single $LiMn_2O_4$ spinel particles. *J. Electrochem. Soc.* **158,** A371–A378 (2011).

54. Dokko, K. *et al.* Electrochemical studies of Li-ion extraction and insertion of $LiMn_2O_4$ single crystal. *Electrochem. Solid-State Lett.* **4,** A151–A153 (2001).

55. Shewmon, P. *Diffusion in Solids*. (Wiley, 1989).

56. Molenda, J. Influence of host electronic structure on lithium intercalation process. *Solid State Ionics* **175,** 203–213 (2004).

57. Tateishi, K., Du Boulay, D. & Ishizawa, N. The effect of mixed Mn valences on Li migration in $LiMn_2O_4$ spinel: a molecular dynamics study. *Appl. Phys. Lett.* **84,** 529–531 (2004).

58.   Stoneham, A. M. Non- classical diffusion processes. *J. Nucl. Mater.* **69-70,** 109–116 (1978).

59.   Iguchi, E., Nakamura, N. & Aoki, A. Electrical transport properties in $LiMn_2O_4$. *Philos. Mag. Part B* **78,** 65–77 (2009).

60.   Barker, J., Pynenburg, R. & Koksbang, R. Determination of thermodynamic, kinetic and interfacial properties for the $Li//Li_xMn_2O_4$ system by electrochemical techniques. *J. Power Sources* **52,** 185–192 (1994).

61.   Tarascon, J. M., Coowar, F., Amatuci, G., Shokoohi, F. K. & Guyomard, D. G. The $Li_{1+x}Mn_2O_4C$ system materials and electrochemical aspects. *J. Power Sources* **54,** 103–108 (1995).

62.   Pieczonka, N. P. W. *et al.* Understanding transition-metal dissolution behavior in $LiNi_{0.5}Mn_{1.5}O_4$ high-voltage spinel for lithium ion batteries. *J. Phys. Chem. C* **117,** 15947–15957 (2013).

63.   Woodford, W. H., Chiang, Y.-M. & Carter, W. C. 'Electrochemical Shock' of intercalation electrodes: a fracture mechanics analysis. *J. Electrochem. Soc.* **157,** A1052–A1059 (2010).

64.   Zhao, K., Pharr, M., Vlassak, J. J. & Suo, Z. Fracture of electrodes in lithium-ion batteries caused by fast charging. *J. Appl. Phys.* **108,** 073517 (2010).

65.   Shao-Horn, Y. *et al.* Structural fatigue in spinel electrodes in $Li/Li_x[Mn_2]O_4$ cells. *J. Power Sources* **81-82,** 496–499 (1999).

66.   Xia, H., Luo, Z. & Xie, J. Nanostructured $LiMn_2O_4$ and their composites as high-performance cathodes for lithium-ion batteries. *Prog. Nat. Sci. Mater. Int.* **22,** 572–584 (2012).

67.   Xia, Y., Zhou, Y. & Yoshio, M. Capacity fading on cycling of 4 V $Li/LiMn_2O_4$ cells. *J. Electrochem. Soc.* **144,** 2593–2600 (1997).

68.   Kim, D. *et al.* Re-deposition of manganese species on spinel $LiMn_2O_4$ electrode after Mn dissolution. *J. Electrochem. Soc.* **159,** A193–A197 (2012).

69.   Lee, J. H. & Kim, K. J. Superior electrochemical properties of porous Mn_2O_3-coated $LiMn_2O_4$ thin-film cathodes for Li-ion microbatteries. *Electrochim. Acta* **102,** 196–201 (2013).

70.   Wang, H.-C. & Lu, C.-H. Dissolution behavior of chromium-ion doped spinel lithium manganate at elevated temperatures. *J. Power Sources* **119-121,** 738–742 (2003).

71.   Park, Y. *et al.* Electrochemical properties of $LiMn_2O_4$ thin films: suggestion of factors for excellent rechargeability. *J. Power Sources* **87,** 69–77 (2000).

72. Li, X., Xu, Y. & Wang, C. Suppression of Jahn-Teller distortion of spinel $LiMn_2O_4$ cathode. *J. Alloys Compd.* **479,** 310–313 (2009).

73. Wen, C. J., Boukamp, B. A., Huggins, R. A. & Weppner, W. Thermodynamic and mass transport properties of 'LiAl'. *J. Electrochem. Soc.* **126,** 2258–2266 (1979).

74. Weppner, W. & Huggins, R. A. Electrochemical methods for determining kinetic properties of solids. *Annu. Rev. Mater. Sci.* **8,** 269–311 (1978).

75. Dawn A Bonnell & Kalinin, S. V. *Scanning probe microscopy for energy research.* (Worldscientific, 2013). at <http://www.worldscientific.com/worldscibooks/10.1142/8613>

76. Kalinin, S. V. & Balke, N. Local electrochemical functionality in energy storage materials and devices by scanning probe microscopies: status and perspectives. *Adv. Mater.* **22,** E193–E209 (2010).

77. Nagpure, S. C., Bhushan, B. & Babu, S. S. Surface potential measurement of aged Li-ion batteries using Kelvin probe microscopy. *J. Power Sources* **196,** 1508–1512 (2011).

78. Glatzel, T., Sadewasser, S., Shikler, R., Rosenwaks, Y. & Lux-Steiner, M. C. Kelvin probe force microscopy on III–V semiconductors: the effect of surface defects on the local work function. *Mater. Sci. Eng. B* **102,** 138–142 (2003).

79. Melitz, W., Shen, J., Kummel, A. C. & Lee, S. Kelvin probe force microscopy and its application. *Surf. Sci. Rep.* **66,** 1–27 (2011).

80. Zhu, J., Zeng, K. & Lu, L. In-situ nanoscale mapping of surface potential in all-solid-state thin film Li-ion battery using Kelvin probe force microscopy. *J. Appl. Phys.* **111,** 063723 (2012).

81. Kawano, H. Effective work functions for ionic and electronic emissions from mono- and polycrystalline surfaces. *Prog. Surf. Sci.* **83,** 1–165 (2008).

82. Hudlet, S., Saint Jean, M., Roulet, B., Berger, J. & Guthmann, C. Electrostatic forces between metallic tip and semiconductor surfaces. *J. Appl. Phys.* **77,** 3308–3314 (1995).

83. Glatzel, T., Sadewasser, S. & Lux-Steiner, M. C. Amplitude or frequency modulation-detection in Kelvin probe force microscopy. *Appl. Surf. Sci.* **210,** 84–89 (2003).

84. Zerweck, U., Loppacher, C., Otto, T., Grafström, S. & Eng, L. Accuracy and resolution limits of Kelvin probe force microscopy. *Phys. Rev. B* **71,** 125424 (2005).

85. Kawai, S., Glatzel, T., Hug, H.-J. & Meyer, E. Atomic contact potential variations of Si(111)-7 x 7 analyzed by Kelvin probe force microscopy. *Nanotechnology* **21,** 245704 (2010).

86. Panchal, V., Pearce, R., Yakimova, R., Tzalenchuk, A. & Kazakova, O. Standardization of surface potential measurements of graphene domains. *Sci. Rep.* **3,** 2597 (2013).

87. Elias, G. *et al.* The role of the cantilever in Kelvin probe force: microscopy measurements. *Beilstein J. Nanotechnol.* **2,** 252–260 (2011).

88. Jesse, S. *et al.* Electrochemical strain microscopy: probing ionic and electrochemical phenomena in solids at the nanometer level. *MRS Bull.* **37,** 651–658 (2012).

89. Morozovska, A. N. *et al.* Frequency dependent dynamical electromechanical response of mixed ionic-electronic conductors. *J. Appl. Phys.* **111,** 014107 (2012).

90. Tselev, A., Morozovska, A. N., Udod, A., Eliseev, E. A. & Kalinin, S. V. Self-consistent modeling of electrochemical strain microscopy of solid electrolytes. *Nanotechnology* **25,** 445701 (2014).

91. Amanieu, H.-Y. *et al.* Electrochemical strain microscopy time spectroscopy: model and experiment on LiMn$_2$O$_4$. *Submitt. to J. Appl. Phys.* (2015).

92. Darken, L. S. & Gurry, R. W. *Physical chemistry of metals*. (McGraw-Hill, 1953).

93. Landau, L. D., Pitaevskii, L. P., Kosevich, A. M. & Lifshitz, E. M. *Theory of elasticity*. (Butterworth-Heinemann, 1986).

94. Morozovska, A. N., Eliseev, E. A. & Kalinin, S. V. Electromechanical probing of ionic currents in energy storage materials. *Appl. Phys. Lett.* **96,** 222906 (2010).

95. Kalinin, S. V. & Morozovska, A. N. Electrochemical strain microscopy of local electrochemical processes in solids: mechanism of imaging and spectroscopy in the diffusion limit. *J. Electroceramics* **32,** 51–59 (2013).

96. Jesse, S. *et al.* Direct mapping of ionic transport in a Si anode on the nanoscale: Time domain electrochemical strain spectroscopy study. *ACS Nano* **5,** 9682–9695 (2011).

97. Gellings, P. J. & Bouwmeester, H. J. *Handbook of solid state electrochemistry*. (CRC Press, 1997).

98. Kalinin, S. *et al.* Li-ion dynamics and reactivity on the nanoscale. *Mater. Today* **14,** 548–558 (2011).

99. Teschke, O. & de Souza, E. F. Electrostatic response of hydrophobic surface measured by atomic force microscopy. *Appl. Phys. Lett.* **82,** 1126 (2003).

100. Guo, S. *et al.* Direct mapping of ion diffusion times on $LiCoO_2$ surfaces with nanometer resolution. *J. Electrochem. Soc.* **158,** A982–A990 (2011).

101. Kumar, A., Ciucci, F., Morozovska, A. N., Kalinin, S. V & Jesse, S. Measuring oxygen reduction/evolution reactions on the nanoscale. *Nat. Chem.* **3,** 707–713 (2011).

102. Kim, Y. *et al.* Ionically-mediated electromechanical hysteresis in transition metal oxides. *ACS Nano* **6,** 7026–7033 (2012).

103. Hong, S. *et al.* Principle of ferroelectric domain imaging using atomic force microscope. *J. Appl. Phys.* **89,** 1377–1386 (2001).

104. Balke, N. *et al.* Decoupling electrochemical reaction and diffusion processes in ionically-conductive solids on the nanometer scale. *ACS Nano* **4,** 7349–7357 (2010).

105. Kochervinskii, V. V. Piezoelectricity in crystallizing ferroelectric polymers: Poly(vinylidene fluoride) and its copolymers (a review). *Crystallogr. Reports* **48,** 649–675 (2003).

106. Chen, Q. N., Ou, Y., Ma, F. & Li, J. Mechanisms of electromechanical coupling in strain based scanning probe microscopy. *Appl. Phys. Lett.* **104,** 242907 (2014).

107. Harnagea, C., Pignolet, A., Alexe, M. & Hesse, D. Higher-order electromechanical response of piezoresponse force microscopy. *IEEE Trans. Ultrason. Ferroelectr. Freq. Control* **53,** 2309–2322 (2006).

108. Morozovska, A. N., Eliseev, E. A. & Kalinin, S. V. Electrochemical strain microscopy with blocking electrodes: the role of electromigration and diffusion. *J. Appl. Phys.* **111,** 014114 (2012).

109. Luchkin, S. Y., Amanieu, H.-Y., Rosato, D. & Kholkin, A. L. Li distribution in graphite anodes: a Kelvin probe force microscopy approach. *J. Power Sources* **268,** 887–894 (2014).

110. Atomic Force Microscope NEXT. at <http://www.ntmdt.com/automated-afm/atomic-force-microscope-next>

111. Garcia, R. & Herruzo, E. T. The emergence of multifrequency force microscopy. *Nat. Nanotechnol.* **7,** 217–226 (2012).

112. Jesse, S., Kalinin, S. V., Proksch, R., Baddorf, A. P. & Rodriguez, B. J. The band excitation method in scanning probe microscopy for rapid mapping of energy dissipation on the nanoscale. *Nanotechnology* **18,** 435503 (2007).

113. Rodriguez, B. J., Callahan, C., Kalinin, S. V. & Proksch, R. Dual-frequency resonance-tracking atomic force microscopy. *Nanotechnology* **18,** 475504 (2007).

114. Romanyuk, K., Luchkin, S. Y., Ivanov, M., Kalinin, A. & Kholkin, A. L. Single- and multi-frequency detection of surface displacements via scanning probe microscopy. *Microsc. Microanal.* **21,** 154–163 (2015).

115. Lübbe, J. *et al.* Thermal noise limit for ultra-high vacuum noncontact atomic force microscopy. *Beilstein J. Nanotechnol.* **4,** 32–44 (2013).

116. Hutter, J. L. & Bechhoefer, J. Calibration of atomic-force microscope tips. *Rev. Sci. Instrum.* **64,** 1868 (1993).

117. Butt, H.-J. & Jaschke, M. Calculation of thermal noise in atomic force microscopy. *Nanotechnology* **6,** 1–7 (1995).

118. Walters, D. a. *et al.* Short cantilevers for atomic force microscopy. *Rev. Sci. Instrum.* **67,** 3583 (1996).

119. Rast, S., Wattinger, C., Gysin, U. & Meyer, E. The noise of cantilevers. *Nanotechnology* **11,** 169–172 (2000).

120. Kopycinska-Müller, M., Geiss, R. H. & Hurley, D. C. Contact mechanics and tip shape in AFM-based nanomechanical measurements. *Ultramicroscopy* **106,** 466–474 (2006).

121. Han, W. & Lindsay, S. M. *Intrinsic contact noise: application note. Agilent Technologies* (2007).

122. Jesse, S. & Kalinin, S. V. Band excitation in scanning probe microscopy: sines of change. *Journal of Physics D: Applied Physics* **44,** 464006 (2011).

123. Kos, A. B. & Hurley, D. C. Nanomechanical mapping with resonance tracking scanned probe microscope. *Meas. Sci. Technol.* **19,** 015504 (2008).

124. Rodriguez, B. J., Jesse, S., Habelitz, S., Proksch, R. & Kalinin, S. V. Intermittent contact mode piezoresponse force microscopy in a liquid environment. *Nanotechnology* **20,** 195701 (2009).

125. Fukuma, T., Kimura, M., Kobayashi, K., Matsushige, K. & Yamada, H. Development of low noise cantilever deflection sensor for multienvironment frequency-modulation atomic force microscopy. *Rev. Sci. Instrum.* **76,** 053704 (2005).

126. Balke, N. *et al.* Nanoscale mapping of ion diffusion in a lithium-ion battery cathode. *Nat. Nanotechnol.* **5,** 749–754 (2010).

127. Nataly Chen, Q. *et al.* Delineating local electromigration for nanoscale probing of lithium ion intercalation and extraction by electrochemical strain microscopy. *Appl. Phys. Lett.* **101,** 063901 (2012).

128. Kumar, A. *et al.* Nanometer-scale mapping of irreversible electrochemical nucleation processes on solid Li-ion electrolytes. *Sci. Rep.* **3,** 1621 (2013).

129. Amanieu, H.-Y. *et al.* Mechanical properties of commercial $Li_xMn_2O_4$ cathode under different states of charge. *Acta Mater.* **89,** 153–162 (2015).

130. Kuriyama, K., Onoue, A., Yuasa, Y. & Kushida, K. Atomic force microscopy study of surface morphology change in spinel $LiMn_2O_4$: possibility of direct observation of Jahn-Teller instability. *Surf. Sci.* **601,** 2256–2259 (2007).

131. Hoang, K. Understanding the electronic and ionic conduction and lithium over-stoichiometry in $LiMn_2O_4$ spinel. *J. Mater. Chem. A* **2,** 18271–18280 (2014).

132. Mamin, R. F., Bdikin, I. K. & Kholkin, A. L. Locally induced charged states in $La_{0.89}Sr_{0.11}MnO_3$ single crystals. *Appl. Phys. Lett.* **94,** 222901 (2009).

133. Firsov, Y. A. *Polarons*. (Nauka, 1975). (in Russian)

134. Li, Q. *et al.* Switching spectroscopic measurement of surface potentials on ferroelectric surfaces via an open-loop Kelvin probe force microscopy method. *Appl. Phys. Lett.* **101,** 242906 (2012).

135. Jooss, C. *et al.* Polaron melting and ordering as key mechanisms for colossal resistance effects in manganites. *Proc. Natl. Acad. Sci. U. S. A.* **104,** 13597–13602 (2007).

136. Figueiras, F. G. N., Bdikin, I. K., Amaral, V. B. S. & Kholkin, A. L. Local bias induced ferroelectricity in manganites with competing charge and orbital order states. *Phys. Chem. Chem. Phys.* **16,** 4977–4981 (2014).

137. Sekhon, J. S., Aggarwal, L. & Sheet, G. Voltage induced local hysteretic phase switching in silicon. *Appl. Phys. Lett.* **104,** 162908 (2014).

138. Balke, N. *et al.* Real space mapping of Li-ion transport in amorphous Si anodes with nanometer resolution. *Nano Lett.* **10,** 3420–3425 (2010).

139. Proksch, R. Electrochemical strain microscopy of silica glasses. *J. Appl. Phys.* **116,** 066804 (2014).

140. Newnham, R. E., Sundar, V., Yimnirun, R., Su, J. & Zhang, Q. M. Electrostriction: nonlinear electromechanical coupling in solid dielectrics. *J. Phys. Chem. B* **101,** 10141–10150 (1997).

141. Yang, S. M. *et al.* Second harmonic detection in the electrochemical strain microscopy of Ag-ion conducting glass. *Appl. Phys. Lett.* **105,** 193106 (2014).

142. Knorr, N., Rosselli, S., Miteva, T. & Nelles, G. Biased-probe-induced water ion injection into amorphous polymers investigated by electric force microscopy. *J. Appl. Phys.* **105,** 114111 (2009).

143. Barrer, M. R. *Diffusion in and through solids*. (Cambridge, England : The University Press ; New York : Macmillan, 1941).

144. Denhoff, M. W. An accurate calculation of spreading resistance. *J. Phys. D. Appl. Phys.* **39,** 1761–1765 (2006).

145. Nowick, A. S. & Berry, B. S. *Anelastic relaxation in crystalline solids*. (Academic press, 1972).

146. Zhang, X., Shyy, W. & Marie Sastry, A. Numerical simulation of intercalation-induced stress in Li-ion battery electrode particles. *J. Electrochem. Soc.* **154,** A910–A916 (2007).

147. Kanamura, K., Naito, H., Yao, T. & Takehara, Z. Structural change of the $LiMn_2O_4$ spinel structure induced by extraction of lithium. *J. Mater. Chem.* **6,** 33–36 (1996).

148. Chung, K. Y. & Kim, K. B. Investigations into capacity fading as a result of a Jahn-Teller distortion in 4 V $LiMn_2O_4$ thin film electrodes. *Electrochim. Acta* **49,** 3327–3337 (2004).

149. Das, S. R., Majumder, S. B. & Katiyar, R. S. Kinetic analysis of the Li^+ ion intercalation behavior of solution derived nano-crystalline lithium manganate thin films. *J. Power Sources* **139,** 261–268 (2005).

150. Wu, X., Li, R., Chen, S. & He, Z. Synthesis and characterization of $Li_{1.3}Al_{0.3}Ti_{1.7}(PO_4)_3$-coated $LiMn_2O_4$ by wet chemical route. *Rare Met.* **28,** 122–126 (2009).

151. Charles Kittel. *Introduction to solid state physics*. (Wiley, 1971).

152. Brown, W. D., Hess, D., Desai, V. & Deen, M. J. Electrochemistry encyclopedia - dielectrics. (2006). at <http://knowledge.electrochem.org/encycl/art-d01-dielectrics.htm>

153. Bohn, E., Eckl, T., Kamlah, M. & McMeeking, R. A Model for lithium diffusion and stress generation in an intercalation storage particle with phase change. *J. Electrochem. Soc.* **160,** A1638–A1652 (2013).

154. Bluhm, H., Inoue, T. & Salmeron, M. Formation of dipole-oriented water films on mica substrates at ambient conditions. *Surf. Sci.* **462,** L599–L602 (2000).

155. Jacobs, H. O., Knapp, H. F. & Stemmer, A. Practical aspects of Kelvin probe force microscopy. *Rev. Sci. Instrum.* **70,** 1756 (1999).

156. Zaghloul, U. *et al.* On the influence of environment gases, relative humidity and gas purification on dielectric charging/discharging processes in electrostatically driven MEMS/NEMS devices. *Nanotechnology* **22,** 035705 (2011).

157. Hansen, W. N., Hansen, W. N., Hansen, G. J. & Hansen, G. J. Standard reference surfaces for work function measurements in air. *Surf. Sci.* **481,** 172–184 (2001).

158. Ono, S., Takeuchi, M. & Takahashi, T. Kelvin probe force microscopy on InAs thin films grown on GaAs giant step structures formed on (110) GaAs vicinal substrates. *Appl. Phys. Lett.* **78,** 1086 (2001).

159. Przychowski, M. D., Marx, G. K., Fecher, G. & Schönhense, G. A spatially resolved investigation of oxygen adsorption on polycrystalline copper and titanium by means of photoemission electron microscopy. *Surf. Sci.* **549,** 37–51 (2004).

160. Obraztsov, A. N., Volkov, A. P., Boronin, A. I. & Kosheev, S. V. Defect induced lowering of work function in graphite-like materials. *Diam. Relat. Mater.* **11,** 813–818 (2002).

161. Baturin, A. S., Nikolski, K. N., Knyazev, A. I., Tchesov, R. G. & Sheshin, E. P. Doping of graphite by an alkaline-earth metal to reduce the work function. *Tech. Phys.* **49,** 342–344 (2004).

162. Lee, H. *et al.* Strong interfacial dipole formation with thermal evaporation of lithium cobalt oxide for efficient electron injections. *Appl. Phys. Lett.* **102,** 033302 (2013).

163. Xie, K. *et al.* Formation, confirmation and application of Li : Al alloy as an electron injection layer with Li_3N as the precursor. *J. Phys. D. Appl. Phys.* **43,** 252001 (2010).

164. Mizuno, S. *et al.* Formation of a linear LiOH compound on Cu(001): reaction of H_2O with Li adatoms at low coverages. *Surf. Sci.* **264,** 103–113 (1992).

165. Ning, G., Haran, B. & Popov, B. N. Capacity fade study of lithium-ion batteries cycled at high discharge rates. *J. Power Sources* **117,** 160–169 (2003).

166. Gnanaraj, J. S. *et al.* Comparison between the electrochemical behavior of disordered carbons and graphite electrodes in connection with their structure. *J. Electrochem. Soc.* **148,** A525–A536 (2001).

167. Qi, Y., Guo, H., Hector, L. G. & Timmons, A. Threefold increase in the Young's modulus of graphite negative electrode during lithium intercalation. *J. Electrochem. Soc.* **157,** A558–A566 (2010).

168. Andersson, A. . & Thomas, J. . The source of first-cycle capacity loss in $LiFePO_4$. *J. Power Sources* **97-98,** 498–502 (2001).

169. Aydinol, M. K. First-principles prediction of insertion potentials in Li-Mn oxides for secondary Li batteries. *J. Electrochem. Soc.* **144,** 3832–3835 (1997).

170. Braithwaite, J. W. Corrosion of lithium-ion battery current collectors. *J. Electrochem. Soc.* **146,** 448–456 (1999).

171. Myung, S.-T., Hitoshi, Y. & Sun, Y.-K. Electrochemical behavior and passivation of current collectors in lithium-ion batteries. *J. Mater. Chem.* **21,** 9891–9911 (2011).

172. Muster, T. H. & Hughes, A. E. Applications and limitations of scanning Kelvin Probe force microscopy for the surface analysis of aluminum alloys. *J. Electrochem. Soc.* **153,** B474–B485 (2006).

173. Larignon, C. *et al.* Combined Kelvin probe force microscopy and secondary ion mass spectrometry for hydrogen detection in corroded 2024 aluminium alloy. *Electrochim. Acta* **110,** 484–490 (2013).

174. Larignon, C. *et al.* Investigation of Kelvin probe force microscopy efficiency for the detection of hydrogen ingress by cathodic charging in an aluminium alloy. *Scr. Mater.* **68,** 479–482 (2013).

Publications

1. S. Yu. Luchkin, H.-Y. Amanieu, D. Rosato, A.L. Kholkin, Li distribution in graphite anodes: A Kelvin Probe Force Microscopy approach, *J. Power Sources* **268,** 887–894 (2014)

2. K. Romanyuk, S.Yu. Luchkin, M. Ivanov, A. Kalinin, A.L. Kholkin, Signal-to-noise ratio of single- and multi-frequency detection of surface displacements via Scanning Probe Microscopy, *Microsc. Microanal.* **21,** 154–163 (2015).

3. Sergey Yu. Luchkin, Konstantin Romanyuk, Maxim Ivanov, Andrei L. Kholkin, Li transport in fresh and aged $LiMn_2O_4$ cathodes via Electrochemical Strain Microscopy, accepted for publication in Journal of Applied Physics

4. Gonçalo da Cunha Rodrigues, Pavel Zelenovskiy, Konstantin Romanyuk, Sergey Luchkin, Ya. Kopelevich, Andrei Kholkin, Strong piezoelectricity in single-layer graphene deposited on SiO_2 grating substrates, accepted for publication in Nature Communications

5. Hugues-Yanis Amanieu, Huy N.M. Thai, Sergey Yu Luchkin, Daniele Rosato, Doru C. Lupascu, Marc-André Keip, Jörg Schröder, Andrei Kholkin, Electrochemical Strain Microscopy Time Spectroscopy: model and experiment on $LiMn_2O_4$, submitted to Journal of Applied Physics

Conferences and Workshops

1. <u>S. Luchkin</u>, A. Kholkin, Li-diffusion in Li-ion battery materials, ITN internal meeting, Aveiro, Portugal, 08 July – 09 July 2012. Oral presentation.

2. <u>S. Luchkin</u>, A. Kholkin, Electrochemical Strain Microscopy of Li battery materials, Oak-Ridge, TN, USA, 4 March – 8 March 2013. Oral presentation.

3. <u>S. Luchkin</u>, A. Kholkin, Li concentration and diffusion in commercial $LiMn_2O_4$ cathodes via Electrochemical Strain Microscopy, 7th International Conference on Materials for Advanced Technologies (ICMAT 2013), Singapore, 30 June – 5 July 2013. Oral presentation.

4. <u>S. Luchkin</u>, K. Romanyuk, A. Kholkin, Nanoscale study of V_2O_5-graphene composites via Scanning Probe Microscopy, Research Day, Aveiro, Portugal, 19 July 2013. Poster.

5. <u>S. Luchkin</u>, A. Kholkin, N. Balke, Li diffusion and electrochemical activity in commercial $LiMn_2O_4$ battery cathode by Electrochemical Strain Microscopy, 2013 Joint UffC, EFTF and PFM Symposium, Prague, Czech Republic, 21 July – 25 July 2013. Poster.

6. <u>S. Luchkin</u>, A. Kholkin, Li-diffusion in Li-ion battery materials, NANOMOTION meeting, Prague, Czech Republic, 26 July 2013.

7. D.O. Alikin, A.V. Ievlev, A.P. Turigin, D.V. Pelegov, <u>S. Luchkin</u>, V.Ya. Shur, S. Kalinin, A.L. Kholkin, Band-excitation Electrochemical Strain Microscopy of the Commercial $LiMn_2O_4$ Battery Material, 2014 Joint IEEE International Symposium on the Applications of Ferroelectrics, International Workshop on Acoustic Transduction Materials and Devices, Workshop on Piezoresponse Force Microscopy ISAF – IWATMD – PFM, PA, USA, 13 May - 16 May 2014. Not present.

8. <u>S. Luchkin</u>, K. Romanyuk, M. Ivanov, A. Kholkin, Application of ESM method to Li battery materials, Research Day, Aveiro, Portugal, 03 June 2014. Poster.

9. D.O. Alikin, A.P. Turygin, D.V. Pelegov, A.D. Ushakov, F. Figueiredo, <u>S. Luchkin</u>, V.Ya. Shur, A.L.Kholkin, Electrochemical strain microscopy in the bulk ceramics of the oxygen ion-conductors, International Conference PFM-2014, Ekaterinburg, Russia, 14 July - 17 July, 2014. Not present.

10. D.O. Alikin, <u>S. Luchkin</u>, A.V. Ievlev, A.P. Turygin, D.V. Pelegov, V.Ya. Shur, S. Kalinin, A.L. Kholkin, Local electrochemical spectroscopy of the Commercial Battery Materials, International Conference PFM-2014, Ekaterinburg, Russia, 14 July - 17 July, 2014. Not present.

11. <u>S. Luchkin</u>, K. Romanyuk, M. Ivanov, A. Kholkin, KPFM and ESM for studying Li diffusion and concentration in Li batteries, International conference Materials

Science and Engineering, Darmstadt, Germany, 23 September – 25 September 2014. Oral presentation.

12. <u>S. Luchkin</u>, K. Romanyuk, M. Ivanov, A. Kholkin, Local probing of Li+ diffusion in Li-ion battery materials by Scanning Probe Microscopy, NANOMOTION student's workshop, Barselona, Spain, 05 Febrary – 06 Febrary 2015. Oral presentation.

13. H.-Y. Amanieu, H. Thai, <u>S. Luchkin</u>, Daniele Rosato, Joerg Schroeder, Electrochemical Strain Microscopy Time Spectroscopy: Model and Experiment on $LiMn_2O_4$, 2015 MRS Spring Meeting, San Francisco, CA, USA, 06 April – 10 April 2015. Oral presentation. Not present.

Curriculum Vitae

Name: Sergey Luchkin

Date of Birth: July 12, 1985, Russia

Nationality: Russian

2015 PhD thesis at University of Aveiro, Portugal

Study:

1.   05/2012 – 05/2015
PhD student, Early Stage Researcher within the Marie Curie ITN NANOMOTION project, CICECO, University of Aveiro, Aveiro, Portugal
Project: Li-diffusion in Li-ion battery materials

2.   09/2003 – 04/2009 M.Sc. and B.Sc. in Physics
Moscow Engineering-Physical Institute (State University), Moscow, Russia
Principal subjects: Functional and structural materials of nuclear reactors

Work experience:

1.   02/2010 – 04/2012
Engineer, Academian A.A. Bochvar All-Russia Research Institute of Inorganic Materials, Moscow, Russia
Description: High temperature superconductors R&D. MgO and YSZ buffer layers, YBCO HTSC-2G, ion-beam-assisted deposition (IBAD).

2.   09/2006 – 02/2009
Intern in the research laboratory ONIL-709, Moscow Engineering-Physical Institute (State University), Moscow, Russia
Description: Influence of accelerated ions on the surface layer of nuclear energy materials (alloying of the surface layer and degradation of fuel element's shells under radiation).